Guiding Light to Detect Life: Nanowires for Optical Biosensing

Davtyan, Rubina

2026

Document Version:
Publisher's PDF, also known as Version of record

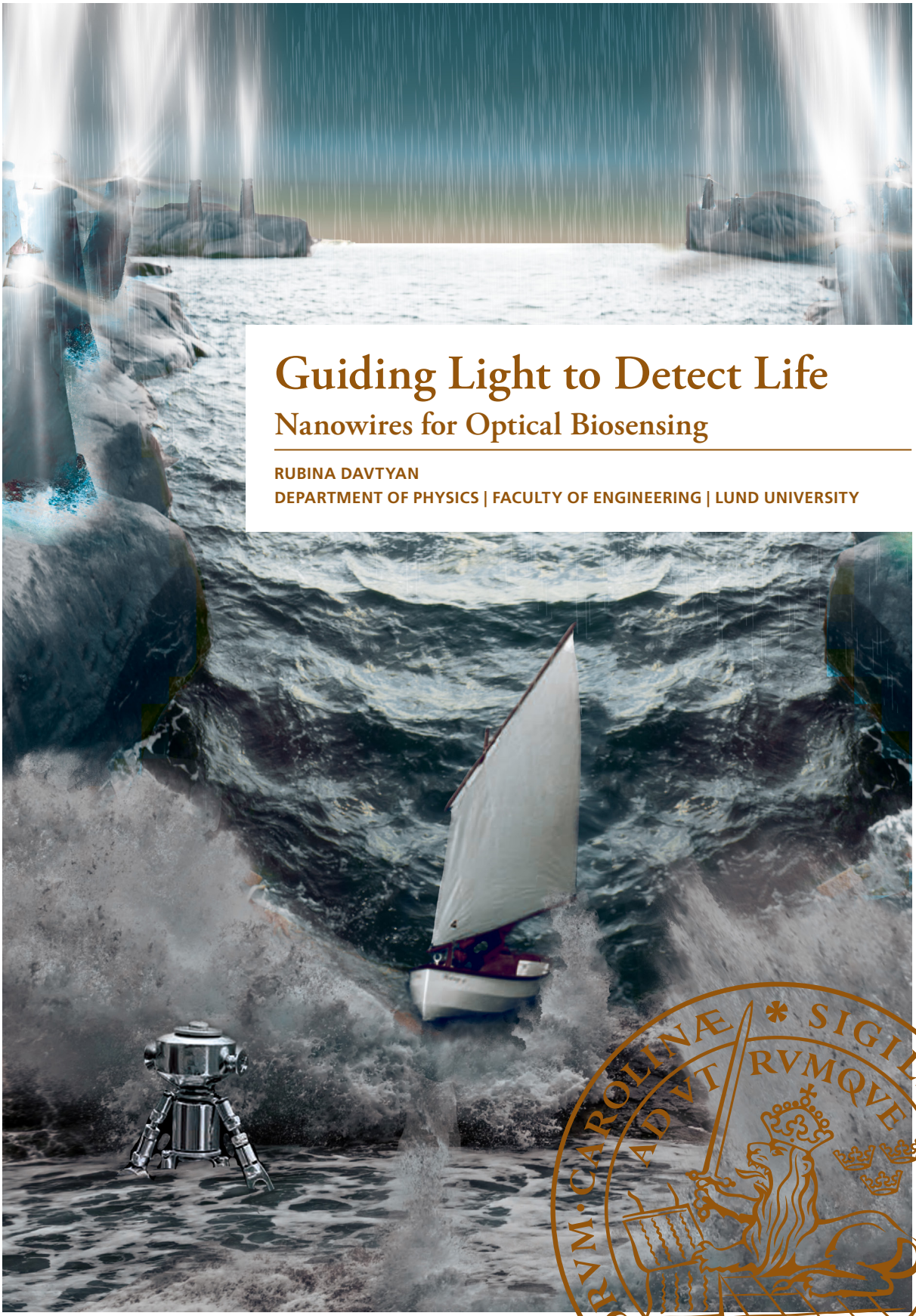

Guiding Light to Detect Life

Nanowires for Optical Biosensing

RUBINA DAVTYAN
DEPARTMENT OF PHYSICS | FACULTY OF ENGINEERING | LUND UNIVERSITY

Guiding Light to Detect Life: Nanowires for Optical Biosensing

Guiding Light to Detect Life: Nanowires for Optical Biosensing

by Rubina Davtyan

LUND
UNIVERSITY

Thesis for the degree of Doctor of Philosophy
Thesis advisors: Prof. Heiner Linke, Prof. Fredrik Höök
Faculty opponent: Dr. Ruby Peters, University of Sheffield, UK

To be presented, with the permission of the Faculty of Engineering of Lund University, for public criticism on 6th of February, 2026 at 09:15 in the Rydberg lecture hall at the Department of Physics, Sölvegatan 14A, Lund.

Organization
LUND UNIVERSITY

Department of Physics
Box 118
SE–221 00 LUND
Sweden

Document name
DOCTORAL DISSERTATION

Date of disputation
2026-02-06

Sponsoring organization

Author(s)
Rubina Davtyan

Title and subtitle
Guiding Light to Detect Life: Nanowires for Optical Biosensing

Abstract
Semiconductor nanowires provide a versatile platform for fluorescence-based detection enabled by their high refractive index and waveguiding properties, which amplify excitation and emission from surface-bound fluorophores. Together with their large surface-to-volume ratio, these features enable enhanced and even single-molecule sensitivity.

This thesis explores the use of gallium phosphide (GaP) and silicon (Si) nanowires through integrated experimental and computational studies, demonstrating their capabilities for sensitive and quantitative biosensing applications.

Using single-emitter localization on well-spaced vertical nanowires combined with brightfield microscopy and systematic analysis, detection ranges can extend over five orders of magnitude, reaching femtomolar levels in streptavidin-biotin assays. Similarly, immobilizing fluorescent molecular beacons on nanowires improves signal-to-background contrast and allows direct oligonucleotide detection at sub-nanomolar concentrations. The nanowire geometry also facilitates extraction of off-plane molecular positions: by modeling point spread functions and training convolutional neural networks on simulated Maxwell datasets, axial localization accuracies below 100 nm are achieved, enabling tracking of labeled DNA diffusing in supported lipid bilayers.

Nanowires also function effectively in complex sample environments. When embedded in polymer matrices and imaged through transparent substrates, they overcome scattering and absorption in opaque media, allowing sub-nanomolar detection of fluorescently labeled proteins in whole blood, lipid emulsions, and powdered milk without sample processing.

Overall, this thesis expands the application scope of semiconductor nanowires for optical biosensing, demonstrating single-molecule detection, extended dynamic range, direct oligonucleotide sensing, three-dimensional localization, and operation in opaque biological samples.

Key words
Nanowires, Biosensing, Fluorescence Microscopy, Single-Molecule Detection, Computational Modeling, Image Analysis

Classification system and/or index terms (if any)

Supplementary bibliographical information

Language
English

ISSN and key title

ISBN
978-91-8104-794-3 (print)
978-91-8104-795-0 (pdf)

Recipient's notes

Number of pages
230

Price

Security classification

Signature

Date 2026-02-06

Guiding Light to Detect Life: Nanowires for Optical Biosensing

by Rubina Davtyan

LUND
UNIVERSITY

Cover illustration front: Artistic representation of nanowire-based optical biosensing. ©Tigran Arakelyan.

Cover illustration back: My journey to Middle Earth (Aotearoa/New Zealand)

Popular science summary illustration: Another artistic representation of nanowire-based optical biosensing. ©Maria Zakaryan.

Funding information: Swedish Research Council (2019–02435 and 2020–04226), NanoLund, and the European Union's Horizon 2020 research and innovation program under the Marie Skłodowska-Curie grant agreement No. 945378.

Faculty of Engineering, Department of Physics

isbn: 978-91-8104-794-3 (print)
isbn: 978-91-8104-795-0 (pdf)

Printed in Sweden by Media-Tryck, Lund University, Lund 2026

Media-Tryck is a Nordic Swan Ecolabel certified provider of printed material. Read more about our environmental work at www.mediatryck.lu.se

Printed matter 3041 0903

MADE IN SWEDEN

Dedicated to
those who were denied
the chance to succeed.

Contents

Abstract

Semiconductor nanowires provide a versatile platform for fluorescence-based detection enabled by their high refractive index and waveguiding properties, which amplify excitation and emission from surface-bound fluorophores. Together with their large surface-to-volume ratio, these features enable enhanced and even single-molecule sensitivity.

This thesis explores the use of gallium phosphide (GaP) and silicon (Si) nanowires through integrated experimental and computational studies, demonstrating their capabilities for sensitive and quantitative biosensing applications.

Using single-emitter localization on well-spaced vertical nanowires combined with bright-field microscopy and systematic analysis, detection ranges can extend over five orders of magnitude, reaching femtomolar levels in streptavidin-biotin assays. Similarly, immobilizing fluorescent molecular beacons on nanowires improves signal-to-background contrast and allows direct oligonucleotide detection at sub-nanomolar concentrations. The nanowire geometry also facilitates extraction of off-plane molecular positions: by modeling point spread functions and training convolutional neural networks on simulated Maxwell datasets, axial localization accuracies below 100 nm are achieved, enabling tracking of labeled DNA diffusing in supported lipid bilayers.

Nanowires also function effectively in complex sample environments. When embedded in polymer matrices and imaged through transparent substrates, they overcome scattering and absorption in opaque media, allowing sub-nanomolar detection of fluorescently labeled proteins in whole blood, lipid emulsions, and powdered milk without sample processing.

Overall, this thesis expands the application scope of semiconductor nanowires for optical biosensing, demonstrating single-molecule detection, extended dynamic range, direct oligonucleotide sensing, three-dimensional localization, and operation in opaque biological samples.

List of publications

This thesis is based on the following publications, referred to by their Roman numerals:

i **Enhanced optical biosensing by Aerotaxy Ga(As)P nanowire platforms suitable for scalable production**

J. Valderas-Gutiérrez, R. Davtyan, S. Sivakumar, N. Anttu, Y. Li, P. Flatt, J. Y. Shin, C. N. Prinz, F. Höök, T. Fioretos, M. H. Magnusson, and H. Linke

ACS Appl. Nano Mater., 2022, 5, pp. 3085-3092

I performed the image analysis and contributed to writing the manuscript.

ii **Sub-nanomolar detection of oligonucleotides using molecular beacons immobilized on lightguiding nanowires**

T. B. Johansson*, R. Davtyan*, J. Valderas-Gutiérrez, A. Gonzalez Rodriguez, B. Agnarsson, R. Munita, T. Fioretos, H. Lilljebjörn, H. Linke, F. Höök, and C. N. Prinz

Nanomaterials (Basel), 2024, 14(5), p. 453

I participated in the experiments, particularly fluorescence imaging. I designed and conducted the data analysis and contributed to writing the manuscript.
*These authors contributed equally and share first authorship.

iii **Image analysis optimization for nanowire-based optical detection of molecules**

R. Davtyan, N. Anttu, J. Valderas-Gutiérrez, F. Höök, and H. Linke

Nanophotonics, 2024, 14(15), pp. 2563-2574

I performed the end-point and time-resolved experiments. I generated images from computational models and created synthetic data. I designed and developed the image analysis software NanoLoci using both existing and custom algorithms. I validated the simulated and experimental data and wrote the manuscript with contributions from all authors.

iv **Comparative kinetics of supported lipid bilayer formation on silica coated vertically oriented highly curved nanowires and planar silica surfaces**

J. Valderas-Gutiérrez, R. Davtyan, C. N. Prinz, E. Sparr, P. Jönsson, H. Linke, and F. Höök

Nano Lett., 2025, 25, pp. 3085-3092

I participated in discussions, data analysis and contributed to writing the manuscript.

v **Turning nanowires into off-plane molecular trackers through point spread function detection**

R. Davtyan, J. Valderas-Gutiérrez, N. Anttu, J. Beech, F. Höök, H. Linke

In Manuscript

I conceived the idea of position tracking from defocused images, performed microscopy image creation and diffusion simulations, neural network training, and data analysis. I conducted imaging experiments and wrote the manuscript with contributions from all authors.

vi **Lightguiding nanowires as a platform for biosensing in non-transparent media, including whole human blood**

N. Al-Khulaifi, J. Valderas-Gutiérrez, C.N. Prinz, H. Linke, R. Davtyan

In Manuscript

I initiated and led the study, advised N. Al-Khulaifi, and led the acquisition of the ethical permit. I contributed to the conceptualization and design of the project, as well as to the planning and execution of experiments. I developed image analysis tools, contributed to data processing and interpretation, and co-wrote the manuscript with N. Al-Khulaifi, with input from all authors.

All published papers are reproduced with permission of their respective publishers. Paper V and VI are reproduced with permission from the co-authors.

Publications not included in this thesis:

vii **Nanowire-based biosensor for short DNA using fluorescent silver nanoclusters**

I.N. Unksov, R. Davtyan, C.N. Prinz, H. Linke

Submitted to Sensors Actuators A: Physical

I participated in the experiments and data analysis. I contributed to writing the manuscript.

Popular science summary in English

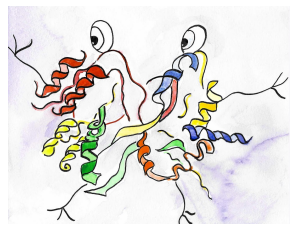

In the tiniest realms, lands and waters so small that the whole world would fit on the tip of a needle, on time scales so short that your clock could never measure them, lived countless tiny creatures and roamed countless mysteries. These were lands of molecules, invisible to naked eyes, yet in constant motion, dancing and weaving the fabric of life, and sometimes, the fabric of disease and decay.

There were the proteins, which you, my dear reader, may know from casual talk of diets and health, but here they were heroes far greater than that. They fold and unfold, shaping bridges for communication, building structures, defending, and patching wounds where the world was hurting. There were also DNA molecules, the ancient librarians, keeping every known and unknown story. We should not forget DNA's cousin, RNAs. Did you know that some of them are messengers? They take the information from our librarians, travel all the way to the cells, and tell them how to make proteins. There were also lipids, squishy architects that build the soft yet strong walls of cells, separating the inside from the outside, the life from chaos.

These worlds were in total darkness, unless they were inside a firefly or a glowing jellyfish. Did you know that fireflies produce their own light? But let's not get distracted, that, my friend, is a tale for another day.

Back to our story: though many creatures wondered how these tiny worlds worked, not very many dared to go into these lands. Some thought these molecules were too chaotic, too difficult to understand, too unpredictable. Yet in this tiny realm wandered a small but determined figure, the Detective, who longed to reveal the invisible signs

of disease creeping into molecular lands and oceans. Because, my dear reader, when some illnesses strike, they send an army of strange molecules ahead of time. And the Detective believed that if one finds these early enough, help can be summoned from the greater worlds above. But first, they needed to identify these spies, hiding within regular DNAs and proteins, yet carrying the mark of decay.

To say that our tiny hero was scared would be wrong. But although that was a tiny land, it was so big and so mysterious. When our Detective was floating around in darkness, thinking what to do, they suddenly heard from somewhere:

"Make them glow! Make them glow so we can see them!"

"Hello? Who's there?"

Suddenly, a million colors turned on in the darkness, shifting, turning, and shining with all colors of the rainbow, which our Detective had never seen before. It was dazzling, beautiful, and a bit scary.

"I am Lumi N. Essence, the friend of photons, the weaver of wavelengths, and the fae of fluorescence! Should we give this little world a makeover, I mean a *glow-up*. Catch this!"

With that, Lumi threw tiny glowing spheres towards our Detective, who caught them with admiration and curiosity.

"These are fluorescent probes! Attach them to the molecules you want to see, and they'll shine bright like diamonds in the sky! Watch me!"

Lumi threw a probe at a nearby protein, then pointed her finger, from which a blue light emerged. Suddenly, the protein was glowing green.

"Magic?"

"Sweetie, it's called fluorescence. Look it up sometime! It's on page 7."

The light beaming from Lumi N. Essence started to fade, as she whispered: "Honey, if you lose your way, remember that even the tiniest glow can slay the darkness."

With that, Lumi vanished into the darkness, leaving our Detective alone with colorful probes, a flashlight, and a bright glow of hope.

The Detective was having a lot of fun throwing probes at different molecules, seeing them

move and dance in the dark. But soon after, they realized that although the probes were bright, they were still not bright enough to see them far away in the darkness. So our Detective wandered the darkness with a tiny flashlight, looking for ways to make the probes even brighter. And suddenly, when they were sailing on the dark oceans, the tiny boat hit something hard.

"Can this life ever be easy?" sighed our Detective, as they looked in front of them. It was a tall narrow pillar, made out of shiny crystal.

"Can you strangers be a bit more careful? You almost wrecked my beautiful structure!" a deep voice echoed from the pillar.

"You... you talk?" asked our Detective, surprised.

"Duhhh! Of course I do, like everyone else here! Next time, try announcing your arrival before crashing into me!"

"I am really sorry. I haven't seen you in the dark."

"Well, now you have, you clumsy mortal! I am a Nanowire, a *grown* nanoscale optical fibre, not a random pillar. But whatever, you won't even understand the difference, even if I explained it slowly," the Nanowire grumbled.

Our Detective decided to leave the Nanowire alone for now, but they had to do one last thing. The Detective picked up one of the fluorescent probes and threw it at the Nanowire, who caught it immediately. As the Detective shone their flashlight, something magical happened, the probe seemed to glow even brighter. And there was more: the light from the probe traveled through the Nanowire, reaching far distances in the dark ocean.

"Wow! You can make molecules even brighter!" exclaimed our Detective.

"Duh, obviously. I am a lightguiding nanowire. I am made for this. So are my siblings!" told the Nanowire proudly.

The Detective realized that they had found a powerful ally to help them in their mission. Then our Detective flew up and saw the Nanowire forest, all glowing, the light stretching far into the darkness.

Then our Detective realized that something was still missing. There were so many molecules in this land, so many nanowires, so much light, yet one had to make use of it all. They still needed a way to detect and quantify the glowing signals from far away. As an amateur photographer, our Detective knew a thing or two about cameras. With a very special camera, which could capture even the faintest glimmers of light, our Detective could finally see the glowing molecules from afar.

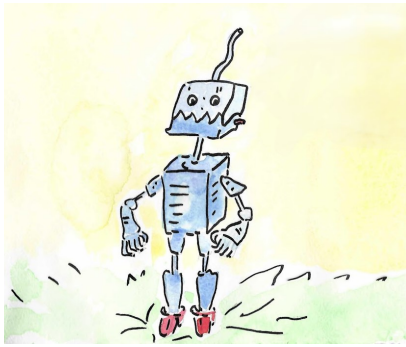

But our Detective didn't really know how to make sense of these pictures. They didn't look anything like the pictures they had seen before. The glowing spots were all over the place: some were big, some were small, some were bright, some were dimmer. How could one tell which spot was which molecule? How could one tell how many molecules were there? This time no help seemed to come from the darkness. Our Detective had to make something on their own. The Detective decided to build something, a robot perhaps, that could analyze the pictures and tell what was in them. So that is how NanoLoci was born, a tiny robot who got her name from the locations plus Loki, the god of mischief. Because, you know, molecules like to hide and play tricks. Our Detective even taught NanoLoci a bit of artificial intelligence. While still not as clever, it could learn, combine images, and get better and better.

So now our Detective had all the tools. They wanted to make sense of Life, had the power of Light, fluorescent probes, light source, and camera, and the power of Materials, nanowires. And the final piece of the puzzle, the Machine, NanoLoci, the robot that could analyze the pictures. And far did our Detective go. Using all these tools, they could finally start finding the spies of disease. They even went to very complicated places, where light couldn't easily reach, like looking in blood. And slowly but surely, our Detective started to uncover the secrets of molecular lands, one glowing molecule at a time.

This tale is not over yet. Maybe one day, my dearest reader, you will be the next detective to explore these tiny lands, or maybe even tinier or much larger ones. When one Detective reaches their destination, another one's journey begins. Because science is a journey, not a destination.

From Story to Science

During global health crises like the COVID-19 pandemic, the need for rapid, sensitive, and accurate detection of biological molecules has become more apparent than ever. With healthcare systems under strain, and rapid tests often falling short in sensitivity, the pressing need for cheap, accessible, but highly sensitive diagnostic tools was clearer than ever. Even beyond pandemics, early-stage detection of diseases such as cancer relies heavily on identifying trace amounts of specific biomolecules. Less privileged regions globally often lack access to advanced diagnostic tools, making the development of affordable and sensitive detection methods crucial for global health equity. Underprivileged communities, such as people in rural areas, people with disabilities, elderly populations, transgender individuals, and marginalized groups, both in developed and developing countries, often face barriers to accessing timely and accurate diagnostics, leading to delayed treatments and poorer health outcomes. Affordable and sensitive detection technologies can bridge this gap, ensuring that everyone, regardless of their socioeconomic status, has access to essential healthcare services.

This thesis is part of the broader scientific endeavor to develop advanced optical biosensing techniques that can meet these critical needs. The fairy tale above is a metaphorical representation of the key components and motivations behind this research. It captures the essence and motivation of the thesis: detecting biological molecules accurately and efficiently is critical for disease diagnostics and understanding life processes. The story's tiny molecular lands represent the complex biological world invisible to the naked eye, where proteins, DNA, RNA, and lipids play essential roles.

Lightguiding nanowires, which are the main tools of trade in this research, can amplify fluorescent signals from molecules, enhancing detection sensitivity by orders of magnitude. Combined with fluorescence microscopy and computational tools, these nanowires enable the detection of low concentrations of biomolecules, even in complex environments like blood.

The story shows how this type of research is between multiple disciplines: physics, chemistry, biology, materials science, and computational science. In this work, experimental techniques are combined with modeling and analysis to push the boundaries of what is possible in optical biosensing, detecting ever smaller amounts of biological molecules with greater accuracy.

Populärvetenskaplig sammanfattning på svenska

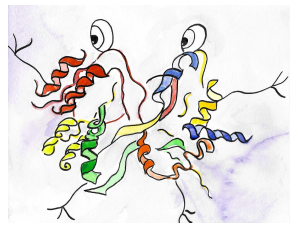

I de minsta riken, på land och i vatten så små att hela världen skulle få plats på en nålspets, på tidsskalor så korta att din klocka aldrig skulle kunna mäta dem, levde otaliga små varelser och vandrade otaliga mysterier. Det var molekylernas rike, osynligt för blotta ögat, men i ständig rörelse, dansande och vävande livets väv, och ibland, sjukdomens och förfallets väv.

Det fanns proteiner, som du, kära läsare, kanske känner till från vardagliga samtal om kost och hälsa, men här var de hjältar som var mycket större än så. De veckade och vecklade ut sig, formade broar för kommunikation, byggde strukturer, försvarade och lappade sår där världen var skadad. Det fanns också DNA-molekyler, de uråldriga bibliotekarierna, som bevarade alla kända och okända historier. Vi får inte glömma DNA:s kusin, RNA. Visste du att vissa av dem är budbärare? De hämtar informationen från våra bibliotekarier, reser hela vägen till cellerna och berättar för dem hur de ska tillverka proteiner. Det fanns också lipider, mjuka arkitekter som bygger cellernas mjuka men starka väggar, som skiljer insidan från utsidan, livet från kaoset.

Dessa världar var i total mörker, såvida de inte befann sig inuti en eldfluga eller en lysande manet. Visste du att eldflugor producerar sitt eget ljus? Men låt oss inte distraheras, det, min vän, är en historia för en annan dag.

Tillbaka till vår berättelse: även om många varelser undrade hur dessa små världar fungerade, var det inte många som vågade bege sig in i dessa länder. Vissa tyckte att dessa molekyler var för kaotiska, för svåra att förstå, för oförutsägbara. Men i detta

lilla rike vandrade en liten men beslutsam figur, Detektiven, som längtade efter att avslöja de osynliga tecknen på sjukdomar som smög sig in i molekylära länder och hav. För, kära läsare, när vissa sjukdomar slår till, skickar de en armé av märkliga molekyler i förväg. Och detektiven trodde att om man hittade dessa i tid, kunde man kalla på hjälp från de större världarna ovanför. Men först måste de identifiera dessa spioner, som gömde sig i vanliga DNA och proteiner, men ändå bar på tecken på förfall.

Att säga att vår lilla hjälte var rädd skulle vara fel. Men även om det var ett litet land, var det så stort och så mystiskt. När vår detektiv svävade omkring i mörkret och funderade på vad hen skulle göra, hörde hen plötsligt någonstans:

”Få dem att lysa! Få dem att lysa så att vi kan se dem!”

”Hallå? Vem är där?”

Plötsligt tändes en miljon färger i mörkret, skiftande, vändande och lysande med alla regnbågens färger, som vår detektiv aldrig hade sett förut. Det var bländande, vackert och lite skrämmande.

”Jag är Lumi N. Essence, fotonernas vän, våglängdernas vävare och fluorescensens fe! Ska vi ge den här lilla världen en makeover, jag menar en *glow-up*. Fånga den här!”

Med det kastade Lumi små lysande sfärer mot vår detektiv, som fångade dem med beundran och nyfikenhet.

”Det här är fluorescerande sonder! Fäst dem på de molekyler du vill se, så kommer de att lysa som diamanter på himlen! Titta på mig!”

Lumi kastade en sond mot ett närliggande protein och pekade sedan med fingret, varifrån ett blått ljus strålade ut. Plötsligt lyste proteinet grönt.

”Magi?”

”Älskling, det kallas fluorescens. Slå upp det någon gång! Det står på sidan 7.”

Ljuset som strålade från Lumi N. Essence började blekna, medan hon viskade: ”Älskling, om du går vilse, kom ihåg att även det minsta skenet kan besegra mörkret.”

Med det försvann Lumi in i mörkret och lämnade vår detektiv ensam med färgglada prober, en ficklampa och ett starkt sken av

hopp.

Detektiven hade mycket roligt med att kasta prober på olika molekyler och se dem röra sig och dansa i mörkret. Men snart insåg de att även om proberna var ljusa, var de fortfarande inte tillräckligt ljusa för att synas långt bort i mörkret. Så vår detektiv vandrade omkring i mörkret med en liten ficklampa och letade efter sätt att göra proberna ännu ljusare. Och plötsligt, när de seglade på de mörka haven, stötte den lilla båten på något hårt.

”Kan livet någonsin bli lätt?” suckade vår detektiv, medan han tittade framför sig. Det var en hög, smal pelare, gjord av glänsande kristall.

”Kan ni främlingar vara lite mer försiktiga? Ni förstörde nästan min vackra struktur!” ekade en djup röst från pelaren.

”Du... kan du prata?” frågade vår detektiv förvånat.

”Duhhh! Självklart gör jag det, precis som alla andra här! Nästa gång, försök att meddela din ankomst innan du kraschar in i mig!”

”Jag är verkligen ledsen. Jag såg dig inte i mörkret.”

”Nu har du det, din klumpiga dödliga! Jag är en nanotråd, en *odlad* optisk fiber i nanoskala, inte en slumpmässig pelare. Men hur som helst, du skulle inte förstå skillnaden även om jag förklarade det långsamt”, muttrade nanotråden.

Vår detektiv bestämde sig för att lämna Nanowire ifred för tillfället, men de var tvungna att göra en sista sak. Detektiven plockade upp en av de fluorescerande sonderna och kastade den mot Nanowire, som fångade den omedelbart. När detektiven lysde med sin ficklampa hände något magiskt: sonden verkade lysa ännu starkare. Och det var inte allt: ljuset från sonden färdades genom Nanowire och nådde långt i det mörka havet.

”Wow! Du kan göra molekylerna ännu ljusare!”, utropade vår detektiv.

”Självklart. Jag är en ljusledande nanotråd. Jag är gjord för det här. Det är mina syskon också!”, sa nanotråden stolt.

Detektiven insåg att de hade hittat en mäktig allierad som kunde hjälpa dem i deras uppdrag. Sedan flög vår detektiv upp och såg nanotrådsdjungeln, som glödde och sträckte sig långt in i mörkret.

Då insåg vår detektiv att något fortfarande saknades. Det fanns så många molekyler i detta land, så många nanotrådar, så mycket ljus, men man måste kunna utnyttja allt detta. De behövde fortfarande ett sätt att upptäcka och kvantifiera de lysande signalerna på långt avstånd. Som amatörfotograf visste vår detektiv en del om kameror. Med en mycket speciell kamera, som kunde fånga även de svagaste ljusglimtar, kunde vår detektiv äntligen se de

lysande molekylerna på långt avstånd.

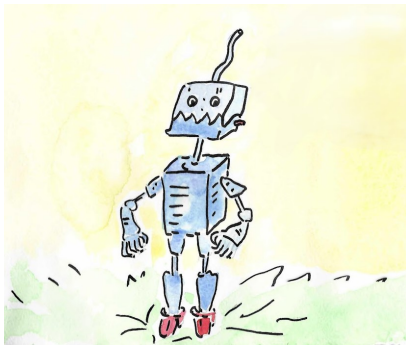

Men vår detektiv visste inte riktigt hur han skulle tolka dessa bilder. De liknade inte alls de bilder han hade sett tidigare. De lysande fläckarna fanns överallt: vissa var stora, andra små, vissa ljusa, andra svagare. Hur kunde man se vilken fläck som var vilken molekyl? Hur kunde man se hur många molekyler det fanns? Den här gången verkade det inte komma någon hjälp från mörkret. Vår detektiv var tvungen att skapa något själv. Detektiven bestämde sig för att bygga något, kanske en robot, som kunde analysera bilderna och avgöra vad som fanns i dem. Så föddes NanoLoci, en liten robot som fick sitt namn från platserna plus Loki, den busiga guden. För, som ni vet, molekyler gillar att gömma sig och spela spratt. Vår detektiv lärde till och med NanoLoci lite artificiell intelligens. Den var fortfarande inte så smart, men den kunde lära sig, kombinera bilder och bli bättre och bättre.

Nu hade vår detektiv alla verktyg. De ville förstå livet och hade kraften från ljus, fluorescerande sonder, ljuskällor och kameror, samt kraften från material, nanotrådar. Och den sista pusselbiten, maskinen NanoLoci, roboten som kunde analysera bilderna. Vår detektiv kom långt. Med hjälp av alla dessa verktyg kunde de äntligen börja hitta sjukdomarnas spioner. De tog sig till och med till mycket komplicerade platser, där ljuset inte lätt kunde nå, som att titta i blod. Och sakta men säkert började vår detektiv avslöja hemligheterna i molekylära landskap, en glödande molekyl i taget.

Denna berättelse är inte slut ännu. Kanske en dag, min kära läsare, kommer du att vara nästa detektiv som utforskar dessa små världar, eller kanske ännu mindre eller mycket större. När en detektiv når sitt mål, börjar en annans resa. För vetenskap är en resa, inte ett mål.

Från berättelse till vetenskap

Under globala hälsokriser som COVID-19-pandemin har behovet av snabb, känslig och noggrann detektion av biologiska molekyler blivit tydligare än någonsin. Med pressade hälso- och sjukvårdssystem och snabbtester som ofta brister i känslighet blev det tydligare än någonsin att det finns ett akut behov av billiga, tillgängliga men mycket känsliga diagnostiska verktyg. Även utanför pandemier är tidig upptäckt av sjukdomar som cancer i hög grad beroende av att spårmängder av specifika biomolekyler identifieras. Mindre privilegierade regioner globalt saknar ofta tillgång till avancerade diagnostiska verktyg, vilket gör utvecklingen av prisvärda och känsliga detektionsmetoder avgörande för global hälsojämlikhet. Underprivilegierade grupper, såsom människor i landsbygdsområden, personer med funktionsnedsättningar, äldre, transpersoner och marginaliserade grupper, både i utvecklade länder och utvecklingsländer, möter ofta hinder för att få tillgång till snabb och noggrann diagnostik, vilket leder till försenade behandlingar och sämre hälsoresultat. Prisvärda och känsliga detekteringstekniker kan överbrygga denna klyfta och säkerställa att alla, oavsett socioekonomisk status, har tillgång till nödvändig hälso- och sjukvård.

Denna avhandling är en del av ett bredare vetenskapligt arbete för att utveckla avancerade optiska biosensorteknologier som kan tillgodose dessa kritiska behov. Sagans handling är en metaforisk representation av de viktigaste komponenterna och motivationen bakom denna forskning. Den fångar essensen och motivationen bakom avhandlingen: att detektera biologiska molekyler noggrant och effektivt är avgörande för sjukdomsdiagnostik och förståelse av livsprocesser. Berättelsens små molekylära länder representerar den komplexa biologiska världen som är osynlig för blotta ögat, där proteiner, DNA, RNA och lipider spelar viktiga roller.

Ljusledande nanotrådar, som är de viktigaste verktygen i denna forskning, kan förstärka fluorescerande signaler från molekyler och förbättra detektionskänsligheten med flera storleksordningar. I kombination med fluorescensmikroskopi och beräkningsverktyg möjliggör dessa nanotrådar detektering av låga koncentrationer av biomolekyler, även i komplexa miljöer som blod.

Berättelsen visar hur denna typ av forskning sträcker sig över flera discipliner: fysik, kemi, biologi, materialvetenskap och beräkningsvetenskap. I detta arbete kombineras experimentella tekniker med modellering och analys för att flytta gränserna för vad som är möjligt inom optisk biosensorik och detektera allt mindre mängder biologiska molekyler med större noggrannhet.

Acknowledgements

This thesis spans a wide range of topics, from biology to computational modeling, and from experiments to theory. Paradoxically, one of the most difficult sections to write has been the acknowledgements. This is not due to a lack of people to thank, but because so many individuals, within and beyond academia, have contributed in meaningful ways throughout this journey.

This work began during an unusually difficult period: the COVID-19 pandemic, shortly after a war in my home country, and amid uncertainties that felt larger than even the worst experimental results. Yet, somehow, it worked out. For that, I am deeply grateful to my main supervisor, Heiner. Thank you for believing in me when I doubted myself, for keeping the position during visa delays, for suggesting scientific ideas while giving me the freedom to explore them, and for helping me stop overthinking and simply do the work.

Fredrik, you once noted that a co-supervisor's role is to guide a student when they feel lost—scientifically or otherwise. Your sense of when to accelerate and when to slow down has been invaluable, as has your creative perspective on science and life more broadly. I am also sincerely grateful to Nicklas, whose modeling work formed the foundation of much of this thesis, and for his responsiveness and generosity, including hosting me during my visit to Turku.

To my past and present colleagues in the Linke lab: you have all made this journey memorable. Julia, you have been there since the beginning—training me in experiments, serving as the experimental backbone of the lab, and being such a joy to be around both inside and outside FTF. Vanya, thank you for your warm and welcoming presence in the lab and beyond. Noah, you have been my first and best Master's student so far, and I am very proud of you. To all past and present lab members: Palle (special thanks for catalyzing so many meta- discussions), Pradheebha, Nils, Anna, Eliz, Sina, Mikkel, Michael, Mariia, Tadija, Javier, Eric, Noah, David, Elena, and others - it has truly been great working with you.

To everyone in the Biogroup: from long safety discussions to philosophical conversations, you made workdays, especially Fridays, something to look forward to. Jason, thanks for

holding the biolabs together. I am grateful to the Gene and Wires collaboration and to AlignedBio for providing the nanowires used in this thesis.

To all PhD students and postdocs at FTF: without naming everyone individually, you have created a stimulating and supportive environment, from scientific discussions to bandy runs, fika breaks, and unforgettable NanoLund retreats. David, your integrity and dedication to doing what is right have always been inspiring. Maxi, thank you for your authenticity and for guiding me through the final steps of thesis submission and the complexities of planning a celebration. Elham, your courage and strength are admirable. Matteo, the conversations about life, politics, and everything in between. Enrico, thanks for the many deep talks and for getting me into running. Outside FTF, I am really glad that clean room adventures brought you around, Damian. And Ayan, maybe the real teaching is the friends we made along the way?

I would also like to thank the administrative, IT, and technical staff at FTF, whose work keeps everything running smoothly. Alexandra, you brought colors to FTF and made complex administrative processes easier to navigate. Alfons and Andreas, thank you for your technical support and for setting up Smaug, which enabled my simulations. Anne, Evelina, and Anna-Karin, thanks for your kindness, motivation, and support. While I am just an admirer of the clean room from afar, I am grateful for the expertise, assistance, and the humor of the clean room staff. Dan, I really appreciate your fairness and care for everyone as a head of division.

Although many of the exciting things I experienced in New Zealand did not make it into this thesis, the people certainly made it into my life. I am grateful to Jami and her group, as well as to the best office mates one could ask for. Luyang, you are a true treasure. Kim and Scott, thank you for treating me like family.

Of course, none of this would have been the same without my friends, both near and far. Morten and Byurakn across the bridge: the pub quizzes at Trows, the food, and the conversations were a warm welcome to the cold Nordics. Tigran, through sad, chaotic, happy, strange, and fun times, you have always been someone I could rely on. Mariia, I am glad our paths crossed and that we shared these unusual times together.

Beyond individuals, communities and places also matter. Some came and went but left a lasting mark: Kalmar nation, Smålands nation, Dubbelexponerat (especially since I got to become friends with you, Jesse), the Malmö improv group, and Page 28. One constant has been my dearest DnD group. From my very first months in Lund, you brought adventure and joy. Nightbreeze is family, and zeros shall become heroes.

Maria V., from Lund to Yerevan to San Francisco—especially during the most confusing times—your empathy and wisdom helped me stay grounded. Astgh, since that Serj Tankian concert 15 years ago, you provided a sunny refuge when darkness crept in. Serena, I would

not be the same person without you. Your strength and wisdom continue to inspire me. Mario, although I am surrounded by remarkable scientists, you remain my favorite, and I hope we excavate together one day. And Maria Z., I am a better person because of you, and I can carry the sky for you.

Finally, my deepest gratitude goes to my family. MJ, Areg, and Bert in Canada—thank you for giving me yet another home away from home. Mom, Dad, and Sabina, you showed up for me in ways I could never have imagined. Thank you for the unwavering support and believing that in the end, I would find a way, my way. With my biological and chosen family all around the world, there would always be a *home*.

There are many people I met before and during my PhD who taught me about kindness, resilience, and care. People who did not lose hope even in the darkest times, and who inspired me to keep going and to believe that the world can be better. This thesis is for all of you, and for those who never had the opportunity or privilege to pursue their dreams.

Acronyms

Au	gold	23
bBSA	biotinylated bovine serum albumin	30
BSA	bovine serum albumin	30
CNN	convolutional neural network	52, 66, 76
DFT	discrete Fourier transform	58
FEM	finite element method	47
FFT	fast Fourier transform	50, 51, 58, 62, 69
FOV	field of view	20
Ga(As)P	gallium (arsenide) phosphide	16, 25, 26, 80
GaP	gallium phosphide	16, 17, 22, 23, 25, 39, 61, 73, 80, 86
IFFT	inverse fast Fourier transform	52, 62
LOD	limit of detection	28, 32
MB	molecular beacons	28, 32–34
MOVPE	metalorganic vapour-phase epitaxy	22–25
NA	numerical aperture	18, 19, 47, 52, 95
NFFT	near-field-to-far-field transformation	51
NW	nanowire	19, 22, 24, 25, 37
PCR	polymerase chain reaction	2, 31
PDMS	polydimethylsiloxane	38, 39, 41
POC	point-of-care	2, 4, 37
PSF	point-spread function	52–54, 56, 57, 65, 68, 76
QY	quantum yield	18, 50
ROI	regions of interest	21

SEM	scanning electron microscopy	23, 25
Si	silicon	16, 17, 22, 25, 26, 37–39, 61
SLB	supported lipid bilayer	28, 35–37, 89, 94
SNR	signal-to-noise ratio	13, 17, 54
TIRF	total internal reflection fluorescence	7, 13, 95
VLS	vapor-liquid-solid	24

Chapter 1

Introduction

The most important step a man can take. It's not the first one, is it?
It's the next one. Always the next step, Dalinar.

Brandon Sanderson, Oathbringer

"It's a dangerous business, Frodo, going out your door.
You step onto the road, and if you don't keep your feet, there's no
knowing where you might be swept off to."

J.R.R. Tolkien, The Lord of the Rings

1.1 Background and motivation

Detecting and quantifying biological molecules is essential for understanding biophysical processes, diagnosing diseases, and developing new therapies. Biosensing, which broadly refers to the detection of biological molecules, such as proteins, nucleic acids, and small molecules, can rely on electrical, mechanical, chemical, magnetic, or optical transduction methods to convert biological signals into measurable responses. [1–4]

Optical biosensing, in particular, is widely known for its sensitivity, specificity, and versatility. It covers a wide range of techniques, from simple colorimetric assays like commercial pregnancy tests to more complex techniques such as surface plasmon resonance. [5–7] Optical biosensors are becoming widely available both as point-of-care (POC) devices, and as laboratory-based techniques requiring tools such as fluorescence microscopes. Ongoing advancements aim to enhance sensitivity and specificity while simplifying detection protocols. Sample processing varies significantly, ranging from minimal or no preparation as in rapid COVID-19 tests to complex purification and amplification steps exemplified by polymerase chain reaction (PCR) tests. [6, 8, 9]

One of the most commonly used optical detection techniques in biosensing is fluorescence detection, known for its wide application range. [10, 11] Single-molecule biosensors are highly significant because they can detect and characterize analytes in extremely low concentrations. [12–14] Advanced super-resolution imaging techniques and ongoing microscopy developments routinely achieve nanometer-scale resolutions with rapid acquisition times. [15–19] However, while these methods satisfy requirements for sensitivity, selectivity, and response time, they typically rely on large, complex fluorescence microscopes that limit portability and scalability. [14]

Previous studies have demonstrated that nanoparticles, nanostructured surfaces, and specifically semiconductor nanowires can overcome limitations commonly associated with conventional fluorescence techniques. [20, 21] This is achieved by expanding the surface area available for sensor-analyte interactions and providing optical enhancement. [22–25] The optical enhancement schemes, which include (i) waveguide properties of nanowire and directional emission [20, 21, 26], (ii) excitation enhancement [27, 28], and (iii) emission enhancement by quantum yield modification are relatively [29] well studied. While substantial progress has been made in nanowire-based optical detection, key challenges remained prior to this work that motivate this thesis.

First, existing computational tools for analyzing nanowire-enhanced fluorescence images remain limited. Although numerous image-analysis algorithms for single-molecule localization, benchmarked extensively on simulated datasets [30–32], handle diverse noise conditions and sample complexities, [33, 34] they lack adaptation for nanowire-specific phenomena including lightguiding, excitation enhancement, and modified point-spread functions.

This thesis therefore develops and validates nanowire-tailored computational methods, incorporating Maxwell's equation simulations and position-aware image processing pipelines.

Second, while biosensing technologies have advanced, scaling production methods to achieve cost-effective, reproducible, and widespread deployment remains an issue. Many high-sensitivity methods rely on complex fabrication in cleanroom environments or materials that do not lend themselves to scalable manufacturing. A small part of this thesis also explores the use of aerotaxically grown nanowires as a scalable alternative to conventional substrate-grown nanowires for optical biosensing applications.

Third, nanowire-enhanced detection must demonstrate utility across diverse biological systems and complex matrices. This includes molecular beacon immobilization for oligonucleotide detection, investigations of membrane curvature effects on supported lipid bilayer formation, and extension to optically challenging samples such as whole blood, which is critical for clinical translation.

This thesis addresses these challenges through integrated computational tool development, scalable fabrication exploration, and application to realistic biological models. By addressing computational needs, developing scalable nanowire solutions, and validating performance in realistic biological systems, this work aims to bridge fundamental research and practical biosensing applications, advancing the sensitivity, specificity, and real-world applicability of nanowire-based optical detection.

1.2 Structure of the thesis

This thesis comprises an introduction, four core chapters, and results sections. The four main chapters systematically present all experimental and computational methodologies alongside their theoretical foundations, each representing a fundamental element of the interdisciplinary nature of this work. These chapters are organized as follows:

- **Light: Optical microscopy and fluorescence**
  Introduces the basic principles of fluorescence microscopy, the central experimental tool used throughout this work. It covers the fundamentals of fluorescence, optical microscopy techniques, such as brightfield, widefield and total internal reflection fluorescence (TIRF) microscopy.
- **Matter: Nanowires for optical biosensing**
  Focuses on semiconductor nanowires, their fabrication, and their optical properties. It discusses substrate grown GaP nanowires, substrate etched Si nanowires, as well as polymer embedded Si and Ga(As)P nanowires. It discusses how nanowires enhance light–matter interactions.

- **Life: Model biological systems and microfluidics**
  Describes the biological systems investigated in this thesis, including molecular beacons, streptavidin–biotin assays, and supported lipid bilayers. It also covers the design of microfluidic platforms used for controlled delivery of biomolecules to nanowire surfaces.

- **Machine: Computational modeling, simulation, and image analysis**
  Presents the computational framework developed for simulating light propagation in nanowires, generating artificial microscopy datasets, and processing experimental images. These methods form the analytical backbone of the thesis, bridging optical experiments with quantitative modeling and image analysis.

1.3 Overview of the included papers

This thesis is based on six research papers, each contributing to the overall aim of improving optical biosensing using semiconductor nanowires. Together, they address different aspects of materials engineering, biological applications, and computational analysis.

- **Paper I: Enhanced optical biosensing by Aerotaxy Ga(As)P nanowire platforms suitable for scalable production**
  Compares aerotaxially grown and substrate-grown nanowires, demonstrating the potential of scalable, cost-efficient production methods for optical biosensing. The results emphasize material quality, growth dynamics, and the suitability of aerotaxial nanowires for point-of-care (POC) applications.

- **Paper II: Sub-nanomolar detection of oligonucleotides using molecular beacons immobilized on lightguiding nanowires**
  Introduces nanowire-based molecular beacon systems capable of operating in a sub-nanomolar detection range. The work highlights the potential of nanowires for real-time, time-resolved fluorescence measurements, enabling dynamic monitoring of molecular interactions.

- **Paper III: Image analysis optimization for nanowire-based optical detection of molecules**
  Focuses on the computational techniques developed within this thesis to enhance image analysis for nanowire-based fluorescence data. It presents artificial dataset generation, ground-truth validation, and efficient algorithms for detecting labeled nanowires in both simulated and experimental datasets.

- **Paper IV: Comparative kinetics of supported lipid bilayer formation on silica coated vertically oriented highly curved nanowires and planar silica surfaces**

Explores the application of nanowires to study supported lipid bilayers as model biological membranes. The study demonstrates how nanowires can be used to investigate membrane-associated processes at the single-molecule level, bridging biosensing and membrane biophysics.

- **Paper V: Turning nanowires into off-plane molecular trackers through point spread function detection**
  Builds upon the computational framework of Paper III by extending analysis to obtain z-positions of molecules bound to nanowires from regular epifluorescence microscopes. The work establishes methods for determining axial positions of fluorophores, advancing toward true three-dimensional localization in nanowire-enhanced microscopy.

- **Paper VI: Lightguiding nanowires as a platform for biosensing in non-transparent media, including whole human blood**
  Demonstrates nanowire-based fluorescence detection in optically opaque and biologically relevant fluids such as blood. This study represents the final experimental step toward real-world applicability, highlighting the feasibility of nanowire biosensing in clinically significant environments.

And with this, *the library is open, because reading is what? Fundamental!**

*Reference to RuPaul's Drag Race

Chapter 2

Light: Optical microscopy and fluorescence

Light thinks it travels faster than anything but it is wrong. No matter how fast light travels, it finds the darkness has always got there first, and is waiting for it.

Terry Pratchett, Reaper Man

Light is essential part of optical detection of biological molecules. Hence, this chapter covers the key microscopy techniques used in this thesis, including brightfield microscopy, fluorescence microscopy, and total internal reflection microscopy.
The chapter starts with an introduction to the simplest form of optical microscopy- brightfield microscopy, which also serves as the foundation for other optical microscopy techniques. It then introduces to the basics of fluorescence, and, in particular, widefield fluorescence microscopy and total internal reflection fluorescence (TIRF).

2.1 Introduction to optical microscopy

Microscopes are central tools in the natural sciences and engineering, enabling observation of structures invisible to the naked eye. With early references to magnification appearing as far back as the 13th century, the first compound microscopes were constructed in the 16th century. By the 17th century, Robert Hooke and Antonie van Leeuwenhoek used microscopes to study cells and microorganisms, pioneering what would become the field of light microscopy. [35] Their work laid the foundation for brightfield microscopy, the simplest form of optical imaging.

When observing a point source of light through an objective lens, the image is not a perfect point but a blurred spot due to diffraction. This phenomenon imposes a fundamental resolution limit on optical microscopes known as the diffraction limit, first described by Ernst Abbe in 1873 [36]. According to Abbe's formula, the minimal resolvable distance d between two points is given by:

$$d = \frac{\lambda}{2n \sin \alpha} \tag{2.1}$$

where λ is the wavelength of light, n is the refractive index of the medium, and α is the half-angle of the cone of light entering the objective lens. This limit typically restricts optical resolution to approximately 100–200 nm for visible light, which is insufficient to resolve many biological structures such as proteins and DNA. [37] Although increasing the numerical aperture or using immersion media with higher refractive indices can improve resolution, these adjustments cannot surpass the fundamental diffraction barrier. [37]

To overcome this limit, a variety of super-resolution microscopy techniques have been developed, leveraging fluorescence and advanced optical methods to achieve resolutions beyond the diffraction limit. These methods operate within the framework of fluorescence microscopy, enhancing spatial resolution and enabling observation of molecular and subcellular structures beyond the brightfield microscopy foundation. [38]

2.1.1 Brightfield microscopy

Brightfield microscopy is an optical imaging technique in which the sample is illuminated with broad-spectrum white light, and the resulting image is formed by the light transmitted through the specimen. The term "brightfield" derives from the bright appearance of the background, as the majority of the illumination passes through transparent regions of the sample, while the specimen itself appears darker due to localized attenuation of light caused by absorption, scattering, or refractive index variations.

A conventional brightfield microscope comprises a white light source (e.g., halogen lamp or LED), a condenser lens system that focuses light onto the sample, a high numerical

aperture objective lens that collects transmitted light, and an eyepiece or camera for image observation and capture (see Fig. 2.2 a). Proper alignment of these optical components, typically achieved via Kohler illumination, ensures uniform illumination and optimal spatial resolution.

Due to its straightforward implementation, brightfield microscopy serves as a foundational method integrated within more advanced modalities such as phase contrast, differential interference contrast (DIC), and fluorescence microscopy, which enhance contrast or provide specific molecular information beyond absorption.

Brightfield microscopy allows direct visualization of stained biological samples, such as cells, tissues, and microorganisms, it is inherently limited by diffraction-limited resolution (typically 200nm) and low contrast in unstained, transparent specimens. These constraints necessitate complementary contrast-enhancing techniques for live-cell imaging or fine structural analysis.

The advantage of brightfield microscopy lies in its simplicity, ease of use, and ability to provide real-time imaging of samples without complex preparation. However, due to its limitations in resolution and contrast, lack of molecular specificity, thus, it is often supplemented with fluorescence microscopy techniques for detailed biological investigations.

2.2 Fundamentals of fluorescence microscopy

2.2.1 Introduction to fluorescence

Fluorescence is an optical phenomenon where a molecule absorbs light at a specific wavelength and then emits light at a longer wavelength. [39] The molecules that exhibit fluorescence are called fluorophores and they can be naturally occuring such as green fluorescent protein (GFP) from jellyfish *Aeqorea victoria* [40], or synthetically produced such as small organic dyes [41] and semiconductor quantum dots [42, 43]. A common way to explain fluorescence is through a Jablonski diagram [44], which illustrates the electronic states of a molecule and the transitions between them (Figure 2.1 b). The process starts when a fluorophore absorbs a photon and is excited from its ground singlet state (S_0) to an excited singlet state (S_1 or higher).

The molecule can radiatively relax to any of the vibrational states of the S_0 state, spontaneously emitting a fluorescence photon of energy equal to the energy difference between the states (with rate k_f). Similar to the excited state, the molecule then vibrationally relaxes to the lowest S_0 state. At room temperature, and since there are many atoms in a typical fluorophore, a continuum of vibrational levels of S_1 and S_0 are available for excitation and emission. This manifests as broad absorption and emission spectra, and the Stokes shift can

be attributed to the lowered energy due to the vibrational relaxations.

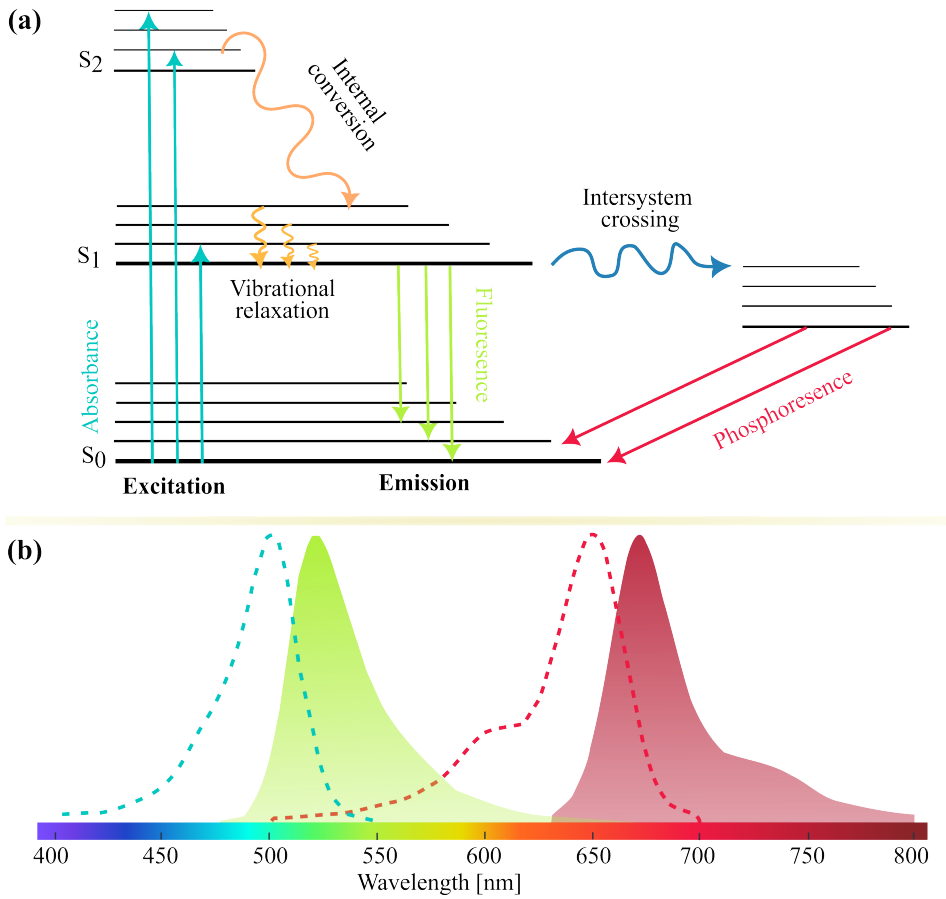

Figure 2.1: The basics of fluorescence.(a) Jablonski diagram illustrating the process of fluorescence. A molecule absorbs a photon and is excited to a higher energy state. It then relaxes to the lowest vibrational level of the excited state through non-radiative processes before emitting a photon and returning to the ground state. (b) Example absorption and emission spectra of two fluorophores, Alexa Fluor 488 (cyan/green) and Alexa Fluor 547 (red), showing the Stokes shift between excitation and emission wavelengths. These spectra are normalized to their respective maximum intensities for clarity, and are obtained from Thermo Fisher Scientific's SpectraViewer database. [45]

The molecules can also relax non-radiatively (k_{nr}) directly from S_1 to S_0, wherein the energy is dissipated to the vibrational modes, or through other long-lived transient states. The number of photons emitted by a fluorophore for a given number of photons absorbed can thus be defined by the ratio of radiative rate with respect to the total relaxation rate, known as the fluorescence quantum yield (Φ_{f}):

$$\Phi_{\mathrm{f}} = \frac{k_{\mathrm{f}}}{k_{\mathrm{f}} + k_{\mathrm{nr}}} \tag{2.2}$$

The spectral shift between absorption and emission, known as the Stokes shift (Figure 2.1 b), arises because the emitted photon has lower energy than the absorbed photon due to energy loss during vibrational relaxation. [39] This shift is crucial for fluorescence microscopy, as it allows for the separation of excitation and emission light using optical filters, enabling clear detection of the fluorescence signal against the background illumination.

2.2.2 Widefield fluorescence microscopy

Widefield or epifluorescence microscopy is one of the most fundamental imaging techniques used in biological imaging and research. Compared to brightfield microscopy techniques, fluorescence microscopy provides high-contrast imaging of specific molecules and structures by labelling them with fluorophores. In widefield fluorescence, the whole sample is illuminated simultaneously, and the emitted fluorescence is collected by same objective lens used for excitation. To guarantee spectral separation between excitation and emission light, the light path contains excitation and emission filters, as well as a dichroic mirror which can selectively reflect excitation light while transmitting the emitted light (see Fig. 2.2 b-c). [46–48]

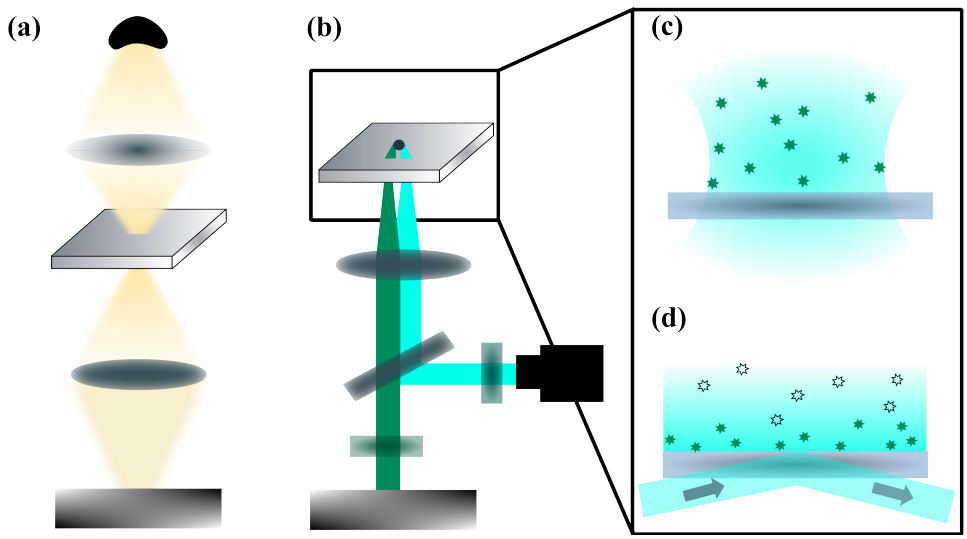

Figure 2.2: Schematics of a (a) brightfield and (b) widefield fluorescence microscope, both with an inverted objective setup. (a) In brightfield microscopy, the sample is illuminated with white light from above, and the transmitted light is collected by the objective lens to form an image. (b) In widefield fluorescence microscopy, the excitation light from the light source is filtered through an excitation filter and directed towards the sample by a dichroic mirror. The emitted fluorescence from the sample passes back through the dichroic mirror and is filtered by an emission filter before being detected by the camera. (c) and (d) show example images of widefield and total internal reflection setups, respectively.

Widefield microscopy often deploys inverted microscope configuration, where the objective lens is positioned below the sample, making it easier to image cells and tissues. However,

fluorescence excitation of the whole sample volume also produces out-of-focus background from fluorophores outside focal plane, thus reducing signal-to-noise ratio (SNR) and contrast. Several techniques have been developed to overcome this limitation, including confocal microscopy, total internal reflection fluorescence (TIRF), and light sheet microscopy.

2.2.3 TIRF microscopy

One of the most common ways to overcome the out-of-focus signal is total internal reflection fluorescence (TIRF) [49, 50], where only the molecules attached to the glass are excited, as an evanescent field is created at the glass-aqueous solution interface due to the mismatch of the refractive indices, [51] as can be seen in Figure 2.2 d. The specific critical angle θ_{critical} at which the total reflection happens is defined as:

$$\theta_{\text{critical}} = \sin^{-1}\left(\frac{n_1}{n_2}\right) \tag{2.3}$$

where n_1 is the refractive index of the solution or cell interior and n_2 is the refractive index of glass. The depth of the evanescent field (Eq. (2.4)) is a function of incident illumination angle, wavelength, and refractive indices with an exponentially decaying intensity (Eq. (2.5)) of the coverglass.

$$d = \frac{\lambda_0}{4\pi\sqrt{n_2^2 \sin^2\theta - n_1^2}} \tag{2.4}$$

$$I_z = I_0 e^{-z/d} \tag{2.5}$$

Chapter 3

Matter: Nanowires for optical biosensing

'Cause this is a material world...

Madonna, Material Girl

... and this chapter is about materials: semiconductor nanowires. It covers the growth and fabrication methods of used nanowires, as well as the optical properties that make them a favorable tool for sensitive fluorescence detection.

3.1 Semiconductor nanowires for optical biosensing

Nanowires are one-dimensional nanostructures typically characterized by diameters ranging from a few to several hundred nanometers and lengths that can extend from hundreds of nanometers to several micrometers. [52, 53] The combination of their small diameter and large length gives rise to very high aspect ratios (length-to-diameter), which leads to physical and chemical behaviors markedly different from those of the corresponding bulk materials. [54] Nanowires can be synthesized from a wide variety of materials [55], including metals [56], semiconductors [57], and insulators [58].

Semiconductor nanowires, in particular, have gained significant applications in electronics, solar cells, sensors, and photonics. [53, 59] III-V semiconductor nanowires, such as gallium arsenide (GaAs) [60], indium phosphide (InP) [21], and gallium phosphide (GaP) [61, 62], are of particular interest due to their direct bandgap, high electron mobility, and tunable optical properties. Rigorously studied in the context of nanowire-based lasers, light-emitting diodes, solar cells, and photodetectors, semiconductor nanowires have also shown great promise in biosensing applications. In this thesis, we focus on GaP nanowires, which have a high refractive index and low absorption in the visible spectrum, making them suitable for fluorescence enhancement applications. [20, 24]

While III-V semiconductor nanowires have been extensively studied, and proven to be effective for biosensing as well, [20, 21] one of the shortcomings is their relatively high cost and complex fabrication methods. Silicon (Si) nanowires, on the other hand, are more abundant, biocompatible, and can be fabricated using top-down approaches, making them a more scalable and cost-effective option for biosensing applications. [63, 64] The established application range of Si in biological experiments due to its biocompatibility and ease of surface functionalization due to native oxide on the surface makes Si nanowires a good candidate for biosensing applications. When III-V semiconductor, especially GaP and Ga(As)P nanowires are used in this work, SiO_2 coating is applied on their surface, providing a biocompatible surface for functionalization and binding of biological molecules.

One of the key advantages of using these semiconductors is their high refractive index, which allows for strong light confinement and waveguiding properties. In this section, we will qualitatively describe the main optical properties of nanowires that make them suitable for fluorescence enhancement applications. A more quantitative description of these effects, as well as the numerical methods used to simulate them, are described in section 5.1. Other advantages include high surface-to-volume ratio, and the added simplicity of performing single nanowire localization.

3.1.1 Signal enhancement by nanowires

Semiconductor nanowires address certain limitations of conventional fluorescence assays by enhancing the signal-to-noise ratio (SNR) in detection. This is achieved by increasing the area available for interaction between the surface and the analyte, and by providing an optical signal enhancement. [24, 25] The later stems from the unique optical properties of nanowires, which can collect and guide light efficiently and enhance the excitation and emission processes of fluorophores located in their vicinity. [20, 26, 27]

In this section, we provide a concise overview of the primary mechanisms responsible for fluorescence enhancement in nanowires. This qualitative discussion is complemented by Section 5.1, where we present the numerical methods used to quantify, characterize, and simulate these effects.

The waveguiding properties of nanowires can be described by considering it as an optical fiber, the number of modes of which are given by:

$$V = \pi \frac{d}{\lambda} \sqrt{n_f^2 - n_{cl}^2} \tag{3.1}$$

where λ is the wavelength of the fluorophore, d is the nanowire diameter, n_f is the refractive index of the nanowire and n_{cl} is the refractive index of the cladding material [20]. In the context of this thesis, the cladding material is typically an aqueous solution ($n_{cl} = 1.33$), where biological molecules are suspended. For values $V < 2.4$, the fiber is considered to have a single mode, where the light is coupled to a fundamental mode H_{11} [20, 21]. In this work, we use nanowires of GaP ($n_f = 3.34$) and Si ($n_f = 4.01$). For both materials, the diameters of nanowires range between $110 - 120$ nm, and fluophore excitation wavelength is 640 nm, which ensures single mode operation for used fluorophores. In general, the fields of optical waveguides consist of two components: one describes the energy travelling in the direction of waveguide axis (*guided energy*), while the other describes the energy extending outside the waveguide core (*radiated energy*). [65, 66]

Also known as leaky modes, the radiated energy component, decaying exponentially away from the waveguide and propagating into surrounding medium. This evanescent field results in an enhancement, called *excitation enhancement* (η_{ex}). This contribution was studied both computationally and experimentally, and was proven to contribute significantly in fluorescence enhancement. [27] The excitation enhancement heavily depends on the wavelength of the incident light, incident angles, the numerical aperture of the microscope objective, as well as the position of the fluorophore on nanowire vertical axis. [67] When including η_{ex} in overall enhancement calculations, the consideration is made that excitation occurs in the linear regime, meaning that the excitation intensity is low enough to avoid saturation of the fluorophore. [67]

In addition to excitation enhancement, there is an *emission enhancement*, which relates to

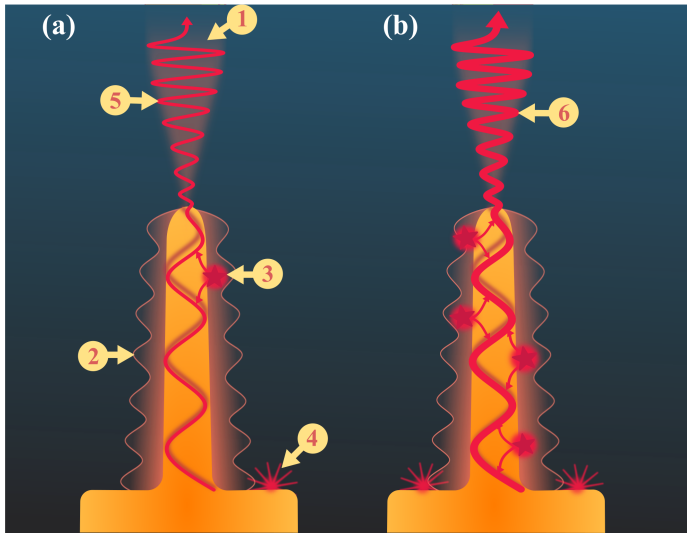

Figure 3.1: Lightguiding nanowire with (a) one bound molecule and (b) multiple bound molecules. (1) the incoming excitation light and (2) is the evanescent field around the nanowire causing excitation enhancement. (3) is an illustration of a fluorophore bound to the surface of the nanowire, with enhanced, coupled emission, while (4) is a fluorophore bound to the substrate, emitting modified by the presence of the substrate. (5) and (6) demonstrate the guided emission from a nanowire with one and multiple bound fluorophores, respectively.

the modification of the fluorophore quantum yield and de-excitiation time constant. When coupled to a nanowire, the radiative relaxation rate (see Eq. 2.2) is modified by the Purcell factor (C_{Purcell}) [68, 69]:

$$k'_{\mathrm{rad}} = C_{\mathrm{Purcell}} k_{\mathrm{rad}} \tag{3.2}$$

C_{Purcell} would be greater than 1 in case of an enhanced radiative rate, and equal to 1 in case of no modification as for a free flurophore in aqueous reference solution (see Section 5.1.2 for more details).

When using fluorophores with a QY significantly lower than 1, as in the case of Alexa Fluor 647, the enhancement of emission (η_{em}) is attributed mainly to the increase of quantum yield, as the enhancement due to de-excitation time modification is negligible [67]. Another important consideration about η_{em}, is the fact that in contrast to excitation enhancement, it does not depend on the excitation or collection NA [67].

The final enhancement property, the *collection enhancement* (η_{col}) is defined as:

$$\eta_{col} = \frac{\psi'}{\psi_0} \tag{3.3}$$

where ψ' and ψ_0 the collection probabilities from nanowires and reference medium.

The overall enhancement of a single fluorophore by an individual NW is multiplicative and can be described as:

$$\eta = \eta_{exc} \cdot \eta_{em} \cdot \eta_{col} \tag{3.4}$$

These enhancement factors can be obtained from numerical solutions of Maxwell's equations as described in section 5.1. It should be noted that absorption losses in the nanowire material will affect the overall enhancement. In practice, absorption loss can be directly included in near field calculations of enhancement factors.

In case of multiple fluorophore binding (see Figure 3.1), axially averaged enhancement factors can be considered. In addition to fluorescence enhancement, the available surface of nanowires allows multiple fluorophore binding on a single NW, resulting in combined signal from individual NWs.

3.1.2 Surface area-to-volume ratio

Another key advantage of employing nanowires in biosensing applications is their exceptionally high surface-to-volume ratio, which substantially increases the available surface area for biomolecular immobilization and interactions. The surface area of an individual nanowire can be approximated by that of a truncated cone, expressed as:

$$S_{NW} = \pi l(r_{top} + r_{bottom}) + \pi r_{top}^2, \tag{3.5}$$

where $l = \sqrt{(r_{top} - r_{bottom})^2 + h^2}$ is the slant height, r_{top} and r_{bottom} denote the top and bottom radii, respectively, and h is the nanowire height. The bottom facet is in contact with the substrate and therefore excluded from the accessible surface area. The corresponding nanowire volume is given by:

$$V_{NW} = \frac{1}{3}\pi h \left(r_{top}^2 + r_{bottom}^2 + r_{top} r_{bottom}\right). \tag{3.6}$$

For a representative nanowire with $h = 2.5\,\mu\text{m}$, $r_{top} = 0.055\,\mu\text{m}$, and $r_{bottom} = 0.060\,\mu\text{m}$, the calculated surface area and volume are approximately $S_{NW} \approx 0.9\,\mu\text{m}^2$ and $V_{NW} \approx 0.025\,\mu\text{m}^3$, respectively. This corresponds to a surface-to-volume ratio of $S_{NW}/V_{NW} \approx 36\,\mu\text{m}^{-1}$, highlighting the strongly surface-dominated nature of nanowire geometries. Such a high ratio is a defining characteristic of one-dimensional nanostructures and is central to enhancing the sensitivity of biosensors by maximizing the number of available binding sites per unit volume. [70–72]

Because biological molecules are typically only a few nanometers in size, this high surface-to-volume ratio enables efficient binding even at very low analyte concentrations. Further-

more, unlike planar surfaces where steric hindrance and molecular crowding limit receptor loading, nanowires provide an inherently three-dimensional architecture. This geometry increases the effective binding capacity and supports a more homogeneous molecular distribution, ultimately resulting in enhanced signal strength and sensitivity. [71, 73]

3.1.3 Single nanowires as individual sensors

The unique optical enhancement properties of nanowires [20, 26, 29] make them exceptionally well-suited for sensitive single-molecule detection. Beyond their role in amplifying fluorescence signals, nanowires offer further advantages due to their spatial separability and the ability to localize individual nanowires within a field of view. This enables what can be termed digital enhancement, where each nanowire acts as an independent, addressable sensor. Such digital enhancement not only improves detection sensitivity but also facilitates robust statistical analysis and multiplexed measurements, as discussed in the context of fluorescence image analysis and detection below.

First, once placed under a widefield fluorescent microscope, thousands of single-nanowire sensors come into view within the field of view (FOV), also showing an improvement in their effectiveness because of their large quantity. The large number of nanowires, which serve as spatially resolved binding sites in FOV, accompanied by the ability to detect single molecules, allow us to (i) extract intensity and concentration information based on a large statistical set of events and/or (ii) simultaneously monitor biophysical processes in one FOV.

Second, the uniform height and lateral displacement of nanowires allow us to obtain and maintain an imaging plane corresponding to nanowire tips and to predetermine nanowire locations without fluorescence excitation. This can be accomplished by one of the simplest microscopy techniques, brightfield microscopy, which allows determining the axial and lateral positions of nanowires, offering the benefits of focusing on the sample and defining regions of interest (ROI) without the risk of photobleaching.

And finally, we emphasize that taking into account both nanowire localizations and integrated intensities over individual nanowires, a large linear-dynamic range of concentration-based experiments can be explored.
The large part of this work is dedicated on developing reliable analysis techniques to perform nanowire-enhanced fluorescence microscopy as accurately as possible, where the advantages of brightfield image acquisition will be described more in details. However, before delving into the details of image processing techniques and methods, we describe the selected three metrics to evaluate the performance of nanowire biosensors in each frame of the image:

1. the digital count of bright nanowires (N), which is significant in low-concentration detection regimes, where the main contribution in the signal increase is by the in-

creasing number of bright nanowires,

2. the average pixel intensity per bright nanowire ($\bar{I}_i$), which is proportional to the number of fluorophores bound to individual nanowires. In low concentration regimes, where only few nanowires are lit, this value should not have a large variation, However, the intensity of individual nanowires will still vary due to the dependence of the combined enhancement factor on the fluorophore binding position,

3. the overall pixel intensity emitted from bright nanowires (I_{tot}), which, being the sum of intensities over all bright nanowires, incorporates the advantages of nanowire digital count and intensity integration along the nanowire axis.

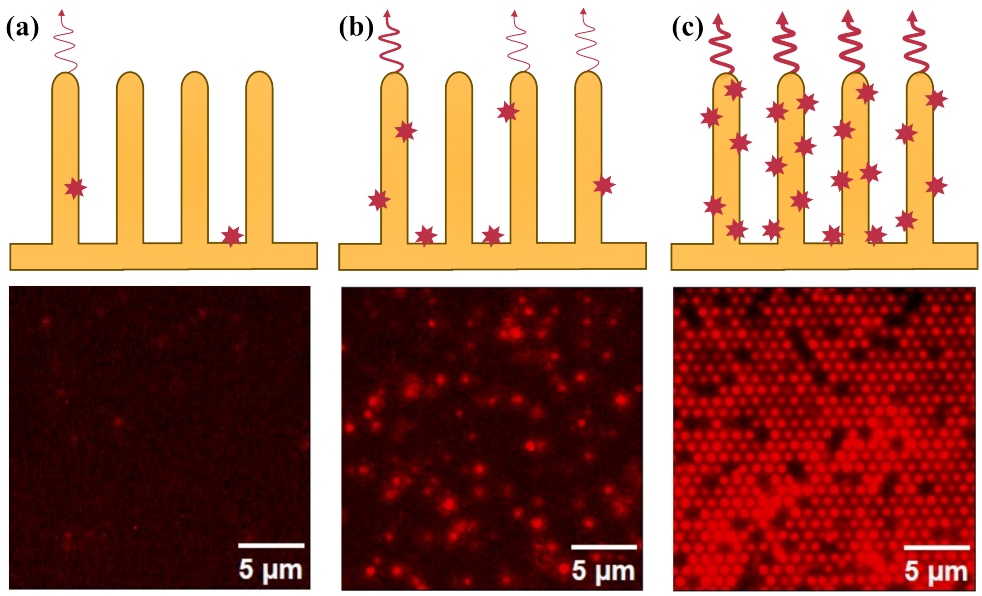

Figure 3.2: The different regimes of nanowire surface coverage. (a) 10 fM: very small amount of molecules is bound to NWs and the substrate and the emitted intensity per nanowire is low. (b) 10 pM: Around half of the nanowires are bright, but the intensity of nanowires varies due to difference in the number of bound molecules (c) 10 nM: All nanowires are bright and multiple molecules bound to them.

3.2 Nanowire growth and fabrication

Generally, nanowire fabrication methods can be classified into two categories: bottom-up and top-down approaches. [74, 75] The bottom-up approaches include the methods where nanowires are grown from atomic or molecular precursors, while in the top-down approaches, nanowires are fabricated by etching or patterning a bulk material. As mentioned earlier, two types of semiconductor nanowires are used in this work - GaP and Si.

GaP nanowires were grown by two bottom-up approaches: metalorganic vapour-phase epitaxy (MOVPE) and aerotaxy, while Si nanowires were fabricated by a top-down approach, where they were etched from a silicon wafer.

In the context of this thesis, which focuses on computational and experimental techniques to advance biosensing, yet another classification of nanowire platforms can be made – periodic nanowire arrays on a wafer of same material and randomly positioned, polymer embedded nanowires. This distinction is significant in the framework of this thesis, as both imaging and image analysis techniques are influenced by nanowire arrangement. We will later show that the periodicity of nanowire arrangement can be exploited in image analysis, namely using frequency domain based techniques. On the other hand, randomly positioned nanowires embedded in a polymer matrix offer a more flexible and scalable platform for biosensing applications, allowing them to be integrated into various microfluidic devices.

3.2.1 GaP nanowires by MOVPE

GaP nanowires along other III-V semiconductor nanowires, are typically grown by metalorganic vapour-phase epitaxy. [76] The term *epitaxy*, originally derived from the Greek words *epi* (above) and *taxis* (arrangement), is a chemical vapor deposition method that refers to the ordered growth of a crystalline layer on a crystalline substrate.

A crucial step achieving well-defined and periodically distributed nanowires is achieved through displacement Talbot lithography (DTL) [77, 78], which uses Talbot self-imaging effect [79] to create high-uniformity nanoscale hole patterns. In this case, the pattern is transferred to a double layer of disposed resists on a GaP (111)B substrate – a bottom antireflection coating (BARC) and deep-ultraviolet resist (DUVR). Eventually, the pattern is transferred to the SiN_x hard mask by reactive ion etching (RIE). Thanks to this, a hexagonal array of holes with a diameter of approximately 120 nm and a pitch of around 1 µm is created in the SiN_x layer, which serves as a mask during gold (Au) deposition. Au ($\approx$ 120 nm) deposition is followed by SiN_x mask removal, resulting a patterned array of gold particles on the substrate.

During MOVPE growth, the substrate temperature is elevated and metal organic precursors trimethylgallium (TMGa) and phosphine (PH_3) are introduced in the reactor chamber. Hydrogen chloride (HCl) is also introduced at this stage to decouple radial and axial growth of GaP nanowires. [80] The gold particles serve as catalysts for the vapor-liquid-solid (VLS) growth mechanism. [81, 82] This term derives from the presumed three phases involved in the growth: vapor phase of the precursors, liquid phase of the seed particle, and solid phase of the semiconductor. When the precursors reach the gold particles, they decompose and dissolve in the gold, forming a liquid alloy droplet. Once it gets supersaturated, nanowire

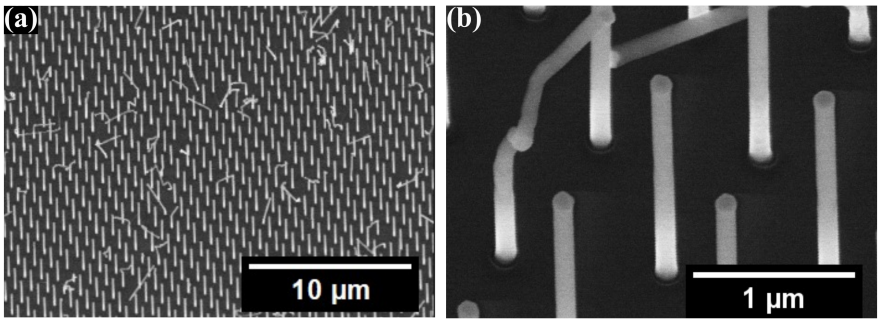

Figure 3.3: Scanning electron microscopy (SEM) images of GaP nanowires grown by MOVPE with (a) 10 µm and (b) 1 µm scale bars. The images were acquired at AlignedBio AB (Lund, Sweden).

growth is initiated. [83, 84] By controlling growth parameters such as temperature, pressure, precursor flow rates, and growth time, the desired length and diameter of the NWs can be achieved.

The final step in fabrication is 10 nm silica (SiO_2) coating of the nanowires by atomic layer deposition (ALD). [85] The silica coating serves mainly two purposes: (i) it passivates the surface of the nanowires, smoothing out surface defects, and (ii) it provides a biocompatible surface for functionalization and binding of biological molecules. The thickness of the silica layer is optimized to be thin enough not to significantly affect the optical properties of the nanowires, while still providing sufficient surface coverage for functionalization.

Alongside silica coating, the displacement pitch of nanowires is another crucial parameter for bio-imaging. In this work, a pitch of 1 µm is selected, which is large enough to avoid optical coupling between nanowires and allows individual nanowire imaging because their separation exceeds the microscope's diffraction limit. It can be observed in Figure 3.3 that the nanowires have a high degree of uniformity in terms of diameter and height, however, around $10-15\%$ of the nanowires are kinked or missing due to imperfections in the growth and lithography processes. These nanowires are generally considered not to contribute to the fluorescence signal enhancement.

3.2.2 Ga(As)P nanowires by aerotaxy

Aerotaxy nanowires, as the name suggests from the Greek words *aero* (air) and *taxis* (arrangement), are synthesized using a bottom-up approach in a continuous flow reactor. [86, 87] Unlike conventional MOVPE, which requires a crystalline substrate for nanowire growth, aerotaxy enables high-throughput production of free-standing nanowires in a continuous gas-phase process—achieving up to 50 times faster production rates. [86]

Similar to MOVPE, aerotaxy relies on VLS growth mechanism, employing gold nanopar-

ticles as catalysts. The same precursors for group III and V elements, trimethylgallium (TMGa) and phosphine (PH_3), are used in the reactor. Size-selected Au nanoparticles are mixed with TMGa at a temperature near 430°C, suitable for forming liquid Au-Ga alloy droplets. This mixture is carried by a nitrogen gas stream into the phosphine atmosphere, where phosphorus dissolves into the alloy. Growth initiates upon reaching supersaturation in the liquid droplet, triggering nucleation of the solid crystalline nanowire. While subsequent nucleation events may occur at different sites on the catalyst, the crystallographic orientation of the resulting crystallites is governed by the balance of surface and interface energies. Fast-growing facets diminish, leaving the more stable, slow-growing facets that define the nanowire shape. [88]

The growth of this NWs was aimed to be similar to GaP nanowires, however, the residual content of arsenic (As) in the reactor led to the formation of Ga(As)P nanowires with a small fraction of As incorporated into the crystal structure. [89]

After gradual cooling to room temperature upon reactor exit, the nanowires are collected on filters. Post-growth, they are coated with a 30 nm SiO_2 shell by atomic layer deposition (ALD), similar to the coatings applied to MOVPE-grown nanowires. The final step involves aligning the nanowires in a polymer matrix (see Fig. 3.4 c-f). [90]

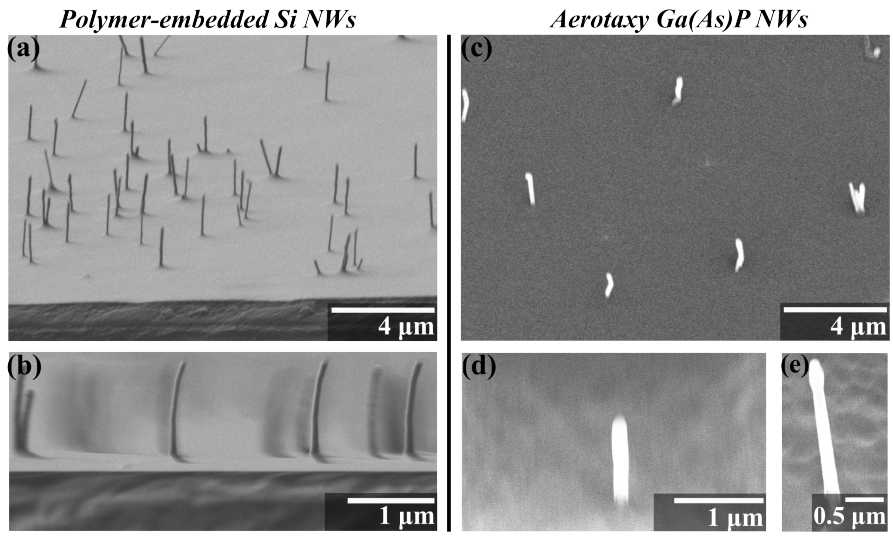

Figure 3.4: SEM images of polymer embedded nanowires. (a-b) Si nanowires fabricated by top-down etching, (c-d) Ga(As)P nanowires synthesized by aerotaxy. The images were acquired at AlignedBio AB (Lund, Sweden).

3.2.3 Si nanowires by top-down etching

Silicon wafers with a (100) orientation were patterned using displacement Talbot lithography (DTL). The patterning process began by depositing a double resist layer, consisting of a bottom antireflection coating (BARC, SF 3S) followed by a deep-ultraviolet resist (DUVR, PAR1085S90). To further reduce the diameter of the patterned holes, a shrink resist (AZSH-114A) was applied on top of this bilayer.

Exposure of the resist was conducted using a PhableR 100 deep-ultraviolet lithography system (EULITHA AG, Switzerland), which generated a hexagonal array of holes measuring 120 nm in diameter, arranged with a pitch of 1 µm, corresponding to a hole density of approximately 1.19 μm^{-2}.

Subsequently, chromium seed nanoparticles were deposited onto the patterned substrate by electron-beam evaporation. The resist layers were then removed by lift-off in acetone heated to 100 °C. Silicon nanowires were grown from the chromium seeds using anisotropic dry plasma etching, following established silicon etching protocols as described in the literature. [91]

3.2.4 Polymer embedded Si nanowires

Both Ga(As)P and Si nanowires were embedded in an optically transparent polymer matrix vertically aligned using a proprietary technology developed by AlignedBio AB (Lund, Sweden). Hence, the details of the process are not disclosed here.

The etched nanowires were harvested from the wafer surface and transferred into polymer films in a random vertical orientation. Large polymer blocks were then sectioned into smaller pieces approximately 2.5 mm $\times$ 2.5 mm for further characterization and application (see Fig. 3.4 a-b).

Chapter 4

Life: Model biological systems and microfluidics

There is no end to what a living world will demand of you.

Octavia E. Butler, Parable of the Sower

Detecting biological molecules is, indeed, demanding. This chapter is a brief overview of the biological systems we study, the molecular tools we use, and the microfluidic devices we employ. As we aim to investigate light-guiding nanowires as tools for sensitive and quantitative detection of biological molecules, we investigate multiple model systems. These include well-studied systems, such as the streptavidin-biotin assay and molecular beacons, as well as more complex systems such as lipid bilayer formation. Microfluidic devices used to study these systems are described here. Finally, we also delve into optically non-transparent media, such as lipid emulsions and blood are discussed in the context of biosensing.

4.1 What are biosensors?

Having discussed the principles of fluorescence microscopy, the synthesis and unique properties of semiconductor nanowires in the preceding sections, we now turn to the question of how these elements can be integrated into practical analytical devices. To place it in context, it is essential to clarify what biosensors are.

A biosensor is an analytical device that combines a biological recognition element with a physical transducer to detect and quantify a specific analyte. The biological recognition element, such as an antibody, enzyme, nucleic acid, provides specificity for the target analyte. The transducer then converts this binding event into a measurable signal, which may take the form of optical, electrical, or mechanical changes. In fluorescence-based biosensors, the binding event leads to a change in fluorescence intensity, wavelength, lifetime, or related optical properties that can be quantified with appropriate sensitivity. Often, biosensors incorporate a signal amplification unit to improve the LOD and dynamic range of low abundance analytes. Finally, a display or readout system presents the results, ranging from simple colorimetric changes to complex digital interfaces. [5, 92]

In this thesis, we explore the use of waveguiding semiconductor nanowires as an optical signal - enhancement element in fluorescence-based biosensing. As a first model, fluorescently labeled streptavidin is used as an analyte binding to pre-functionalized nanowire surfaces. This model system does not constitute a clinically deployable biosensor, since the fluorophore is already conjugated to the analyte. However, it provides a well-characterized platform to evaluate optics-governed detection limits, to identify biology-imposed constrains, and to improve quantification capabilities. In this context, nanowires act as both the substrate for analyte binding and optical transducer. The resulting fluorescence signal is collected as an image and analyzed to extract spatial intensities and nanowire counts for quantitative readout curve.

To evaluate the potential of nanowires for more complex and optically challenging environments, we investigate the performance of nanowires in non-transparent biological media, such as blood, milk, and lipid emulsions. Finally, we explore the use of nanowires in conjunction with molecular beacons (MB) for the detection of specific oligonucleotide sequences, moving closer to clinically relevant biosensing applications. The study using supported lipid bilayer (SLB) systems further expands the scope of nanowire-based biosensors creating a platform for investigating membrane-associated biological processes, and studying time-resolved events in a controlled microenvironment.

4.1.1 Molar concentration of biological molecules

To quantitatively interpret the fluorescence signals obtained from nanowire-based biosensing, whether using model proteins or nucleic-acid probes, it is essential to relate the measured optical response to the actual number of molecules present in the system.

The concentration of biological molecules is typically expressed in terms of molarity (M), defined as the number of moles of solute per liter of solution. One mole corresponds to 6.022×10^{23} molecules, known as Avogadro's number.

Molecular weight, commonly expressed in Daltons (Da), where 1Da is one-twelfth the mass of a carbon-12 atom, is equivalent to grams per mole (g/mol) and represents the mass of one mole of a substance.

Expressing concentration in molarity rather than mass concentration (e.g., mg/mL) is preferred in certain cases because molarity provides a direct measure of the number of molecules present in a given volume. This is crucial for stoichiometric calculations, binding kinetics, and quantitative comparisons across different molecules or assays. In contrast, mass concentration does not account for molecular size or mass differences between analytes, which affects the actual number of molecules involved in interactions.

The conversion from mass concentration to molarity is given by:

$$\text{Molarity (M)} = \frac{\text{Mass concentration (mg/mL)} \times 1000}{\text{Molecular weight (g/mol)}}$$

This relationship links measurable mass units to molecular counts, enabling precise and meaningful interpretation of biosensing data.

4.2 Model biological systems

4.2.1 Streptavidin-biotin assay as a model system

One of the strongest non-covalent interactions in biology is the binding between avidin and biotin [93]. Avidin consists of four identical subunits, each capable of binding to one biotin molecule with a dissociation constant $K_d \approx 10^{-15}$M. [94] In research and biotechnology, streptavidin, a bacterial analog of avidin, is more commonly used. [95] Streptavidin has a slightly lower affinity for biotin ($K_d \approx 10^{-14}$ M) but is less positively charged and has a lower tendency for non-specific binding [96, 97]. Due to its high affinity, specificity, stability, and versatility, the streptavidin biotin system is widely used in various ap-

plications, including immunoassays, protein purification, drug delivery, biosensing, and bioimaging. [98]

Streptavidin is a relatively large protein with a molecular weight of $\approx$ 56 kDa. [94] Biotin is much smaller with a molecular weight of $\approx$ 240 Da. [96] It can be chemically conjugated to a wide range of molecules without significantly affecting their biological activity. [99] In the context of biosensing, biotin can attach to a surface-binding molecule, and various concentrations of fluorescently labeled streptavidin can be used as a model analyte. This simplicity and robustness makes it an attractive assay for testing new biosensing platforms, such as lightguiding nanowires.

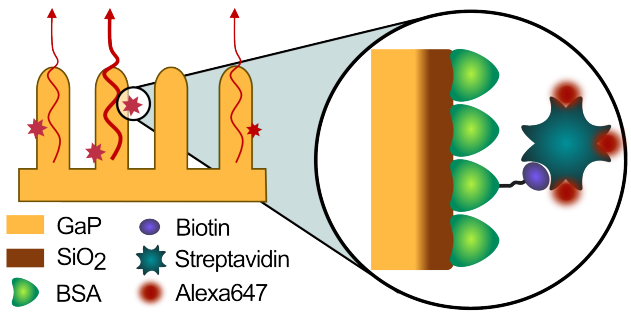

Figure 4.1: bBSA is adsorbed to the coating layer of nanowire, covering both the nanowires and the substrate. Streptavidin labelled with AlexaFluor647 (StvA647) dye is bound to bBSA with high affinity

Nanowires which are typically coated with a thin layer of silica can be functionalized with biotinylated bovine serum albumin (bBSA). BSA is a commonly used protein for blocking non-specific binding and passivating surfaces [100]. It can attach to a silica surface through adhesion [101], while the biotin molecules provide specific binding sites for streptavidin. By incubation bBSA passivating nanowires with different concentrations of fluorescently labeled streptavidin, we can investigate the sensitivity and quantification capabilities of nanowires as a biosensing platform. Figure 4.1 illustrates the binding of streptavidin to bBSA-functionalized nanowires.

4.2.2 Molecular beacons for oligonucleotide detection

During the early stages of disease progression, elevated concentrations of specific biomarkers, such as nucleic acid sequences, can serve as critical indicator of disease presence. Cell-free DNA and various RNA species, are particularly attractive biomarkers, as their concentrations and molecular concentrations often correlate with disease onset, stage and response to treatment. [102, 103] Thus, sensitive and specific detection of nucleic acids is crucial in early detection, prognosis, and longitudinal disease monitoring. [104–106]

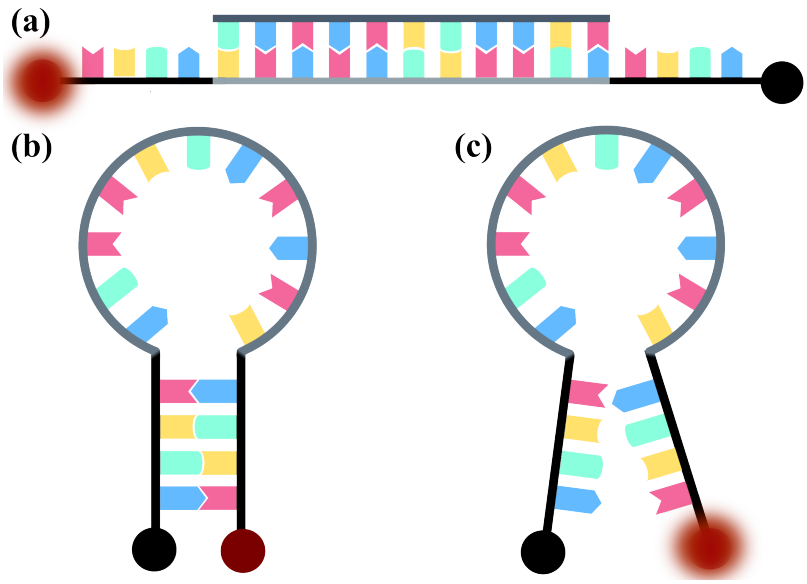

Figure 4.2: Schematic representation of a molecular beacon in three states: (a) duplex state (hybridized to target), (b) closed hairpin state (quenched fluorescence), and (c) open state (unhybridized).

Several analytical platforms are available to detect specific nucleic acid sequences. Perhaps one of the most widely known methods is polymerase chain reaction (PCR) which is used to enzymatically amplify target DNA sequences, thereby increasing their abundance above the detection limit, providing sensitive quantification. Next-generation sequencing (NGS) assays are high-throughput methods that allow simultaneous sequencing of large amount of DNA or RNA molecules. FISH (fluorescence in situ hybridization) uses fluorescently labeled probes that hybridize to complementary nucleic acid sequences within cells or tissues, enabling spatially resolved visualization of specific genomic loci or transcripts. [107] PCR and NGS require complex sample preparation, specialized equipment, and oftentimes require lysis or homogenization of cells and tissues to extract the nucleic acids. FISH, on the other hand, allows for direct visualization of nucleic acids within their native cellular or tissue architecture, but it requires fixation and permeabilization of the cells or tissues.

A particularly versatile strategy for fluorescence-based nucleic acid detection is the use of molecular beacons (MB). MBs are single-stranded oligonucleotide probes engineered to form a hairpin-like stem-loop structure. A fluorophore and a quencher are covalently attached to opposite ends of the stem. [108, 109] In the absence of the target oligonucleotide sequence, the fluorophore and quencher are in a close proximity, resulting in efficient quenching of fluorescence, typically via fluorescence resonance energy transfer or contact quenching (see Fig. 4.2 a-b). Upon hybridization of the loop with a complementary sequence, the hairpin structure opens, effectively separating the fluorophore and quencher. The prob-target event thus leads to a significant increase in fluorescence signal, resulting

a strong and time-resolved readout. MBs can exhibit high specificity, due to the requirement of precise base-pairing upon hybridization, can be widely applied in real-time PCR, live-cell imaging, and in wider biosensing.

4.2.2.1 MB kinetics

MB can exist in three primary phases: (1) the duplex state, where it is hybridized to the target sequence; (2) the closed state, featuring a hairpin structure with quenched fluorescence; and (3) the open state, where the hairpin is open but not hybridized to the target (see Fig. 4.2). We are primarily interested in the transition between the closed and duplex states, as this directly correlates with the concentration of the target oligonucleotide. However, when aiming to improve the limit of detection (LOD) of MB-based biosensors, phase (3) must be considered, as it sets a limit on the minimum target concentration that can be detected. [110]

The dissociation constant K_{2-3} describing the equilibrium between the closed hairpin conformation and the random coil state of molecular beacons can be expressed in terms of fluorescence intensities as

$$K_{2-3} = \frac{F(\theta) - \beta}{\gamma - F(\theta)}, \tag{4.1}$$

where $F(\theta)$ is the fluorescence intensity measured at temperature θ, β corresponds to the fluorescence of molecular beacons in the closed hairpin form, measured at low temperature (e.g., $10^{\circ}\mathrm{C}$), and γ represents the fluorescence in the fully unfolded random coil state at a high temperature (e.g., $80^{\circ}\mathrm{C}$), all measured in the absence of target sequences. [111, 112] This ratio provides a quantitative measure of the conformational equilibrium by relating fluorescence signals to the relative populations of folded and unfolded beacon states.

According to Tsourkas et al. [111], the correlation between fluorescence intensity and temperature allows determination of the enthalpy change ΔH_{2-3} and entropy change ΔS_{2-3}:

$$R \ln K_{2-3} = \frac{\Delta H_{2-3}}{\theta} - \Delta S_{2-3}, \tag{4.2}$$

where R is the universal gas constant (1.9872 cal mol^{-1} K^{-1}) and θ is the absolute temperature in Kelvin.

The dissociation constant K_{1-2}, characterizing the equilibrium between the molecular beacon–target duplex and the stem–loop hairpin, can be derived from fluorescence melting data obtained in the presence of the target [111]. It is expressed as:

$$K_{1-2} = \frac{(\alpha - F(\theta))T_0}{(F(\theta) - \beta) + (F(\theta) - \gamma)K_{2-3}}, \tag{4.3}$$

where T_0 is the target concentration, α is the fluorescence intensity of the molecular beacon–target duplex measured at low temperature (e.g., $15°C$), and F, γ, and β are fluorescence intensities previously defined in Equation (4.2).

Tsourkas et al. [111] also describe the temperature dependence of MB-target hybridization kinetics. Around the melting temperature ($\theta_M \approx 54°C$), the hairpin opens, resulting in similar fluorescence intensities in the presence or absence of target. At lower temperatures, although less pronounced, a slight fluorescence increase occurs even without target, but it remains significantly lower than in the presence of target.

In the context of this thesis, we do not perform detailed kinetics analysis; however, understanding these principles is essential for understanding MB-based biosensing assays using lightguiding nanowires. Possible effects such as sample heating by laser illumination, local environmental variations, and immobilization on solid surfaces can all influence hybridization kinetics. [113, 114] Several factors, such as surface charge [115], brush effects [116], and surface curvature [117] may be play a significant role when immobilizing MBs on semiconductor nanowire. Other important factors also include the length of the stem and loop regions [118], as well as the ionic strength and composition of the surrounding buffer [119]. Different MB may respond differently to different salt concentrations, namely monovalent (e.g., NaCl) and divalent (e.g., $MgCl_2$) ions, which can stabilize or destabilize the hairpin structure, which could be attributed to the differences in their backbones and constructions. [120]

4.2.2.2 MB design and immobilization

The design of MBs is fundamental for their biosensing function, although detailed optimization and testing of sequences were not performed here. For detecting *ABL1* mRNA, a target region was selected using the NCBI database to obtain the mRNA sequence. To minimize unwanted secondary structures, regions with low self-hybridization were identified with RNAfold, and specificity was checked using BLAST to confirm uniqueness to *ABL1* *.

An additional DNA linker was appended to enable immobilization on nanowire surfaces. The chosen MB sequence is:

*The selection and design of the MBs were performed by Roberto Munita at the Division of molecular hematology, Lund University, and Diogo Volpati at the Division of Solid State Physics, Lund University

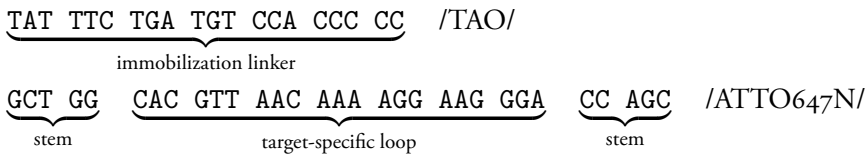

where *TAO* is the quencher, the loop sequence targets *ABL1* mRNA, and *ATTO647N* is the fluorophore.

In this particular case, we explore the detection limit of target complementary to the loop sequence. For evaluating specificity, we use the same target sequence with scrambled order as a negative control:

- Complementary target: `TCC CTT CCT TTT GTT AAC GTG`
- Scrambled (negative control): `AGT TCT CTC ATC GTT CCT TGT`

Prior to experiments, nanowires were passivated with PLL-g-PEG to reduce nonspecific binding. Immobilization involved layer-by-layer assembly of biotinylated PLL-g-PEG, streptavidin, DNA tethers complementary to the linker, and then the MBs themselves. All layers and target oligonucleotides were introduced under controlled flow with incubation and rinsing steps.

This qualitative design approach provides a basis for understanding molecular beacon behavior on nanowire biosensors, with full experimental optimization suggested for future work.

4.2.3 Supported lipid bilayers as model biological membranes

Biological membranes are essential structural components of all living cells. They define cellular boundaries, create compartments within the cell, and regulate the exchange of materials and signals with the surrounding environment. [121] The primary structural element of biological membranes is the lipid bilayer, a thin, flexible sheet composed of two layers of lipid molecules, primarily, phospholipids. These are amphiphatic molecules which have hydrophillic heads and hydrophobic tails. In aqueous environments, the phospholipids arrange in a double layer, with hydrophillic heads facing the aqueous environment and hydrophilic tails facing each other, forming a hydrophobic core. This arrangement creates a semi-permeable barrier that regulates the passage of substances and molecules in and out of the membrane. [122] The lipid bilayer is not a static barrier; instead, it behaves as a two-dimensional fluid in which lipids and many membrane-associated proteins can

undergo lateral diffusion within the plane of the membrane. [122] This lateral fluidity enables dynamic reorganization, membrane remodeling, and the diffusion-driven movement of components essential for cellular functions such as signaling, transport, and trafficking. [123, 124] Thus, the fluid nature of lipid bilayers can serve as model system to study membrane-associated processes and motions in a controlled manner.

Understanding the formation and properties of lipid bilayers is crucial for studying various biological processes, such as membrane protein function, cell signaling, and drug delivery. [125, 126]As the complexity and dynamic nature of native biological membranes pose a significant experimental challenge, model systems are used to investigate the fundamental properties of lipid bilayers in a controlled manner. Supported lipid bilayer (SLB), first created by Tamm and McConnell [127] in 1985, are widely used model formed by the spontaneous assembly of lipid molecules on solid supports, such as glass, quartz or silica.

4.2.3.1 SLB formation and curvature effects

SLBs are commonly formed by the fusion of lipid vesicles, small spherical structures composed of lipid bilayers enclosing an aqueous core. When vesicles contact a suitable substrate, they adsorb, rupture, and spread to form a continuous bilayer. [128, 129]

Spontaneous formation of SLBs through adsorption and rupture of small unilamellar vesicles on hydrophilic substrates constitutes the predominant method for generating planar cell membrane mimetics. [129] An alternative approach employs the Langmuir-Blodgett (LB) technique [130, 131], entailing vertical transfer of a proximal lipid monolayer from the air-water interface onto the substrate, followed by horizontal deposition of the leaflet. [132] Relative to this method, vesicle fusion affords greater simplicity and compatibility with transmembrane proteins, albeit with reduced asymmetry control.

The mechanism of vesicle-fusion-induced SLB formation on hydrophilic substrates can be described as follows: initially, vesicles adsorb and deform on the surface under adhesion forces but tend to remain intact for long periods. Increasing surface coverage leads to lateral vesicle-vesicle interactions that trigger rupture and fusion and formation of bilayer patches. These patches grow by merging with additional vesicles or other patches via energetically driven interactions at the exposed hydrophobic bilayer edges. Eventually, patches coalesce into a complete SLB, while excess vesicles that fail to fuse remain in solution. Factors such as vesicle charge, ionic strength, temperature, and surface properties like curvature and roughness modulate the fusion efficiency and bilayer quality. [129, 133]

While the majority of SLB studies have focused on planar surfaces, membrane curvature is seen as a mean of creating membrane domains and organizing centers for membrane trafficking. [134, 135] During cytokinesis, infection, cellular motion, or immune response,

the membranes undergo significant curvature changes. [136] SLBs on curved substrates thus provide a model system to study curvature-dependent biological processes, or natively curved biological structures, such as filopodia [137] or cilia [138].

Membrane curvature can be defined through the packing parameter P, which relates the intrinsic curvature of a lipid molecule to its geometric properties: the molecular volume V, the cross-sectional area of the head group a, and the length of the lipid tail l. The packing parameter is defined as

$$P = \frac{V}{a \cdot l} \tag{4.4}$$

Lipids with positive packing parameters tend to favor arrangements in concave membrane regions, whereas lipids with negative packing parameters are more stable in convex membrane areas.

4.2.3.2 SLBs on Nanowire Surfaces

The curvature-dependent kinetics of SLB formation via vesicle fusion can be studied on various nanostructured surfaces, including nanowires. In this thesis, vertically aligned Si NWs on a Si wafer with a 10 nm silica coating were employed to perform a comparative study of SLB formation on curved versus planar surfaces. NWs, designed to support lightguiding at wavelengths matching the fluorescence emission of Cyanine 5 (Cy5) around 670 nm, were compared against conventional glass slides as planar silica controls.

To enable fluorescent visualization of vesicle adsorption and SLB formation, a small fraction (∼1%) of POPC (1-palmitoyl-2-oleoyl-glycero-3-phosphocholine) lipid vesicles, with mean diameter 118 ± 4 nm and polydispersity index 0.33, were labeled with 1% Cy5-DOPE (1,2-dioleoyl-sn-glycero-3-phosphoethanolamine-N-Cy5) lipids, hereafter termed fluorescent vesicles.

The ability to successfully form SLBs on nanowire surfaces not only provides a model system for studying membrane-associated processes on curved substrates but also opens up new possibilities for biosensing applications. Elongated nanostructures can be a model system to study biological processes with similar geometries, while also providing enhanced optical properties for sensitive detection.

On the other hand, SLBs serve as a functional interface for biosensing. The bilayer's inherent fluidity allows the lateral diffusion of embedded molecules, such as labeled probes, enabling the study of their dynamic motion on the nanowire surface. This mobility not only mimics physiological membrane environments but also allows the quantification of biosensing signals based on molecular diffusion characteristics and interactions.

4.3 Flow channels for model biological systems

Reproducing that controlled movement in the laboratory is key to performing precise biological experiments. In the context of this thesis, the experimental work can be divided into two main categories: static and dynamic.

In static experiments, nanowires are incubated in a solution containing the target biological molecules. Binding is allowed to occur under equilibrium conditions, after which the sample is washed and subsequently imaged. This approach is straightforward and suitable for end-point characterization, as well as for future integration in POC devices.

In dynamic experiments, by contrast, the sample is exposed to a continuous flow of solution. This enables real-time observation of binding events, accumulation processes, or other transient interactions as they occur. Such measurements require more elaborate flow control but provide richer kinetic information.

Two experimental setups are employed to support these approaches. For static experiments, we use commercially available IBIDI VI sticky slides, which feature an adhesive base and pre-defined microchannel geometry, allowing them to be mounted directly onto a glass coverslip. For dynamic experiments, we rely on custom-fabricated microfluidic devices produced via soft lithography using polydimethylsiloxane (PDMS). These devices provide precise control over channel dimensions and flow conditions, and are well suited for studies requiring continuous perfusion.†

4.3.1 Description of the devices

The devices used in this thesis were designed to enable controlled delivery of solutions to nanowire surfaces, ensuring laminar flow and reproducible experimental conditions. Nanowires are typically 2–3 µm long, but are grown on a comparatively thick GaP substrate of approximately 300 µm. This large mismatch between the nanowire length and substrate thickness has important consequences for fluid handling and analyte transport.

For static and parallel measurements, commercially available Ibidi VI sticky slides were employed. These chambers consist of pre-defined channels with a 0.4 mm height and allow six independent measurements to be performed simultaneously. While simple to use, the tall channel height and large volume (30 µL) relative to the small nanowire surface area can result in inefficient delivery of analytes to the nanowires. The thick GaP substrate protruding into the channel further disrupts laminar flow, limiting mixing and diffusion, and increasing the potential for nonspecific interactions with channel walls. As a result,

†These devices were designed and prepared by Julia Valderas-Gutiérrez at the Division of Solid State Physics, Lund University. I performed COMSOL simulations to compare the fluid flow in both channels.

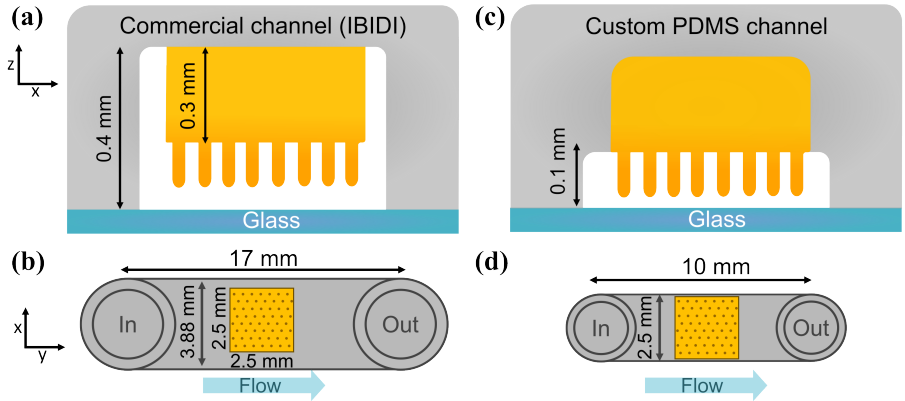

Figure 4.3: (a) and (b) show zx and xy cross-sections of a commercial microscopy channel, with nanowires attached to the top of the channel. (c) and (d) show the respective cross-sections in the custom-made channel. As it can be observed, the dimensions of the custom channel are more compact, ensuring laminar flow.

only a small fraction of the introduced sample reaches the nanowire surface, and controlled, pressure-driven flow cannot be applied (see Fig 4.3 a-b). This approach works relatively well for static incubation experiments, but is less suited for dynamic flow studies. In case of etched Si nanowires, the substrate thickness is larger than the channel height, making it impossible to use these commercial channels.

To overcome these limitations, a custom microfluidic device was developed in which a PDMS channel is integrated with the nanowire platform. In this design, the GaP or Si substrate is fully incorporated inside the PDMS, removing it as an obstacle to the flow. The channel dimensions can be tailored to the nanowire array, allowing compact, well-defined channels that support laminar flow. The PDMS can be independently surface-treated, preserving the nanowire surface chemistry while enabling robust and reproducible experiments (see Fig 4.3 c-d). This configuration improves analyte delivery, reduces dead volume, and provides a more controlled environment for studies.

The custom channel length and width are up to small variations. Papers II and IV provide detailed schematics and dimensions, as well as fabrication protocols.

4.3.2 Simulations of the fluid flow

To compare the fluid flow in both channels, COMSOL Microfluidics Module was used to simulate laminar single-phase flow in regimes where analytical solutions of the Navier–Stokes equations are impractical. To resolve the full three-dimensional flow behavior, we constructed and analyzed a 3D numerical model.

The stationary Navier–Stokes equations solved are

$$\rho(\mathbf{u}\cdot\nabla)\mathbf{u} = \nabla[-p\mathbf{I} + \mathbf{K} + \mathbf{F}], \qquad \nabla\cdot\mathbf{u} = 0,$$

$$\mathbf{K} = \mu\big(\nabla\mathbf{u} + (\nabla\mathbf{u})^T\big),$$

where $\nabla\mathbf{u}$ is the velocity gradient, p the pressure, $\mathbf{I}$ the identity tensor, $\mathbf{K}$ the rate-of-strain tensor, and $\mathbf{F}$ the body-force vector.

As it is expected, on xy planes, which are closer to the walls of the channel ($z = 10$ µm, $z = 390$ µm), the flow is negligible due to the parabolic nature of the flow. However, as the size of the channel and the nanowire platform have the same dimensionality, the placement of the platform distorts the flow drastically. As it can be observed from the slices $z = 100$ µm, 200 µm, 300 µm, the flow around the platform is distorted with high velocity distribution around the platform leading to poor analyte delivery to nanowires, thus decreasing the binding efficiency and the limit of the detection (see Fig 4.4).

To demonstrate the non-uniformity of the flow within the channel, we have simulated nanowire top plane ($z = 300$ µm). It can be observed from Figure 4.4 that the flow is relatively uniform further away from the platform, while closer to the platform, more is the difference in velocity between the edges and the center of the channel.

The fluid flow was also simulated in an ideal case of a fluid flow in a $10 \times 2.5 \times 0.1$ mm^3 channel (Figure 4.5), which reflects the parameters of custom-made PDMS channels. These simulations confirm our hypothesis that less platform is exposed to the channel, less flow distortions are created, thus a more uniform and controlled analyte delivery can be reached. As expected, in this case, all yz slices have the same velocity flow profile (Figure 4.5 b) due to channel symmetry. The flow velocity from inlet to outlet (xy plane, Figure 4.5) also behaves as expected and confirms the assumption that decreasing the channel height and the exposed platform, we can achieve more laminar and controlled flow.

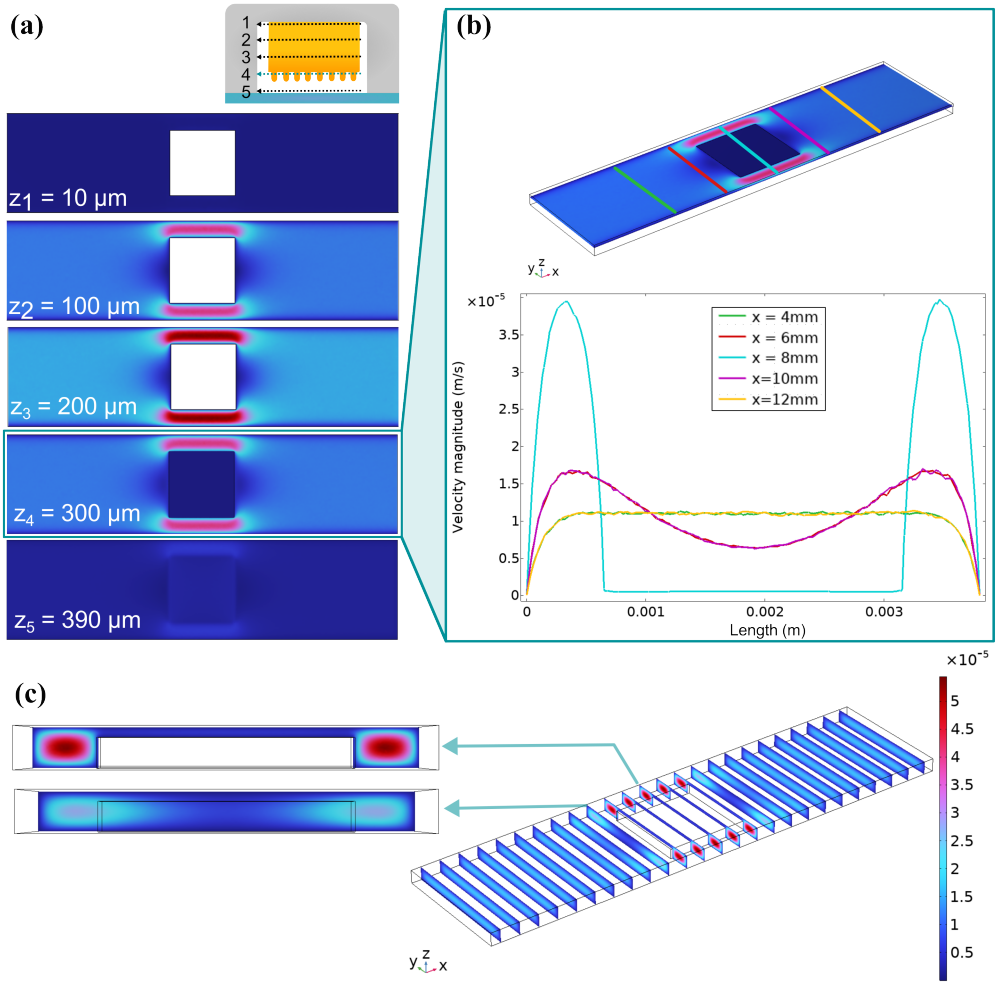

Figure 4.4: (a)Five xy planes at height of 10, 100, 200, 300 and 390 μm demonstrating how the flow behavior changes around the nanowire platform and the analyte delivery to the platform surface can be relatively poor due to this factor. The nanowire platform of size $2.5 \times 2.5 \times 0.3$ mm^3 (b) Velocity profile along the centerline of the channel at different heights. The flow is significantly disrupted by the nanowire platform, leading to recirculation zones and reduced analyte delivery to the nanowire surface. (c) yz slides of flow in the larger channel, where two planes (i) the flow right before reaching the platform and (ii) the flow on the platform are zoomed. It also can be observed from the yz planes of the channel that when the flow approaches the platform, the liquid swirls around the corners with poor coverage on the nanowire surface, especially in the middle of the platform.

While for both simulations the same driving pressure difference is applied, the flow velocity values do not reflect actual experimental conditions, as the fluid reservoir and tubing dimensions are not included in the model. However, the simulations provide a qualitative comparison of the flow behavior in both channels.

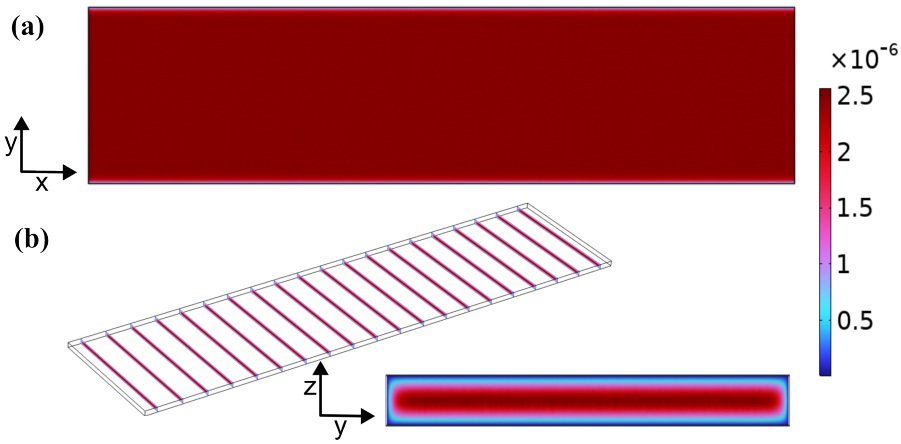

Figure 4.5: A simulation of laminar flow in a $10 \times 2.5 \times 0.1\ mm^3$ channel, where (a) represents the laminar flow in xy ($10 \times 2.5\ mm^2$) plane and (b) shows multiple yz ($2.5 \times 0.1\ mm^2$) slices. In this case, as no platform is placed in the channel, the flow is not distorted, thus the uniform flow profile is achieved.

4.4 Optically non-transparent media

Optical biosensors frequently rely on fluorescence, absorbance, or interferometric contrast that is generated by biomolecular recognition events. [139] Although laboratory validation is typically performed in optically transparent aqueous buffers, real-world applications require sensor operation in complex native biological fluids. In such media, including blood, plasma, saliva, milk, and food emulsions, light propagation is dominated by multiple scattering and wavelength-dependent absorption. As a result, simple attenuation models such as the Beer–Lambert law (see Equation 4.5) are insufficient to describe light transport [140]. This limitation arises because most biological fluids contain micron-scale scatterers, including red blood cells, fat globules, and protein aggregates, which produce strong Mie scattering and lead to non-exponential attenuation of optical signals.

In weakly scattering media, the attenuation of light can be described by Beer-Lambert law:

$$I = I_0 e^{-\epsilon c l} \tag{4.5}$$

where I is the transmitted light intensity, I_0 is the incident light intensity, ϵ is the molar extinction coefficient, c is the concentration of the absorbing species, and l is the path length through the medium. Here, ϵ represents an effective extinction coefficient that, in simple absorbing solutions, reflects true absorption but can be generalized to include scattering contributions when only total attenuation is measured.

Oftentimes, instead of molar extinction coefficient, absorption coefficient μ_a and scattering coefficient μ_s are used, which are expressed in mm^{-1}. The overall effect of scattering and

absorption can be given as the total attenuation coefficient μ_t', defined as:

$$\mu_t' = \mu_a + \mu_s' \tag{4.6}$$

where $\mu_s' = \mu_s(1-g)$ is the reduced scattering coefficient, accounting for the anisotropy factor g. For a single scattering event, the characteristic penetration depth, or mean free path, is given by $l_p = 1/\mu_t'$. [141, 142] Turbid biological media, on its turn, can be characterized as $\mu_t' l_p \gg 1$. In this case, Beer–Lambert law either needs to be modified to include multiple scattering effects [143, 144] or replaced with more comprehensive models of light transport, such as radiative transfer theory or diffusion approximations.

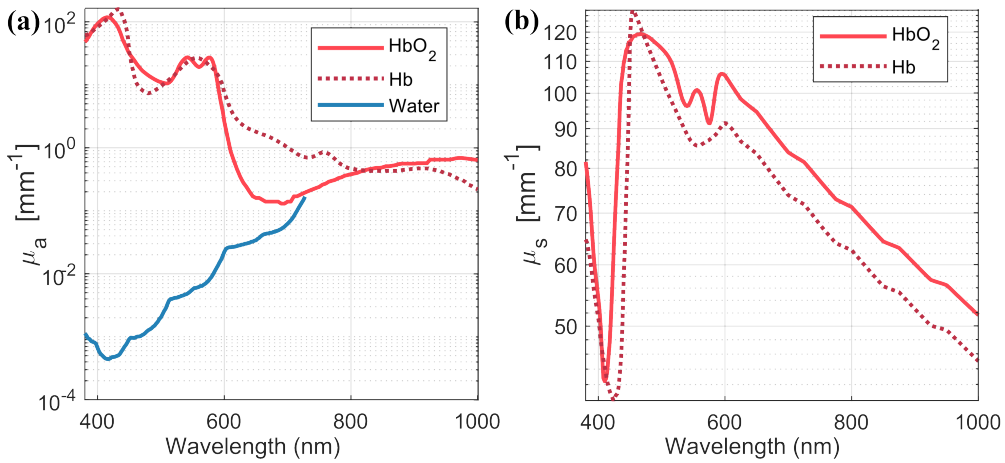

Figure 4.6: Optical properties of whole blood and water. (a) Absorption coefficient μ_a for oxygenated (HbO_2) and deoxigenated blood(Hb), as well as pure water. (b) Theoretically compiled scattering coefficent (μ_s) for oxygenated and deoxygenated blood. The data for water is originally from [145], compiled in OMLC database [146]. The blood data is compiled from [147], and Kramers-Kronig/Percus-Yevick theory values for μ_s are plotted.

Detailed theoretical and experimental investigations of light propagation in complex biological fluids are well established in the literature [140, 142] and beyond the scope of this thesis. However, we rely on these principles to explore the use of lightguiding nanowires for biosensing in optically non-transparent media.

In whole blood, optical attenuation exhibits hemoglobin absorption peaks in the Soret band (400–450 nm) and Q-bands (500–600 nm), with contributions from oxygenation state, plasma proteins, and water absorption beyond 1100 nm [147, 148] (see Figure 4.6 a). Scattering is predominantly dominated by red blood cell (RBC) scattering, with additional contributions from plasma proteins and water beyond 1100 nm [147](see Figure 4.6 a). Scattering from RBCs exhibits strong forward bias ($g \approx 0.98$–0.99). In milk and related food emulsions, fat globules (1–10 µm) and casein micelles (50–300 nm) are the primary scatterers, while chromophores such as carotenoids and riboflavin contribute to wavelength-dependent absorption. [149, 150]

Chapter 5

Machine: Computational modeling, simulation and image analysis

"Throughout human history, we have been dependent on machines to survive. Fate, it seems, is not without a sense of irony."

Morpheus, The Matrix

In contemporary research, the dependence on computational tools is more pronounced than ever. This thesis is no exception: it relies extensively on computational methods to model, simulate, and analyze the interaction of light with nanowires and the resulting optical images.
This chapter describes the computational methods used throughout this work, including (i) modeling the light-matter interactions of nanowires and fluorophores, (ii) simulating the image formation process and generating synthetic images, and (iii) developing and applying conventional and deep-learning based image analysis algorithms to extract meaningful information from microscopy data.
In doing so, this chapter, and the thesis more broadly, highlights the critical role of computational tools to bridge experiments and theory, enabling to push the limits of optical detection.

5.1 Modeling of nanowires as optical sensors

Nanowire-based sensors, being a promising candidate for biosensing, still rely on a variety of design parameters that need to be optimized for the best performance. As described in chapter 3.1.1, nanowires enhance the fluorescence signal through a combination of excitation enhancement, emission modification, and directional emission. The growth and fabrication of nanowires with specific dimensions and material properties can be challenging, time and resource consuming. Therefore, computational modeling of nanowires in context of biosensing, namely fluorescence detection, is essential to guide parameter choice, experimental design, and in this case, optical image formation. Various computational modeling studies alongside with experimental works have been done to understand the effects of nanowire diameter [20], material properties and refractive index, oxide thickness [27]. A recent study by N.Anttu [67] covered the final gap of extending the modeling to image formation, providing a framework to understand and simulate nanowire-based fluorescence detection.

Section 3.1.1 provides a brief overview of nanowire-based signal enhancement mechanisms, describing the main aspect affecting signal enhancement. This section provides a more detailed description of the computational modeling aspect, focusing on each individual enhancement mechanism. It includes excitation enhancement, emission modification, and collection enhancement. As described in Ref. [67], a distinction between signal-integration and imaging modes can be made. In signal-integration mode, the total collected power from nanowire-fluorophore system is considered, while in imaging mode, image formation through a microscope objective is modeled. Thus, instead of collection enhancement in signal-integration mode, image formation model will be described. Subsequently, the formed image indirectly includes the collection enhancement effect. Note, that due to the fact that the same microscope objective is used for both excitation and collection of light, there is no distinction between collection and excitation numerical apertures.

Generally speaking, fluorophores can effectively be modeled as electric dipoles. Assuming time-harmonic electromagnetic fields with time dependence $e^{-i\omega t}$, where $\omega = \frac{2\pi c}{\lambda}$, with c the speed of light in vacuum and λ the vacuum wavelength, the complex electric $\mathbf{E}$ and magnetic $\mathbf{H}$ fields are calculated by solving Maxwell's equations by finite element method (FEM) method in COMSOL Multiphysics.*

*The modeling is based on numerical solutions of Maxwell's equations performed in COMSOL Multiphysics, developed and provided by N. Anttu. I modified the relevant parameters to be comparable with nanowires and conditions used in experiments.

5.1.1 Excitation enhancement

Excitation enhancement refers to the increase of local excitation intensity at the fluorophore location compared to the excitation intensity of a free fluorophore in homogenous medium. The main assumption is that the excitation probability is porportional to the squared electric field $|\mathbf{E}(r,z)|^2$, where r and z are the radial and axial coordinates, respectively. In the context of widefield illumination, the incident light is modelled as incoherent plane waves, described by polar angle θ_{inc} and azimuthal angle ϕ_{inc}. Scattered field formulation is used:

$$\mathbf{E}(\mathbf{r},\lambda_{\text{ex}},\theta_{\text{inc}},\phi,\hat{\mathbf{e}}) = \mathbf{E}_{\text{bg}}(\mathbf{r},\lambda_{\text{ex}},\theta_{\text{inc}},\phi_{\text{inc}},\hat{\mathbf{e}}) + \mathbf{E}_{\text{sc}}(\mathbf{r},\lambda_{\text{ex}},\theta_{\text{inc}},\phi_{\text{inc}},\hat{\mathbf{e}}). \tag{5.1}$$

Here, $\hat{\mathbf{e}}$ denotes the polarization vector, where s (Transverse Electric) and p (Transverse Magnetic) polarizations are chosen. Incident light with s polarization has its electric field oriented perpendicular to the incidence plane, while p polarization is oriented parallel. The background field $\mathbf{E}_{\text{bg}}$ is the field in the absence of the nanowire and can be analytically expressed. $\mathbf{E}_{\text{sc}}$ is the scattered field due to the presence of the nanowire. This is modelled numerically by solving Maxwell's equations for diffraction of light as described in Refs. [27, 67, 151].

The intensity of electric field at the location $\mathbf{r}$ is given by:

$$|\mathbf{E}(\mathbf{r},\lambda_{\text{ex}})|^2 = \frac{\displaystyle\sum_{\hat{\mathbf{e}}=s,p}\int_0^{2\pi}\int_0^{\theta_{\text{NA}}} |\mathbf{E}(\mathbf{r},\lambda_{\text{ex}},\theta_{\text{inc}},\phi_{\text{inc}},\hat{\mathbf{e}})|^2 \,\sin\theta_{\text{inc}}\, d\theta_{\text{inc}}\, d\phi_{\text{inc}}}{\displaystyle\sum_{\hat{\mathbf{e}}=s,p}\int_0^{2\pi}\int_0^{\theta_{\text{NA}}} \sin\theta_{\text{inc}}\, d\theta_{\text{inc}}\, d\phi_{\text{inc}}}. \tag{5.2}$$

Due to the circular symmetry of the nanowire, a simulation for a given ϕ_{inc} provides all information for the averaged field around the nanowire circumference at radius r for all incidence angles ϕ_{inc}. Consequently, one only has to vary θ_{inc} and polarization in the simulations. Finally, the excitation enhancement factor for wavelength λ_{ex} at position z on nanowire axis is calculated as:

$$\eta_{\text{ex}}(r,z) = \frac{\displaystyle\int_0^{\theta_{\text{NA}}} \left(|E_s(r,z,\theta_{\text{inc}},\lambda_{\text{ex}})|^2 + |E_p(r,z,\theta_{\text{inc}},\lambda_{\text{ex}})|^2\right)\sin\theta_{\text{inc}}\, d\theta_{\text{inc}}}{2\displaystyle\int_0^{\theta_{\text{NA}}} \sin\theta_{\text{inc}}\, d\theta_{\text{inc}}\, |E_{\text{inc}}|^2}. \tag{5.3}$$

Here, the incident electric field intensity $|E_{\text{inc}}|^2$ is in units of $1\,[\text{V/m}]^2$, and the calculated local electric field intensities $|E_s|^2$ and $|E_p|^2$ have the same units. Thus, the excitation enhancement factor $\eta_{\text{ex}}(r,z)$ is a dimensionless number describing the local field amplification due to the nanowire at the fluorophore location.

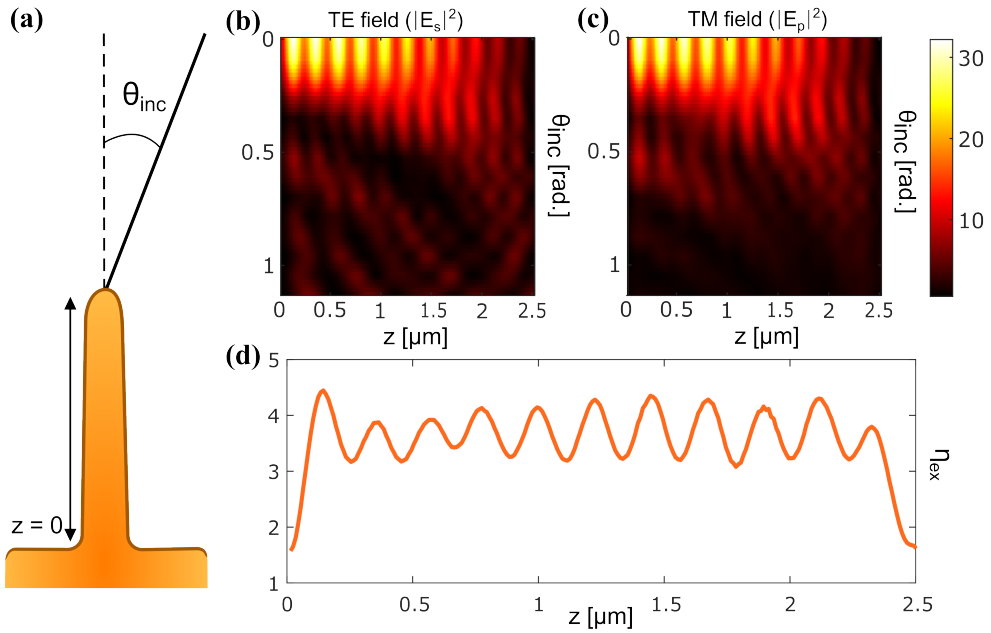

Figure 5.1: Schematic of excitation enhancement calculation for $\mathrm{NA} = 1.2$. (a) An illustration of nanowire, demonstrating the incident angle θ_{inc}. (b-c) Are *s* and *p* polarized squared electric fields in relation to incident angle θ_{inc} and nanowire z position. (d) The final excitation enhancement (η_{ex}) is calculated by integrating over incident angles and polarizations and is dependent on z-position.

5.1.2 Modification of emission by nanowires

As described before, the emission modification can take radiative and non-radiative forms. An assumption, reflecting realistic fluorophores, is made, such as that when the fluorophore is in the vicinity of nanowire, the non-radiative pathway stays unaffected. As of radiative transfer modification, Purcell factor is used for quantification. Purcell factor is independent of excitation conditions and optics, and can be obtained by comparing the emitted power from the dipole in the presence of the nanowire to that of a free flurophore. In simulated system, the emitted power P_{em} from a dipole fluorophore is modeled by integrating the Poynting vector $\mathbf{S}$ over a closed surface S surrounding the emitter:

$$P_{em} = \oint_S \mathbf{n} \cdot \mathbf{S}\, dS \tag{5.4}$$

where $\mathbf{n}$ is the surface normal. If the nanowire can absorb fluorescence (i.e., if $Im(n) > 0$ for the nanowire material at the fluorescence wavelength), this surface must be chosen such that the enclosed volume contains no absorbing material.

This emitted power is evaluated separately for dipole orientations along x, y, and z, assum-

ing a random emission dipole orientation:

$$P_{\text{em,avg}} = \frac{1}{3} \sum_{i \in \{x,y,z\}} P_{\text{em},i} \tag{5.5}$$

To quantify enhancement, $P_{\text{em,avg}}$ is compared to the analytically known emission power of a dipole in a reference homogeneous medium [152]:

$$P_{\text{em,analytical}} = \frac{2n\omega^2 p_{\text{dipole}}^2}{12\pi\epsilon_0 c^3} \tag{5.6}$$

with refractive index n, angular frequency ω, dipole moment magnitude p_{dipole}, vacuum permittivity ϵ_0, and speed of light c.

The Purcell factor C_{Purcell}, indicating the modification of radiative emission rate by the nanostructure, can be then calculated as:

$$C_{\text{Purcell}} = \frac{P_{\text{em,avg}}}{P_{\text{em,analytical}}} \tag{5.7}$$

For a fluorophore with a reference QY Φ_0^f, the enhancement through quantum yield modification will be [67]:

$$\eta_{QY} = \frac{C_{\text{Purcell}}}{C_{\text{Purcell}}\Phi_0^f + (1 - \Phi_0^f)} \tag{5.8}$$

5.2 Image formation and synthetic data

Excitation enhancement (η_{ex}) and QY (η_{QY}) modification enhancement provide a measure of signal enhancement at the fluorophore location. However, to fully understand the molecular detection process, it is essential to model the image formation through the microscope system. In this case, not only the fluorophore position on the nanowire matters, but also the axial position of focal plane of the microscope objective. Image formation is a far-field process, thus we first calculate the far-field emission from the dipole-nanowire system, and then model the image formation through FFT-based methods.

The image is calculated for each binding position of the fluorophore on the nanowire, and for different focal plane positions. This theoretical image then needs to be binned to match the camera pixel size, and corrected for excitation enhancement and Purcell factor, to provide a realistic estimate of the detected signal intensity from a fluorophore at a given position on the nanowire.

5.2.1 Image formation model

The simulations for the imaging-mode detection are based on the same dipole model employed for calculating Purcell factor. The RETOP package [153] is used to perform a near-field-to-far-field transformation (NFFT), which is capable of handling the presence of a substrate. The far-field emission entering the collection objective is assumed to be focused onto the image plane. The far-field emission direction is described in Fourier space coordinates (k_x, k_y), where

$$k_x = \sin(\theta)\cos(\phi)k_0, \quad k_y = \sin(\theta)\sin(\phi)k_0, \tag{5.9}$$

with θ and ϕ denoting the polar and azimuthal angles, respectively, and

$$k_0 = \frac{2\pi}{\lambda} \tag{5.10}$$

the free-space wavenumber. The RETOP package provides the electric field components $\mathbf{E}_{\text{farfield}}(k_x, k_y)$ and the wavevector component along the optical axis (assumed z-axis), $k_{\text{farfield}}(k_x, k_y)$, at a reference plane $z = z_{\text{ref}}$.

To account for the focal plane z_{focal}, each far-field component is multiplied by a phase factor

$$\exp\left[ik_{\text{farfield}}(k_x, k_y)(z_{\text{ref}} - z_{\text{focal}})\right]. \tag{5.11}$$

This operation is performed on a grid of evenly spaced k_x and k_y values, enabling the use of FFT for efficient image formation. A cut-off is applied such that directional components with $\sqrt{k_x^2 + k_y^2} > \text{NA}k_0$ set to zero, reflecting the limited collection angle of the microscope objective.

The phase-shifted, truncated far-field components are then compiled into large matrices $E_x^{\text{FFT}}, E_y^{\text{FFT}}, E_z^{\text{FFT}}$ corresponding to the spatial Fourier representation of the electric field, padded appropriately in the matrix center to align with the FFT conventions. The components from RETOP, are corrected by division by $\cos(\theta)$ (the Debye-Wolf correction [154]) and multiplied by the phase factor implementing the focal shift:

$$E_x^{\text{FFT}}(k_x, k_y) = \frac{\text{EH}_x(k_x, k_y)}{\cos(\theta)} \exp\left[-ik_z(z_{\text{focal}} - z_{\text{ref}})\right]|_{\theta<\theta_{\text{NA}}}, \tag{5.12}$$

with analogous expressions for E_y^{FFT} and E_z^{FFT}, where the indicator function restricts to angles within the objective NA: $\theta_{\text{NA}} = \arcsin\left(\frac{\text{NA}}{n_{\text{ambient}}}\right)$.

The final electric field components, $E_x(x, y), E_y(x, y), E_z(x, y)$ on the image plane are obtained by inverse fast Fourier transform of the padded matrices. The image, representing the spatial signal intensity in the image plane., is computed as:

$$I^i_{\text{img}}(x, y) = |E_x(x, y)|^2 + |E_y(x, y)|^2 + |E_z(x, y)|^2, \tag{5.13}$$

Here, the index i denotes the dipole orientation (x, y, or z). The total image intensity is then averaged over all three dipole orientations:

$$I_{\text{img}}(x, y) = \frac{1}{3} \sum_{i=1}^{3} I^i_{\text{img}}(x, y). \tag{5.14}$$

The image intensity $I_{\text{img}}(x, y)$ is needs to be normalized, and for normalization we use the following relation [67]:

$$\bar{I}_{\text{img}}(x, y) = \frac{I_{\text{img}}(x, y)}{C_{\text{Purcell}} P_{\text{em,analytical}}} \tag{5.15}$$

We will also refer to $\bar{I}_{\text{img}}(x, y)$ as the PSF of the nanowire-fluorophore system, as it describes the spatial intensity distribution in the image plane for a fluorophore at a specific position on the nanowire.

5.2.2 Microscope image creation

The theoretical image formation model provides the PSF of the nanowire-fluorophore system for different fluorophore binding positions on the nanowire and different focal plane positions. To create a realistic synthetic image, several additional factors need to be considered, including excitation enhancement, quantum yield modification, microscope camera characteristics, and imaging noise. The overall image creation process is illustrated in Figure 5.2†.

The simulated images were used to benchmark different image analysis algorithms in Paper III, as well as to train a regression-based convolutional neural network (CNN) and to generate simulations of molecular diffusion in Paper V. We approximate the microscope camera as an ideal photon detector, where each photon contributes equally to the detected signal. Due to the radial symmetry of the nanowire, we only simulated the PSF for fluorophores bound along a single radial line on the nanowire surface, as this captures all unique binding positions. If necessary, different angular positions can be reconstructed by rotating the PSF accordingly.

To simulate the image formation process, we first create a grid representing the nanowire locations in the field of view, using the known nanowire array parameters, such as nanowire length, pitch, diameter, and the percentage of kinked nanowires. To simulate different concentrations of molecules, we initialize a certain number fluorophores, which can bind either to straight nanowires, kinked nanowires, or the substrate between nanowires. Kinked

†I wrote the codes and performed all simulations from this point onwards

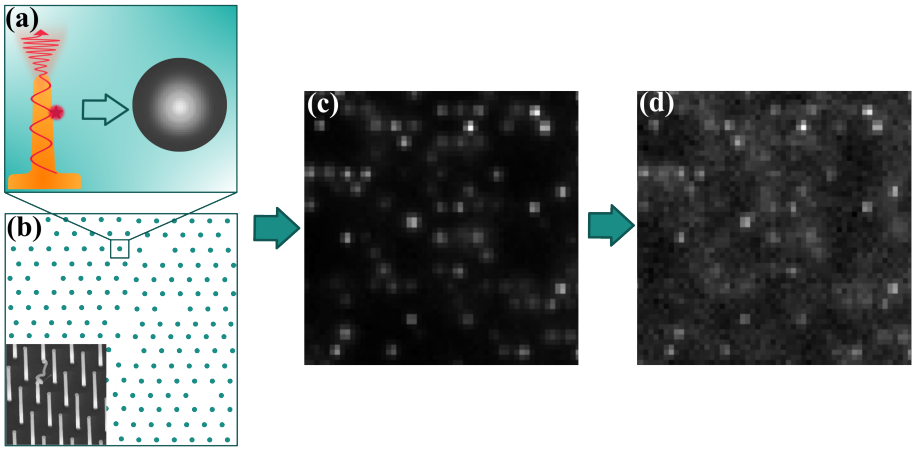

Figure 5.2: Theory-based image generation. **(a)** PSF estimation based on the binding position of a fluorophore on nanowire (b) A grid with nanowire locations - a fluorophore can bind on nanowires or a substrate, which is the space between nanowires (c) A generated image corresponding only to emisson from nanowires (d) The final image, where the signal emitted from the substrate and noise are added.

nanowires are considered to have similar properties as substrate, hence no enhancement is assumed. Area-based random sampling is used to assign binding locations of fluorophores. For each fluorophore bound to a straight nanowire, we randomly assign a binding position along the nanowire height. Using the pre-calculated PSF for the corresponding binding position and focal plane position, we generate the image contribution from each fluorophore, using the pre-calculated excitation and quantum yield enhancement factors. The total detected photon count from a fluorophore at position (z) on the nanowire is given by:

$$N_{\text{photon}}^{\text{eff}} \sim \text{Poisson}\left(\Phi \cdot \eta_{\text{QY}}(z) \cdot \eta_{\text{ex}}(z) \cdot J_{\text{norm}}(z) \cdot N_{\text{photon}}\right) \tag{5.16}$$

where $N_{\text{photon}}^{\text{eff}}$ is the effective number of photons detected from a bright nanowire, Φ is the quantum yield of the fluorophore in a homogeneous medium, and $J_{\text{norm}}(z)$ is normalized excitation laser intensity. Instead of laser power, we use the number of detected photons in the absence of nanowires proportional to the excitation time, N_{photon}. This allows us to directly control the SNR of the simulated images, and the values are selected according to experimental images. The detected photon count is sampled from a Poisson distribution to account for photon shot noise.

Afterward, $N_{\text{photon}}^{\text{eff}}$ photons were sampled from the numerical PSF using the generation of random numbers from discrete 2D functions [155]. The SNR of the images was varied by varying the excitation time, which translates into a varied number of detected photons per bright nanowire.

In the event of multiple binding, the photons were sampled from each position and added to form the final image. In case of fluorophore binding to GaP substrate instead of nanowires,

we used a z-dependant Gaussian PSF [31, 156]. This approximation was used in Paper III, however, later on, we replaced it with a modelled exact PSF for a dipole on a substrate.

Gaussian read noise $\mathcal{N}(0, \sigma^2_{\text{read}})$ and pixel response non-uniformity (PRNU) modeled as multiplicative noise around unity with variance σ^2_{PRNU} are added:

$$I_{\text{final}} = (I_{\text{NW}} + I_{\text{sub}}) \times \left(1 + \mathcal{N}(0, \sigma^2_{\text{PRNU}})\right) + \mathcal{N}(0, \sigma^2_{\text{read}}). \tag{5.17}$$

Here, I_{NW} and I_{sub} are the image contributions from fluorophores bound to nanowires and substrate, respectively. The read noise and PRNU values were selected to match the characteristics of the experimental camera used in the measurements. The photon coordinates are binned onto a pixel grid determined by image size and pixel dimensions, forming separate nanowire and substrate images.

5.3 Image Analysis Techniques

5.3.1 Traditional single-emitter localization

Traditional single-emitter localization refers to a family of algorithms that (i) identify bright spots that stand out from the background according to defined mathematical criteria, and (ii) estimate their coordinates within an image frame. [15, 30]. A wide range of approaches exists in the literature, [30, 34] each optimized for specific imaging conditions, computational constraints, or signal characteristics. However, due to their robustness, simplicity, and compatibility with nanowire-related data, we focus here on the methods most relevant to our analysis pipeline.

The detection process typically consists of four main steps, some of which are optional, described below

Step 1: Image Enhancement

Image enhancement improves signal quality and suppresses noise. It refers to techniques that remove imperfections from an image while highlighting key features [157, 158]. Enhancements can be performed either in the spatial or frequency domain (see Section 5.3.2). This is typically achieved by convolving the image with small matrices called *filters* or *kernels*, which modify the image through defined mathematical operations. [157, 159]

Typically, image enhancement can be performed in spatial domain, using linear and nonlinear filters. Linear filters (kernels), which are essential in signal and image processing, manipulate the data in both the frequency and spatial domains. [157, 160] In the spatial

domain, filters directly modify the pixel values, oftentimes through convolution between the filter and image:

$$f[n] = \sum_{k=0}^{M-1} h[k] \cdot g[n-k] \tag{5.18}$$

where $f[n]$ is the filtered image, $h[k]$ is the original image, $g[n-k]$ is the filter kernel, and M is the size of the kernel. [157] Common linear filters include Gaussian smoothing, which reduces high-frequency noise but can blur edges, and Sobel filters, which enhance edges by computing gradients. [158]

Non-linear filters, such as median filtering, are more effective at preserving edges while reducing noise. [157] One common non-linear approach is wavelet filtering, which decomposes the image into different frequency components, while preserving spatial information. [161, 162] Wavelet filtering, particularly cubic B-spline based undecimated wavelet transform (UWT), has been shown to effectively denoise microscopy images while preserving important features. [162] Alongside frequency domain methods, described in Section 5.3.2, wavelet filtering based on [162] for image enhancement is used in our analysis pipeline.

Step 2: Location Estimation

Location estimation involves detecting the brightest pixels within local neighborhoods, usually by thresholding. Since this step typically identifies only pixel-level coordinates, additional refinement is required for sub-pixel accuracy.

We implemented a thresholding approach based on local gradient estimation, leveraging the assumed symmetry of the nanowire signal. [163] Local maxima are detected by identifying the brightest pixels in each neighborhood using image dilation. [164]

Assuming central symmetry of each PSF, the local gradient G is computed for each detection [22, 163]:

$$G = \sum_{\text{box}} g_i \vec{u_i} \tag{5.19}$$

where g_i is the central difference gradient at the i-th pixel and $\vec{u_i}$ is the unit vector pointing toward the detection center. The only parameters adjusted in our analysis were the local gradient threshold (G_{min}) and the size of the user-defined box (see Figure 5.3 b).

Step 3: Position Refinement

Position refinement provides precise coordinates of each emitter. One of Position refinement provides precise coordinates of each emitter. A widely used method for this purpose

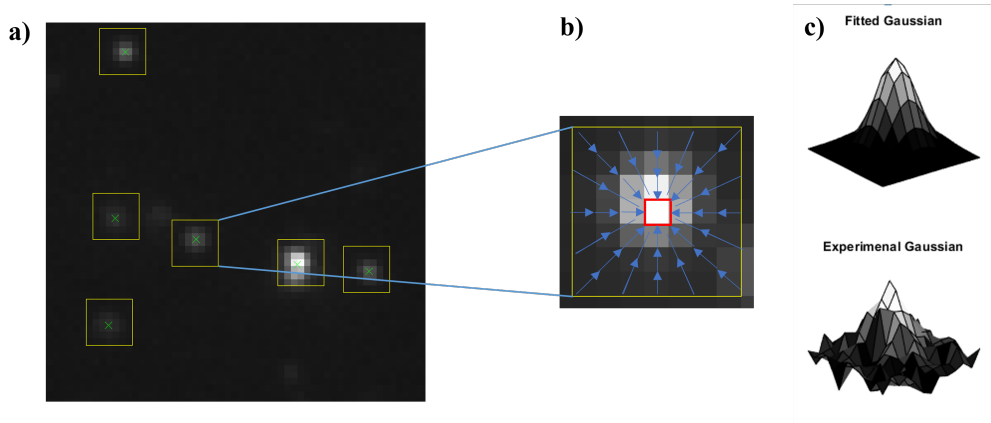

Figure 5.3: (a) A sample image with detected spots (yellow squares) and refined locations (green crosses). (b) Example of identifying the brightest pixel (red) with gradient vectors pointing toward it. (c) Comparison of a Gaussian PSF and a noisy Gaussian PSF, representative of experimental data.

is fitting a 2D Gaussian function to the detected signal (Figure 5.3 c) [165]. In this approach, the measured intensity around a candidate emitter is modeled as a Gaussian distribution, and the fit parameters, including the center position, amplitude, and width, are optimized to best match the observed data.

We incorporated a Gaussian-fitting procedure based on [32]. Even though the intensity profile of nanowires is not strictly Gaussian. Often, it shows showing asymmetry, and other deviations due to the underlying nanowire geometry. However, fitting a Gaussian remains a reliable way to locate the position of the intensity maximum. The fit effectively smooths over noise and small deviations, producing a robust estimate of the emitter center.

Alternative methods, such as weighted-centroid estimation or more complex shape-fitting algorithms, such as experimental PSF fitting, can be applied depending on the signal characteristics, but Gaussian fitting provides a practical and well-established baseline for obtaining precise emitter coordinates.

Step 4: Outlier Exclusion

Outlier exclusion is an optional but important step in single-emitter localization, aimed at removing false positives that may arise due to noise, background fluctuations, or spurious detections. In general, all types of detection methods can yield some false positives, and a variety of statistical and computational approaches have been developed to identify and remove them.

In our analysis, and subsequently the used software, we implemented two complemen-

tary strategies for outlier exclusion were developed. The first is a statistical and machine learning-based approach, where isolated points are identified as outliers using clustering methods: for example, DBSCAN can detect points that do not belong to coherent clusters of emitters [166], while k-means can group detections and highlight those falling outside expected clusters [167]. The second strategy relies on the known periodic structure of the nanowires. Here, we assume that true signals are colocalized with nanowires, while detections located between nanowires are likely false positives. By combining these two approaches, our pipeline effectively minimizes false positives while preserving true emitter detections. Section 5.3.3 provides more details on periodicity-based outlier exclusion.

5.3.2 Image manipulation in frequency domain

Frequency-domain analysis is a powerful tool in image processing because it allows separation of image components based on spatial frequencies. In microscopy, it can be used to isolate signals from the background created by illumination sources, such as lasers or lamps. Signals with distinct frequency characteristics can also be separated effectively.

In computational image processing, the discrete Fourier transform (DFT) is widely used for its efficiency and ease of implementation. The DFT is typically computed using the fast Fourier transform (FFT) algorithm, which reduces the computational complexity from $O(N^2)$ to $O(N \log N)$, where N is the data size. [161] This enables fast processing of large datasets, becoming especially advantageous in real-time image processing, including in microscopy applications.

For an image $g[x, y]$ of size $M \times N$, the DFT is defined as:

$$F[u, v] = \sum_{x=0}^{M-1} \sum_{y=0}^{N-1} g[x, y]\, e^{-j2\pi\left(\frac{ux}{M} + \frac{vy}{N}\right)} \tag{5.20}$$

where u and v are the discrete frequency indices. The magnitude $M[u, v]$ and phase $\phi[u, v]$ of the DFT are:

$$M[u, v] = |F[u, v]| = \sqrt{\mathrm{Re}(F[u, v])^2 + \mathrm{Im}(F[u, v])^2} \tag{5.21}$$

$$\phi[u, v] = \arctan\left(\frac{\mathrm{Im}(F[u, v])}{\mathrm{Re}(F[u, v])}\right) \tag{5.22}$$

where $\mathrm{Re}(F[u, v])$ and $\mathrm{Im}(F[u, v])$ denote the real and imaginary parts of $F[u, v]$. The magnitude represents the amplitude of each frequency component, while the phase encodes its spatial arrangement.

In the frequency domain, kernels such as low-pass and high-pass filters selectively allow or reject specific frequency ranges [161]. The convolution theorem states that the Fourier

transform of the convolution of two functions $h[x, y]$ and $g[x, y]$ is equal to the product of their Fourier transforms:

$$\mathcal{F}\{h * g\}[u, v] = \mathcal{F}\{h\}[u, v] \cdot \mathcal{F}\{g\}[u, v] = H[u, v]\, G[u, v] \tag{5.23}$$

where $H[u, v]$ and $G[u, v]$ are the DFTs of $h[x, y]$ and $g[x, y]$.

In other words, convolution in the spatial domain becomes **element-wise multiplication** (Hadamard product) in the frequency domain:

$$H \circ G = H[u, v] \cdot G[u, v] \tag{5.24}$$

This is different from standard matrix multiplication and requires both matrices to have the same dimensions.

5.3.2.1 High-pass and low-pass filters

Different components of images map to different frequencies in Fourier domain, e.g. edges, sharp intensity transitions contribute to high frequency content, while smoother, less variable features correspond to lower frequencies [161].
A 2D low-pass Gaussian filter of size $M \times N$ is defined as:

$$H_{LPG}(u, v) = e^{-D^2(u,v)/2D_0^2} \tag{5.25}$$

where D_0 is the cutoff frequency. $D(u, v)$ is a distance between the given point (u, v) and the frequency domain center of a $M \times N$ square [161]:

$$D(u, v) = [(u - M/2)^2 + (v - N/2)^2]^{0.5} \tag{5.26}$$

In microscopy images, especially when a laser or lamp was used for excitation or illumination, this pattern is residing in the low frequency part, as it can be seen in Fig. 5.5. Thus, for our images, the application of low-pass filters will result in image background component. As the signal emitted from nanowires corresponds to a higher frequency component, high-pass filters are more useful. The high-pass counterpart of low-pass Gaussian filter is simply defined as:

$$H_{HPG} = 1 - H_{LPG} \tag{5.27}$$

Figure 5.4 demonstrates that when a high-pass filter is applied, the resulting image has a more uniform background, as low-frequency components are cut out.

This filter or its equivalents in frequency or spatial domains suitable for removing image background are necessary when we are comparing detection intensities across specimen or different samples, as the contribution from background is not desired.

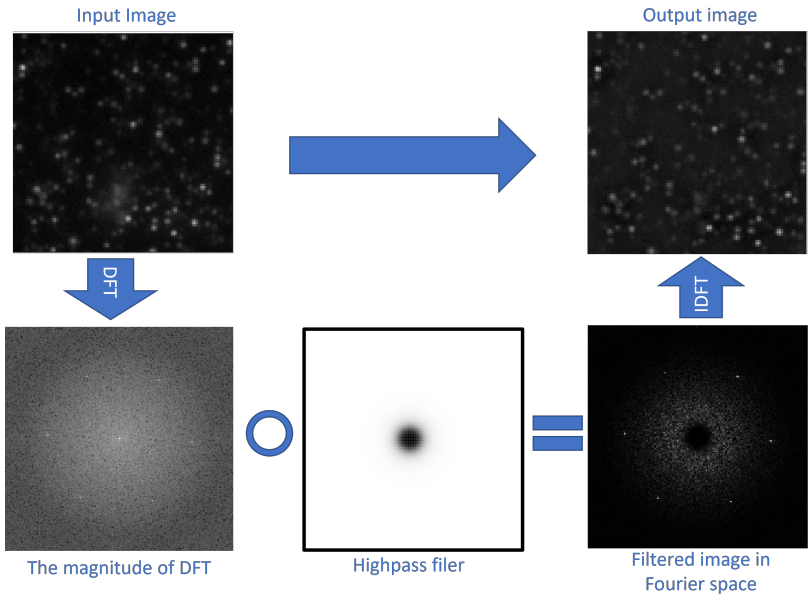

Figure 5.4: The concept of high-pass filtering in Fourier space. The resulting image is the denoised high-frequency component of the image.

5.3.2.2 Notch filters

When a specific frequency band or frequencies in a small region are needed, *band filters* or *Notch filters* can be used, respectively [161]. Due to the periodicity of nanowire placement, we are interested in Notch filters, which can be classified as notch-reject or notch-pass, depending on whether they reject or pass the specified frequencies.

Notch filters are zerophase-shift filters, meaning they exhibit symmetry in the center of the frequency rectangle. For a notch filter centered at u_0, v_0, a corresponding notch emerges at $(-u_0, -v_0)$. Notch reject filter transfer functions result from multiplying highpass filter transfer functions, where centers are adjusted to align with the notches [161]:

$$H_{NR}(u,v) = \prod_k H_k(u,v) \cdot H_{-k}(-u,-v) \tag{5.28}$$

Here, $H_k(u,v)$ and $H_{-k}(-u,-v)$ are highpass filter transfer functions centered at (u_k, v_k)

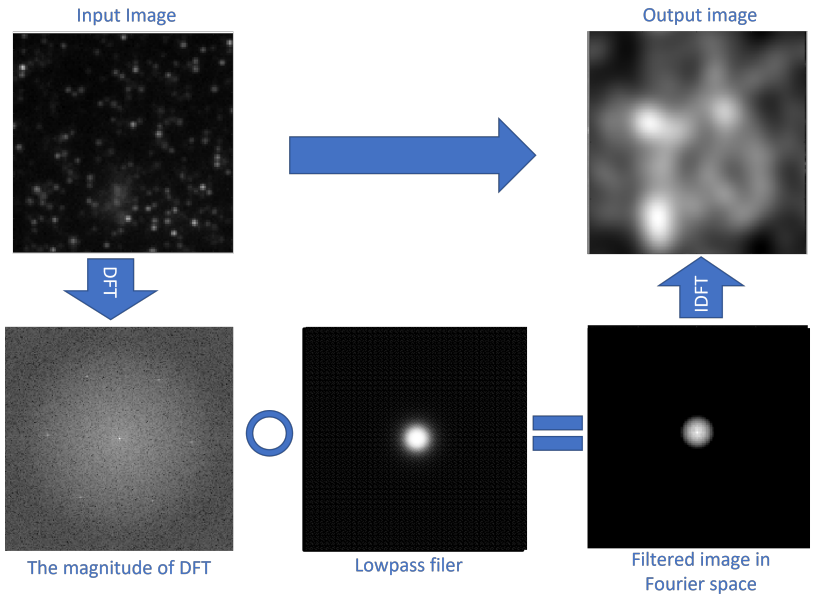

Figure 5.5: The concept of low-pass filtering in Fourier space. The resulting image is the background.

and $(-u_k, -v_k)$ respectively, relative to the center of the frequency rectangle $(M/2, N/2)$. The distance functions are then given by:

$$\begin{aligned} D_k(u,v) &= \left[(u - M/2 - u_k)^2 + (v - N/2 - v_k)^2\right]^{0.5} \\ D_{-k}(u,v) &= \left[(u - M/2 + u_k)^2 + (v - N/2 + v_k)^2\right]^{0.5} \end{aligned} \tag{5.29}$$

A Gaussian Notch Reject filter (GNR) would then be:

$$H_{GNR} = 1 - e^{\left(\frac{-D_k(u_k,v_k)\cdot D_{-k}(-u_k,-v_k)}{D_0^2}\right)} \tag{5.30}$$

5.3.3 Brightfield microscopy for detection improvement

Periodically grown GaP and etched Si nanowires were discussed previously, which are laterally spaced at fixed intervals (p ≈ 1 µm). This regular geometry generates a periodic signal in brightfield and fluorescence images that appears as a distinct peak in the Fourier magnitude spectrum. These peaks correspond to the spatial frequency of the nanowire array,

always present in brightfield images, regardless of fluorophore concentration or imaging conditions.

While spatial domain filters effectively separate high- and low-frequency components, Fourier analysis provides additional benefits by explicitly revealing the nanowire placement pattern. This periodicity is used to enhance detection accuracy through two approaches: (i) image fusion, which combines multiple frames to improve signal-to-noise ratio (especially valuable for low-concentration images), and (ii) Voronoi-plane construction, which uses the lattice to define cell boundaries and systematically remove localization outliers.

5.3.3.1 Image fusion based on frequency domain information

Notch filters are used in various disciplines to identify and/or reject certain frequencies. For example, it can be used in digital image analysis to remove periodic noise from images or applied in spectroscopy for molecular or crystal structure analysis. [168–170]

In this thesis, we describe a method where the lateral locations of nanowires can be identified using Notch filtering using brightfield images, in order to enhance the signal from fluorophores attached to nanowires in widefield fluorescence images. Let's denote fluorescence image as $A(x, y)$ brightfield image as $B(x, y)$, denoting the coordinates in lateral space as (x, y) and coordinates in frequency space as (u, v):

1. FFT of brightfield image:

$$G(u, v) = \mathcal{F}[B(x, y)]$$

2. Notch filtering in frequency domain:

$$G'(u, v) = F(u, v) \circ (1 - H(u, v))$$

3. IFFT of the filtered frequency image:

$$B'(x, y) = \mathcal{F}^{-1}[G'(u, v)]$$

Here, $H(u, v)$ is the band-reject notch filter as defined in equation 5.3.2.2,and it is obtained by localizing peaks in FFT magnitude $G(u, v)$(see figure 5.6a)). The final image, $B'(x, y)$

contains only the information of hexagonal grid of nanowire placement.

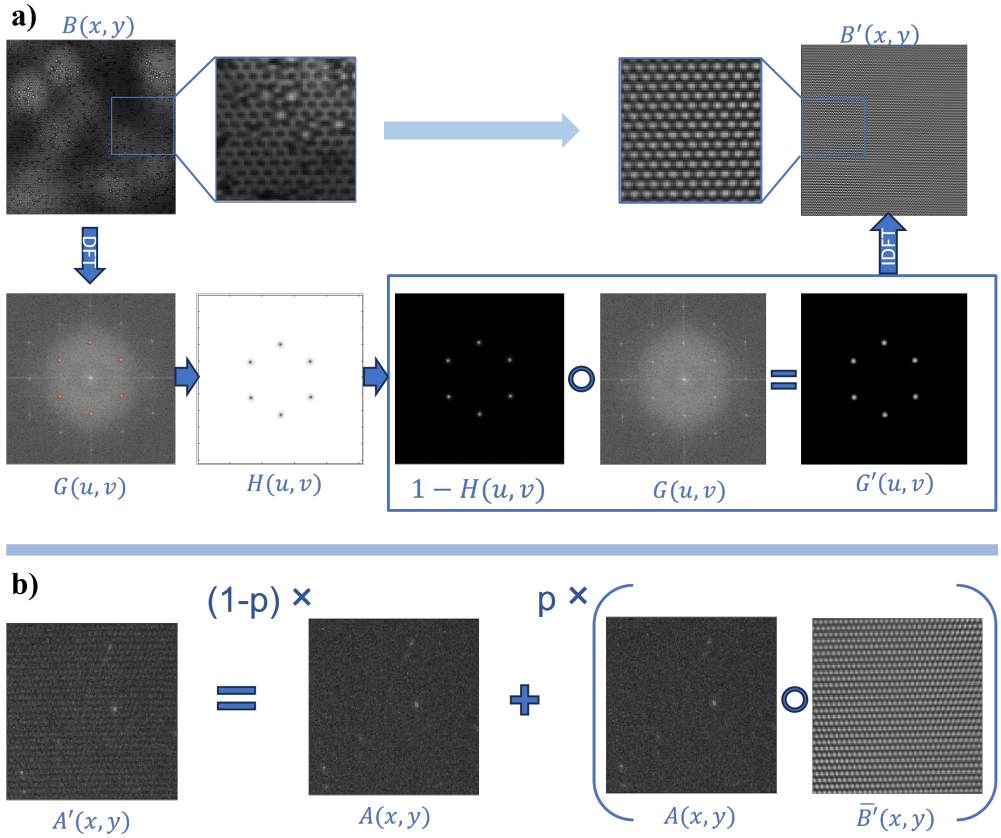

Figure 5.6: **(a)** Brightfield image $B(x,y)$ is transformed into Fourier domain and G(u,v) is obtained. Frequency peaks are obtained from $G(u,v)$, from which the Notch band-reject filter $H_{GNR}(u,v)$ is created. **(b)** The fused image $A'(x,y)$ is obtained by combining the raw image and the grid.

After obtaining the filtered frequncy domain image $B'(x,y)$, the following steps are carried out to perform image fusion:

1. Re-scaling the filtered frequency image $B'(x, y)$ to the range [0,1]:

$$\bar{B}'(x, y) = \frac{B(x, y) - \min(B)}{\max(B) - \min(B)}$$

2. Obtaining the enhanced fluorescence image $A'(x, y)$ through image fusion:

$$A'(x, y) = (1 - p) \cdot A(x, y) + p \cdot \big(A(x, y) \circ \bar{B}'(x, y)\big)$$

Here, $p \in [0, 1]$ is the enhancement ratio and is a user defined value. If $p = 0$, no enhancement is performed and the fused image $A'(x, y)$ is the same as the original image $A(x, y)$. After testing different values for p, we found that $p \in [0.05, 0.1]$, leads to the most accurate performance.

5.3.3.2 Voronoi tesselation

Voronoi diagram, or also called *Voronoi tesselation*, is a partition technique where a plane is divided into regions given a number of defined points, also referred as *seeds*. For each seed, there is a plane, which consists of points closest to that seed, referred to as *Voronoi cell*. [171–173]

The locations of nanowires can be considered as Voronoi seeds, and construct Voronoi cells around them, where each cell will correspond to a local neighborhood of an individual nanowire (see Figure 5.7a). Nanowire locations can be obtained from brightfield images, after performing band-pass Notch filtering according to Figure 5.6. Note, that we assign Voronoi seed locations also to nanowires which are missing or kinked (seen as dark points in brightfield images) to ensure the correct partition of the plane into hexagonal regions.

Once the fluorophores are localized in the fluorescence image (see Figure 5.7 a), these detections match the constructed Voronoi planes. The false-positive exclusion procedure is based on analyzing fluorescence events within each Voronoi cell. For every cell, its geometric center (x_c, y_c) is first computed. If the cell contains any fluorescence points, each point (x_f, y_f) is evaluated by calculating its distance D from the cell center. Points whose distance exceeds a predefined threshold, indicating that they lie unusually far from the local density center, are classified as false positives and removed, while points within the threshold are retained. This procedure is applied to all Voronoi cells to systematically filter spatial outliers.

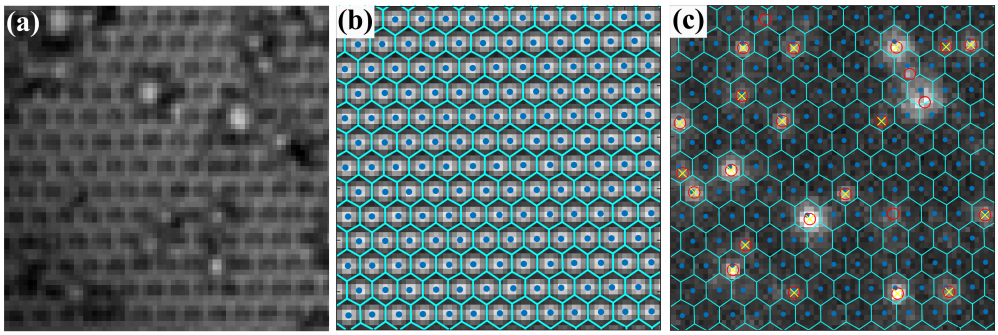

Figure 5.7: A demonstration of Voronoi tesselation for mapping detections to nanowire locations. (a) Shows the unmodified brightfield image, while (b) shows the reconstructed denoised, reconstructed brightfield image with Voronoi cells (cyan hexagons) and Voronoi seeds (blue dots) corresponding to nanowire locations. This is to ensure the symmetry of Voronoi cells, and is based on the assumption of hexagonal growth mask. In (c), Voronoi partition plane is overlayed on a fluorescence image of nanowire-bound fluorophores. Red circles correspond to false positives - localizations which do not match to Voronoi seeds (blue dots). Orange asterisks are true positives - detections which are close to Voronoi seeds.

Note, that this serves as an alternative to more traditional co-localization algorithms. However, since only one detection is expected in each Voronoi cell, this method decreases the computational time, as there is no need to calculate pairwise distances between each nanowire location and obtained detection.

5.3.4 Neural networks for image analysis

Conventional image analysis algorithms enable training-free microscopy data analysis but require extensive parameter tuning, system knowledge, and degrade under low resolution or poor signal-to-noise conditions. [174, 175] Deep learning provides versatile alternatives–CNN-based autoencoders like U-Net [176] for segmentation, denoising, super-resolution, deconvolution, and tasks such as nanowire localization or concentration readout, using simulated datasets as ground truth for low-SNR conditions [177–179]. CNNs employ learnable convolutional filters with nonlinear activations to extract spatial features for classification (discrete labels) or regression (continuous values). [180, 181]

Simulations revealed a key observation: point-spread function (PSF) varies distinctly with fluorophore binding position along the nanowire in the single-molecule detection regime. While this challenges Gaussian fitting and nanowire tip co-localization, it enables 3D detection, potentially tracking 1D molecular diffusion along the nanowire z-axis using standard widefield microscopy. Numerical solutions of Maxwell's equations modeled excitation/emission enhancement to generate synthetic PSFs for neural network training.

These PSF patterns depend on binding location, nanowire-induced optical modifications, and focal plane (Fig. 5.8), allowing axial position retrieval relative to the nanowire surface.

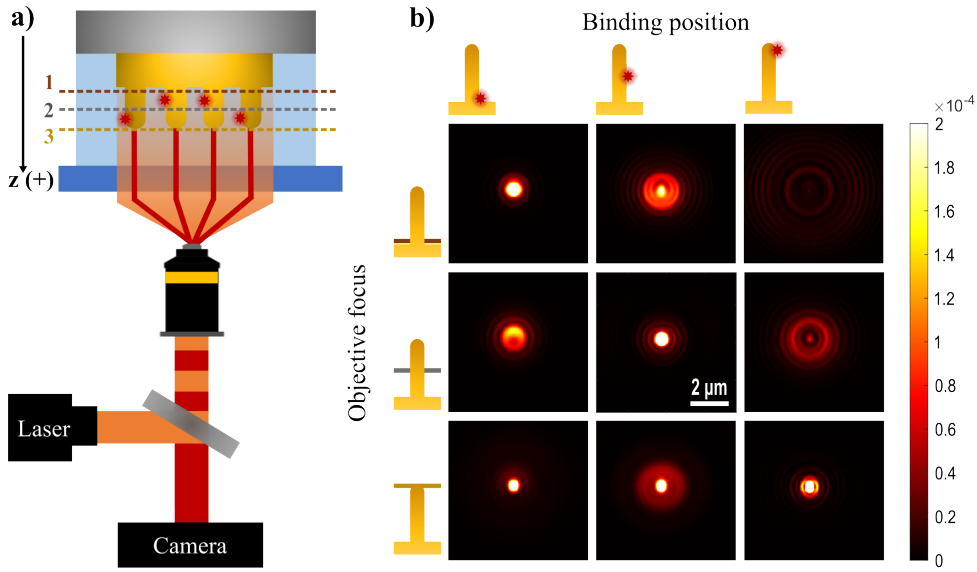

Figure 5.8: z-dependent image formation using semiconductor nanowires. (a) Imaging setup with bottom illumination through liquid medium (orange: excitation; red: emission) at three focal planes: $f_1 = 0.05\ \mu\text{m}$ (bottom), $f_2 = 1.25\ \mu\text{m}$ (center), $f_3 = 2.45\ \mu\text{m}$ (top). (b) Simulated nanowire images with representative fluorophore binding positions matching experimental parameters.

The simplest z-position reconstruction used a regression-based CNN (Fig. 5.9) with three convolutional layers for feature extraction followed by fully connected layers, trained on simulated images with known axial ground truth to predict positions from experimental data.

Realistic simulations matching experimental photon counts, background, and noise ensure robust generalization for axial reconstruction of fluorescently labeled molecules.

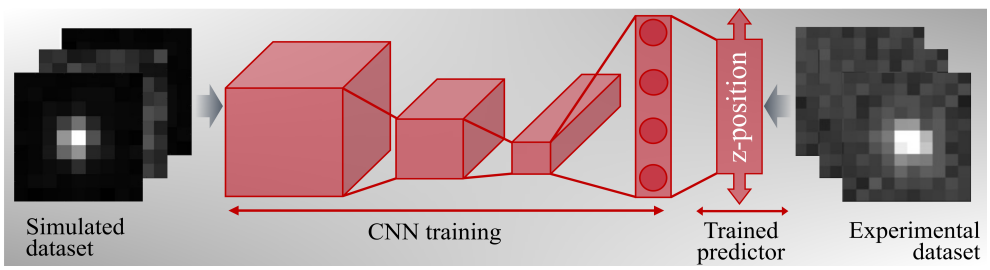

Figure 5.9: Regression CNN architecture for fluorophore axial position prediction: three convolutional layers extract PSF features from simulated/experimental images, followed by fully connected layers outputting continuous z-positions.

Chapter 6

Summary of results

And so, does the destination matter? Or is it the path we take?
I declare that no accomplishment has substance nearly as great as
the road used to achieve it. We are not creatures of destinations.
It is the journey that shapes us.

Brandon Sanderson, The Way of Kings

This chapter provides an overview of the main results presented in this thesis, structured around the key themes of computational tools for enhancing nanowire-based biosensing, the application of scalable and robust polymer-embedded nanowires for biosensing, and the observation and detection of biological processes using nanowire-based platforms.

6.1 Computational tools for nanowire-based biosensing

Nanowire-specific effects such as lightguiding, excitation enhancement, and modified PSFs necessitate customized computational tools for accurate and sensitive image analysis. Building on previous work in single-molecule localization and nanowire optical properties, this thesis develops and validates computational methods specifically tailored for nanowire-enhanced fluorescence microscopy. These tools bridge the gap between experimental imaging and quantitative molecular detection, ultimately improving the sensitivity and reliability of nanowire-based biosensing technologies.

This section summarizes two papers (Paper III and V) that develop computational tools for enhancing nanowire-based molecular detection. Paper III introduces an image analysis toolbox optimized for detecting and quantifying fluorescence signals from nanowire assays across a dynamic range from femtomolar to nanomolar concentrations. Paper V extends these tools for off-plane axial localization of molecules on nanowires, improving 3D spatial resolution.

Both papers validate their methods on simulated datasets before application to experimental imaging, bridging the gap between raw microscopy and quantitative biosensing.

6.1.1 Image analysis optimization (Paper III)

In Paper III, computational image analysis tools push nanowire-based biosensing detection limits across simulated and experimental data, structured into three key components: a simulation framework for synthetic microscopy datasets paired with a quantification toolbox (NanoLoci); application of these tools to real-world experimental assays; and direct benchmarking against conventional planar glass substrates via TIRF microscopy.

This organization reveals how NanoLoci unlocks nanowire advantages—digital counting of sparse emitters (Regime I, <10 pM), intensity integration at higher densities (Regime III), and superior sensitivity over TIRF at low concentrations due to enhanced capture and per-molecule brightness. The pipeline's progressive enhancements (Fourier preprocessing, localization, Voronoi filtering) improves sensitivity, validating fM-nM dynamic range while minimizing variability due to user-parameter selection.

NanoLoci for image analysis optimization

As described in chapter 5.5, we utilize the brightfield images of periodically grown nanowires to determine the positions of the nanowires using fast Fourier transform (FFT) analysis. In simulated data, the positions of nanowires are known, thus we can validate the effect

of additional steps of image pre-processing as of image fusion and post-processing as of exclusion of non-nanowire signals.

To systematically evaluate and optimize the image analysis pipeline for nanowire-based biosensing, we compare three progressively advanced methods for detecting nanowire-associated fluorescence signals (Figure 6.1). While Method 1 is based on single-molecule localization techniques, applicable for nanowires, Methods 2 and 3 introduce specific enhancements tailored to the periodic nanowire geometry (see section 5.5).

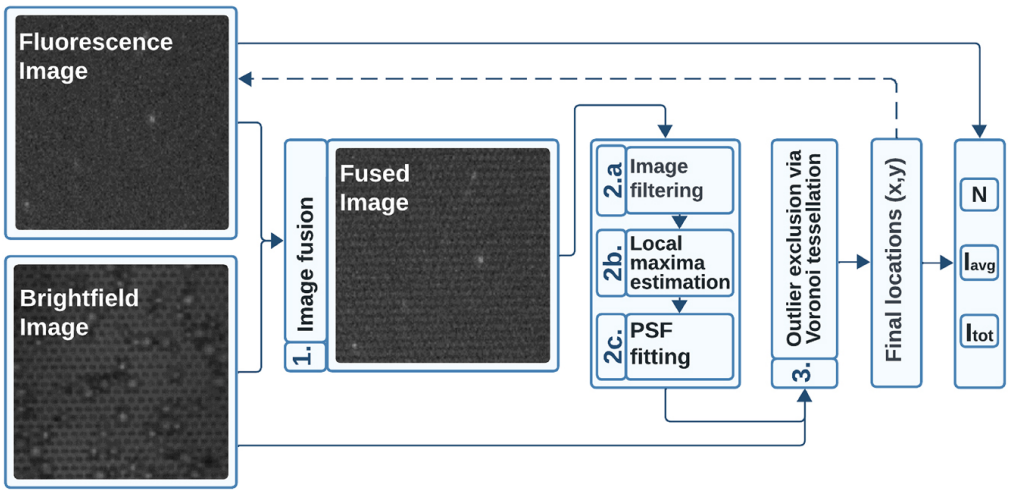

Figure 6.1: Pipeline for single nanowire localization. Brightfield image is used in and optional preprocessing step to enhance the signal originating from nanowires (step 1), followed by single-emitter localization (step 2) and outlier exclusion via Voronoi tessellation (step 3).

- **Method 1:** Conventional single-molecule localization, consisting of:
  1. Image filtering using the *à-trous* wavelet algorithm [162],
  2. Local maxima detection via image dilation and local gradient thresholding [163],
  3. 2D Gaussian fitting for precise subpixel localization [165].

  This method serves as the baseline pipeline (Fig. 6.1, Fig. 2 Step 2).

- **Method 2:** Extends Method 1 by adding Fourier domain image pre-processing to enhance nanowire signal prior to localization. This boosts frequency components corresponding to nanowire positions, improving robustness (Figs. 5.6, 6.1, Fig. 1 Steps 1–2).

- **Method 3 (NanoLoci):** Further extends Method 2 by incorporating outlier exclusion using Voronoi tessellation. This spatial filtering excludes inaccurate detections

inconsistent with expected nanowire tip positions, substantially reducing false positives and improving accuracy (Fig. 5.7, Fig. 6.1, Fig. 2 Steps 1–3).

Together, these methods form a progressive pipeline combining advanced image enhancement, localization, and spatial validation for improved nanowire detection accuracy. We validate and benchmark these methods, accounting for that during analysis, a user-defined threshold is set to distinguish true nanowire signals from background noise. This threshold is optimized for each method to maximize detection accuracy. Thus, we compare the methods for varying thresholds to compare the performance and robustness of each method. We also vary the matching distance parameter used to associate detected fluorophore positions with known nanowire locations, assessing its impact on detection accuracy.

The accuracy of nanowire detection was evaluated using a simulated dataset by comparing detected fluorophore positions with known ground truth locations. The analysis varied two key parameters: the gradient detection threshold G_{min} and the matching distance between detections (See Figure 6.2).

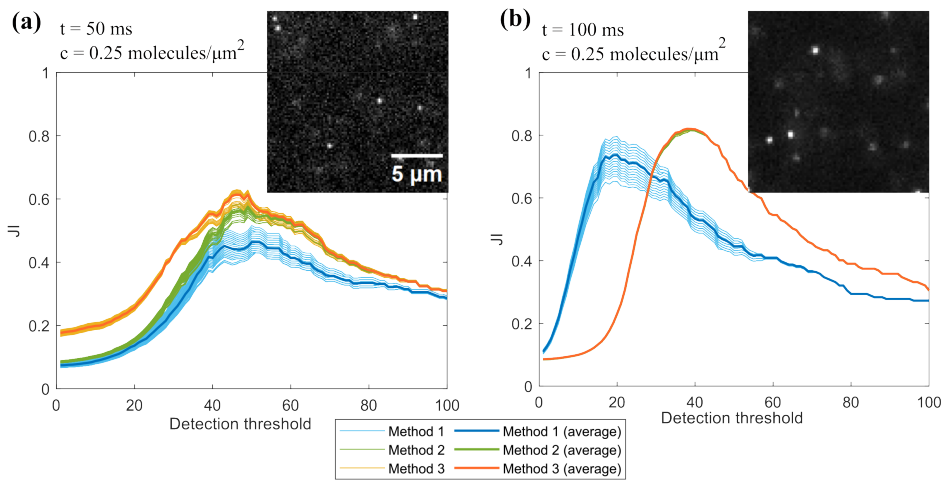

Figure 6.2: Comparison of detection accuracy across three methods for varying thresholds and matching distances. Varything thresholds are on x-axis, while the different matching distances are shown in dashed lines. (a) t = 50 ms and (b) t = 100 ms simulated exposure times. Light blue, green and orange lines represent the variation of detection matching distance d_m in the range from 1.2 and 1.5 pixels for Method 1, Method 2 and Method 3, respectively. The darker blue lines represent the averaged JIs for all tested values d_m.

A linear adjustment of the detection threshold was applied for Methods 2 and 3 according to:

$$G'_{min} = (1 + p) \times G_{min},$$

where p is the enhancement ratio, set to 0.05 and 0.1 for Methods 2 and 3, respectively.

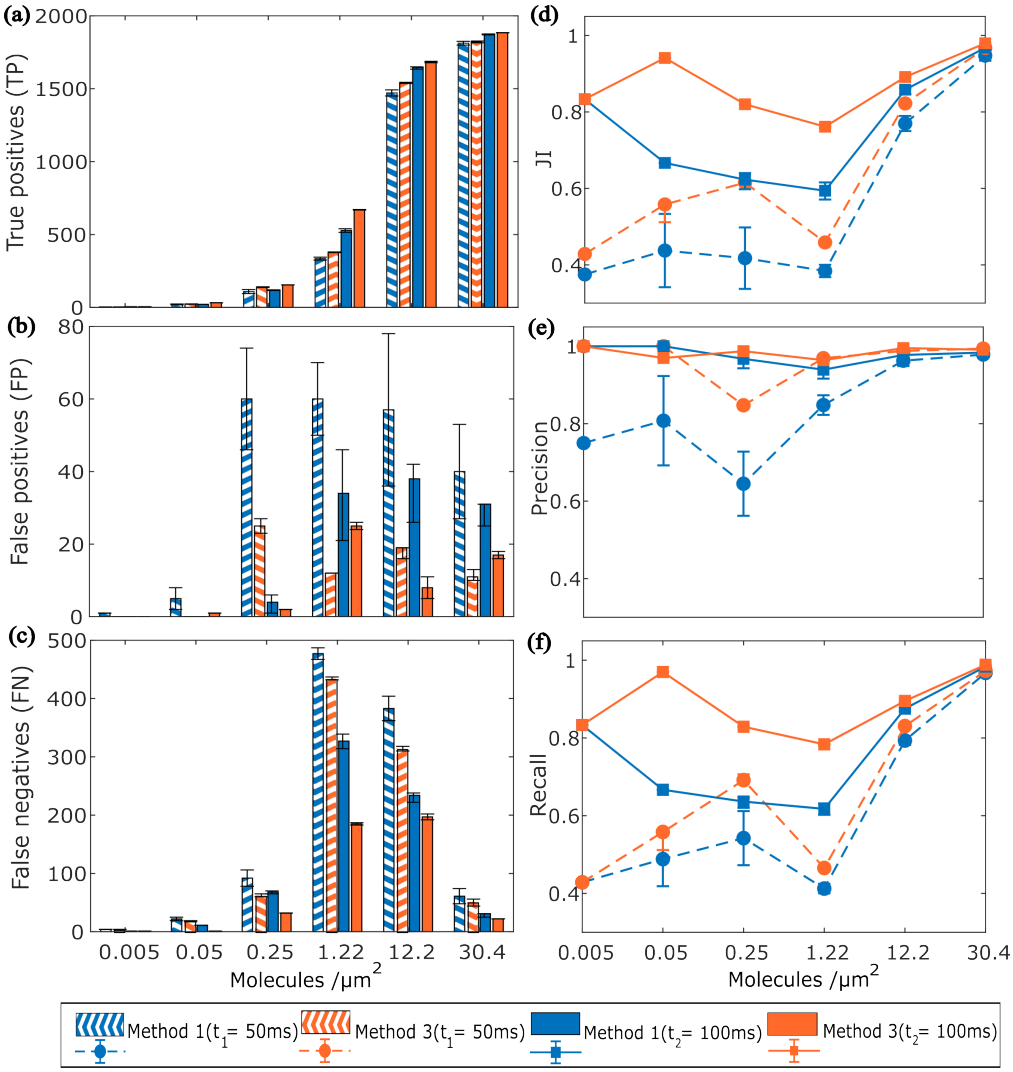

Figure 6.3: Comparison of detection accuracies for exposure times $t = 100$ ms and $t = 50$ ms, between Method 1 (blue) and Method 3 (NanoLoci, orange). Values were calculated using a matching distance of $d_m = 1.4$ pixels, with upper and lower error bounds at $d_m^+ = 1.5$ pixels and $d_m^- = 1.3$ pixels, respectively. a) Both methods detect more true positives (TPs) at longer exposure times due to increased photon emission. b) Method 1 exhibits significantly higher false positives (FPs) at $t = 50$ ms, indicating non-specific detections. Method 3 reduces FPs in both conditions, improving Precision (panel e). Precision improvement is particularly notable (about 20%) for concentrations $c < 1.22$ molecules/μm^2 at $t = 50$ ms, while remaining stable at $t = 100$ ms. c) Compared to Method 1, Method 3 decreases false negatives (FNs) especially at intermediate concentrations, boosting Recall (panel f) by 10–30% for concentrations $c = 0.005, 0.05, 0.25$ molecules/μm^2. d) By lowering both FP and FN rates while increasing TPs, Method 3 improves the Jaccard Index (JI) by 5–30% across concentrations $c = 0.05, 0.05, 0.25$ molecules/μm^2.

Detection accuracy was quantified by the Jaccard Index (JI) [182], Precision, and Recall metrics across a range of concentrations and two exposure times (50 ms and 100 ms). Method 2, which employs image fusion in the Fourier domain, consistently outperformed Method 1,

achieving a 10–15% increase in JI at optimal thresholds. Method 3 provided further, though modest, improvements, particularly at lower photon emission rates (Figure 6.2).

Notably, the peak detection performance shifted towards higher threshold values with image fusion techniques, reflecting enhanced robustness to threshold choice. Variations in matching distance had a significant impact on Method 1's accuracy but produced minimal effects for Methods 2 and 3, indicating improved tolerance and more precise alignment of detected points with actual nanowire locations. Across the simulated concentration range, Method 3 (NanoLoci) demonstrated significant improvements in detection accuracy by substantially reducing false positives (FPs) and false negatives (FNs), particularly at intermediate nanowire concentrations. This reduction directly improved both Precision, defined as the fraction of correct positive identifications, and Recall, the fraction of true nanowire locations correctly detected. Improvements ranged from approximately 5% to 30%, depending on fluorophore concentration and photon emission rate during imaging (See Figure 6.3).

At intermediate concentrations, where distinguishing true nanowire signals from background is more difficult, Method 3 effectively lowered error rates, resulting in higher confidence in detection. At higher concentrations, detection performance remained stable, demonstrating robustness over a broad dynamic range. Furthermore, the image fusion and processing algorithms in Method 3 enhance signal localization quality and reduce sensitivity to parameter choices, such as matching distance threshold, leading to more stable detection across various imaging conditions.

Overall, these attributes make Method 3 especially suitable for challenging imaging scenarios characterized by low photon counts and medium target densities, where precise and reliable nanowire tip localization is critical. This robustness and accuracy establish Method 3 (NanoLoci) as the most effective pipeline among those tested for nanowire detection in simulated fluorescence microscopy data.

Experimental validation

The optimized image analysis pipeline (Method 3, NanoLoci) was validated on experimental fluorescence microscopy data from nanowire-based biosensing assays using GaP nanowire platforms functionalized with Alexa Fluor 647-labeled streptavidin. Substrates were incubated with concentrations spanning 10 fM to 10 nM (see Figure 6.4), revealing three distinct detection regimes: Regime I (<10 pM, digital single-molecule counting via sparse bright nanowires), Regime II (intermediate, variable binding per nanowire), and Regime III (>10 pM, saturated multi-molecule emission).

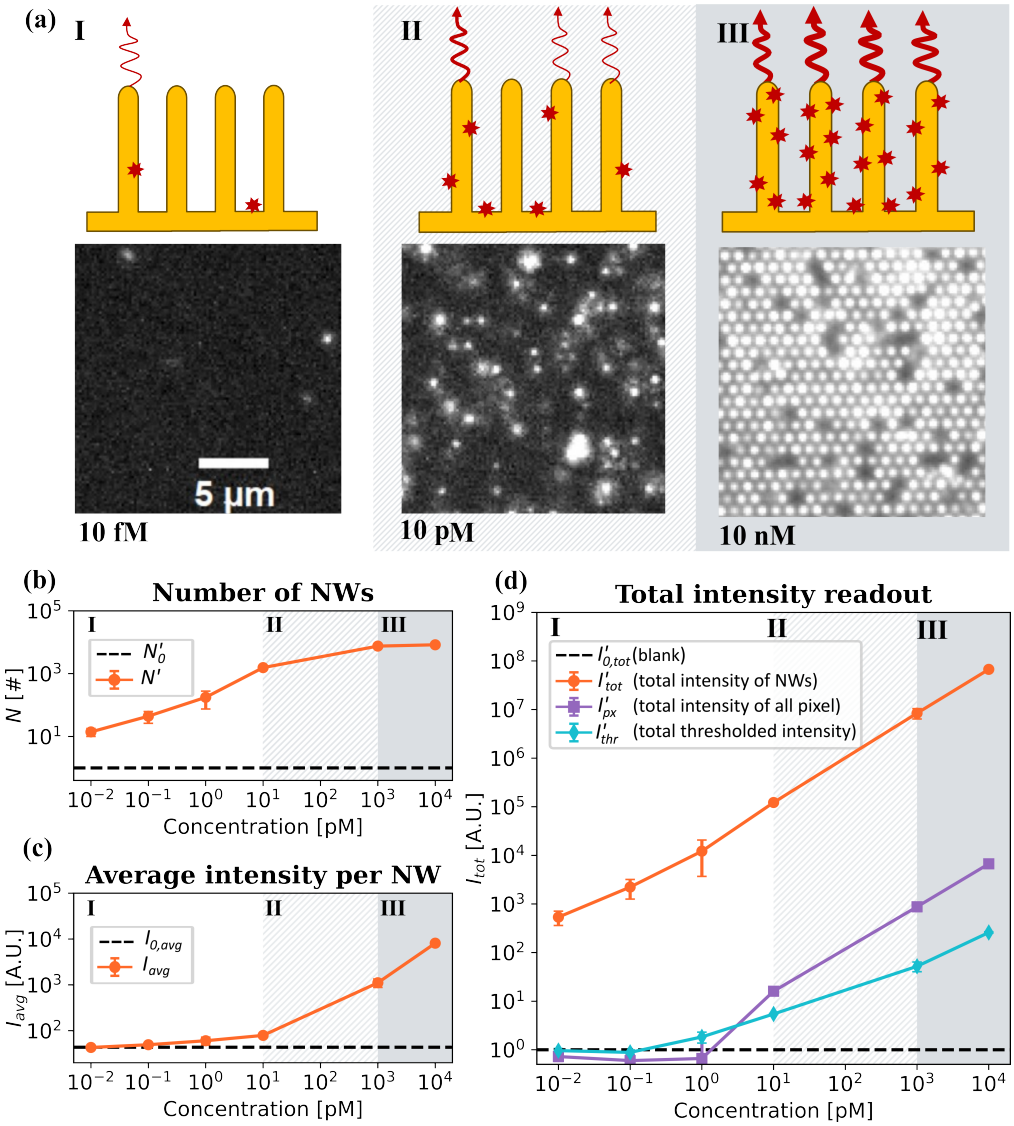

Figure 6.4: Titration experiments of Stv-Alexa647 binding to a nanowire array. (a) Micrographs showing fluorescence emission upon addition of Stv-Alexa647 at 10 fM, 10 pM, and 10 nM concentrations. The illustrations depict the three identified regimes (see main text). (b) The normalized number of localized bright nanowires (N') versus Stv-Alexa647 concentration. (c) The average intensity per bright nanowire (I_{avg}) plotted against Stv-Alexa647 concentration (orange curve). The dashed black line indicates the average intensity from blank measurements. (d) The normalized total intensity detected from nanowires (I'_{tot}), serving as the readout signal (orange curve). Non-single-emitter methods, including pixel-value averaging (I'_{px}, purple) and thresholded pixel-value averaging (I'_{thr}, cyan), are plotted for comparison. Detections from blank images were used to normalize both the number of molecules (b) and total intensities (d).

Three comparison metrics, were used to evaluate detection performance across the concentration range: (i) normalized number of localized bright nanowires (N'), (ii) average

intensity per bright nanowire (I_{avg}), and (iii) total normalized intensity from all nanowires (I'_{tot}). N' and I'_{tot} were normalized against blank measurements in the absence of labeled streptavidin to account for background fluorescence.

I'_{tot} demonstrated linear response across all five orders of magnitude (10 fM–10 nM), outperforming non-localization methods by 2–3 orders in limit of detection. Pixel averaging detected from 10 pM (2-order dynamic range), while simple thresholding saturated earlier; NanoLoci enabled precise nanowire counting in Regime I (Figure 6.4 b) and intensity integration in Regimes II/III, confirming improved sensitivity (Figure 6.4 c-d).

Direct comparison to TIRF microscopy on identical substrates (same microfluidic channel, conditions) showed nanowire-enhanced widefield fluorescence achieving ∼2x higher sensitivity at lowest concentrations, due to elevated protein capture rates and per-molecule brightness from lightguiding.

6.1.2 Off-plane localization of molecules on nanowires (Paper V)

Where in Paper III we developed computational tools for detecting molecules on nanowires in 2D, Paper V builds upon this to extend the analysis to detect off -plane axial positions of molecules with respect to the nanowire z-axis. This advancement enables true three-dimensional localization in nanowire-enhanced microscopy, enabling more detailed studies of molecular interactions on nanowires.

The methodology involves simulating the PSF for molecules at various axial positions on the nanowire and developing a convolutional neural network (CNN) model trained on these simulations to perform a regression of the axial positions based on the observed PSF patterns. The axial position dependant images are simulated with 50 nm steps along nanowire axis, using the simulation framework described in *5.1 Modeling of nanowires as optical sensors*. Thus, the model is informed of PSF and the excitation and emission modifications along nanowire axis.

CNNs were trained as regression models to predict the axial position of a fluorophore attached to a nanowire. The input consisted of simulated grayscale images of individual nanowires with the corresponding axial positions provided as labels. The CNN architecture included three convolutional blocks with increasing filter sizes (128, 256, 512), each followed by batch normalization, ReLU activation, and max pooling (stride 2). A dropout layer was applied before the final regression layer, which used a mean absolute error (L1) loss function. The Adam optimizer was used for training.

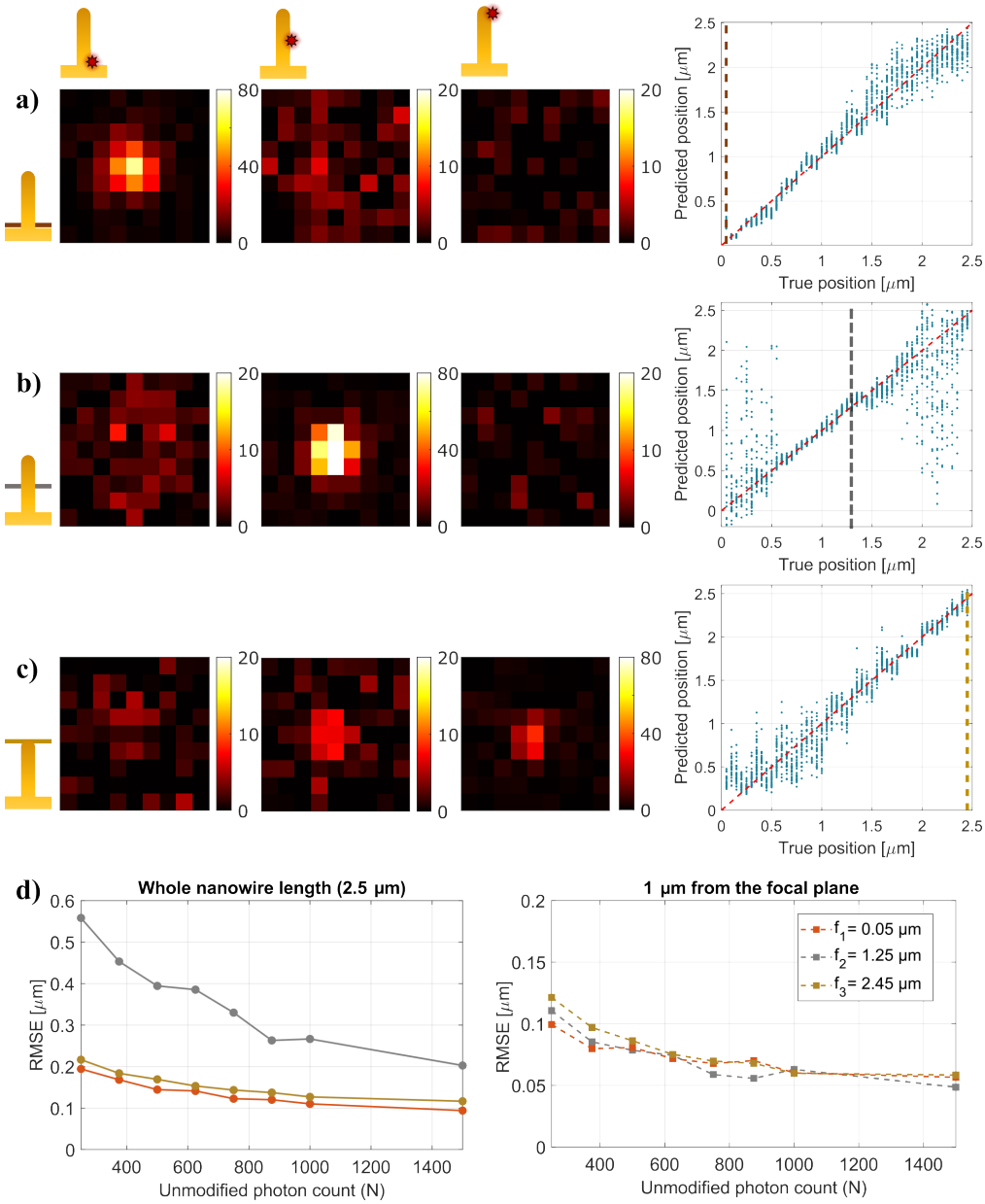

Figure 6.5: Predicted positions for simulated and experimental data with two focal planes. a) Two focal planes were chosen to train the model: bottom ($f_1 = 0.05\ \mu\text{m}$) and top ($f_3 = 2.45\ \mu\text{m}$) of the nanowire platform. The true positions and predictions of the two-focus model on simulated data are shown for b1) a fixed photon count of 500 and b2) a variable photon count ranging from 250 to 600. Panels c1) and c2) show the distributions of predicted z-positions for the simulated validation and experimental datasets, respectively, and panel c3) provides a box plot comparison of these two distributions. The experimental data were acquired by taking z-stack images of Alexa647-labeled streptavidin bound to the nanowires. The top and bottom focal planes were estimated using the brightfield images.

Three focal planes were simulated at the bottom ($f_1 = 0.05\ \mu\mathrm{m}$), middle ($f_2 = 1.25\ \mu\mathrm{m}$), and top ($f_3 = 2.45\ \mu\mathrm{m}$) of the platform (Fig. 4). For each plane, the point spread function (PSF) of a fluorophore bound to a single nanowire was generated, and a neural network was trained to predict its z-position. When focused at the top or bottom, PSFs appeared approximately symmetric; prediction accuracy declined notably beyond 1.5 μm from the focal plane, causing randomly distributed position errors. Focusing at the center increased errors near nanowire edges where tip and base were occasionally confused, as expected from lightguiding effects.

Varying photon counts from 250 to 1500 photons per image confirmed accuracy improves with intensity (Fig. 4d). Over the entire nanowire, focusing at top or bottom performed best. Within $\pm 1\ \mu\mathrm{m}$ of the focal plane, all three positions showed comparable root-mean-square-errors, decreasing from 125 nm to about 50 nm as photon counts rose.

Our simulations demonstrate that convolutional neural networks trained on synthetic data achieve sub-100 nm accuracy up to $\sim 1\ \mu\mathrm{m}$ from the focal plane (with 50 nm step size). This highlights the potential of CNN-based approaches for high-resolution axial estimation, while noting limits from laser intensity decay, microscope resolution, and photon statistics. Centering the focus near the nanowire's axial center yields uniform illumination but edge regions remain prone to artifacts, emphasizing the importance of careful focal-plane selection in experiments.

6.2 Polymer-embedded nanowires for biosensing

The majority of nanowire-based biosensing studies which are part of this thesis use substrate grown or etched nanowires (Papers II-V). While these nanowires are an excellent platform for fundamental studies and sensitive biodetection, they have limitations in terms of product scalability and bulkiness for practical applications. To address these limitations, we explore the use of polymer-embedded nanowires as a robust and scalable platform.

This section summarizes two papers (Paper I and VI) that focus on the development and application of polymer-embedded nanowires for biosensing. In Paper I, we demonstrate the fabrication a comparison of these nanowires compared to traditional substrate-grown nanowires, demonstrating comparable performance. Paper VI builds on this knowledge to utilize yet another advantage of nanowires embedded in transparent polymer - the ability to illuminate the samples through the polymer, allowing biosensing in non-transparent media, including whole human blood.

6.2.1 Aerotaxy nanowires for biosensing (Paper I)

This paper presents the characterization of optical biosensing platforms based on Ga(As)P semiconductor nanowires grown by aerotaxy, a novel high-throughput method without the need of substrate. While these nanowires are more scalable and cost-effective in terms of production, their performance as a potential biosensing platform has not been previously established.

The study compares two nanowire platforms: (1) aerotaxy-grown Ga(As)P nanowires vertically aligned on polymer substrates and (2) epitaxially grown GaP nanowires organized on GaP substrates. Both platforms were coated with silicon dioxide and functionalized with fluorescently labeled biomolecules to evaluate their fluorescence enhancement capabilities compared to planar glass substrates. On planar glass substrates, it is unlikely to observe individual molecules in widefield microscopy, due to limited sensitivity. However, both nanowire platforms enable single-molecule detection, as individual nanowires appear as bright spots in fluorescence images (Figure 6.6 a-f).

Results show that epitaxial GaP nanowires offer a roughly 2-fold fluorescence enhancement over planar glass surfaces, while aerotaxy nanowires provide about a 1-fold increase in overall fluorescence intensities (Figure 6.6 g-h). The difference in enhancement is attributed primarily to the higher density, uniformity, and crystallinity of epitaxial nanowires. Aerotaxy nanowires were found to have larger diameters, some tapering, and occasional defects, as well as thicker oxide coatings ($\sim$30 nm compared to $\sim$ 10 nm for epitaxy), all factors slightly reducing their signal enhancement. At the single nanowire level, both platforms demonstrate comparable fluorescence enhancement, with aerotaxy nanowires showing larger variability in intensities in single molecule range (Figure 6.6 i). The detection at low concentrations (below 10 pM) confirms the capacity for detection down to the single molecule level, highlighting the high sensitivity offered by these nanowire biosensors.

With further optimization to increase nanowire density and improve uniformity, aerotaxy nanowire platforms offer a promising route for scalable fabrication of optical biosensors capable of sensitive and multiplexed biomolecular detection.

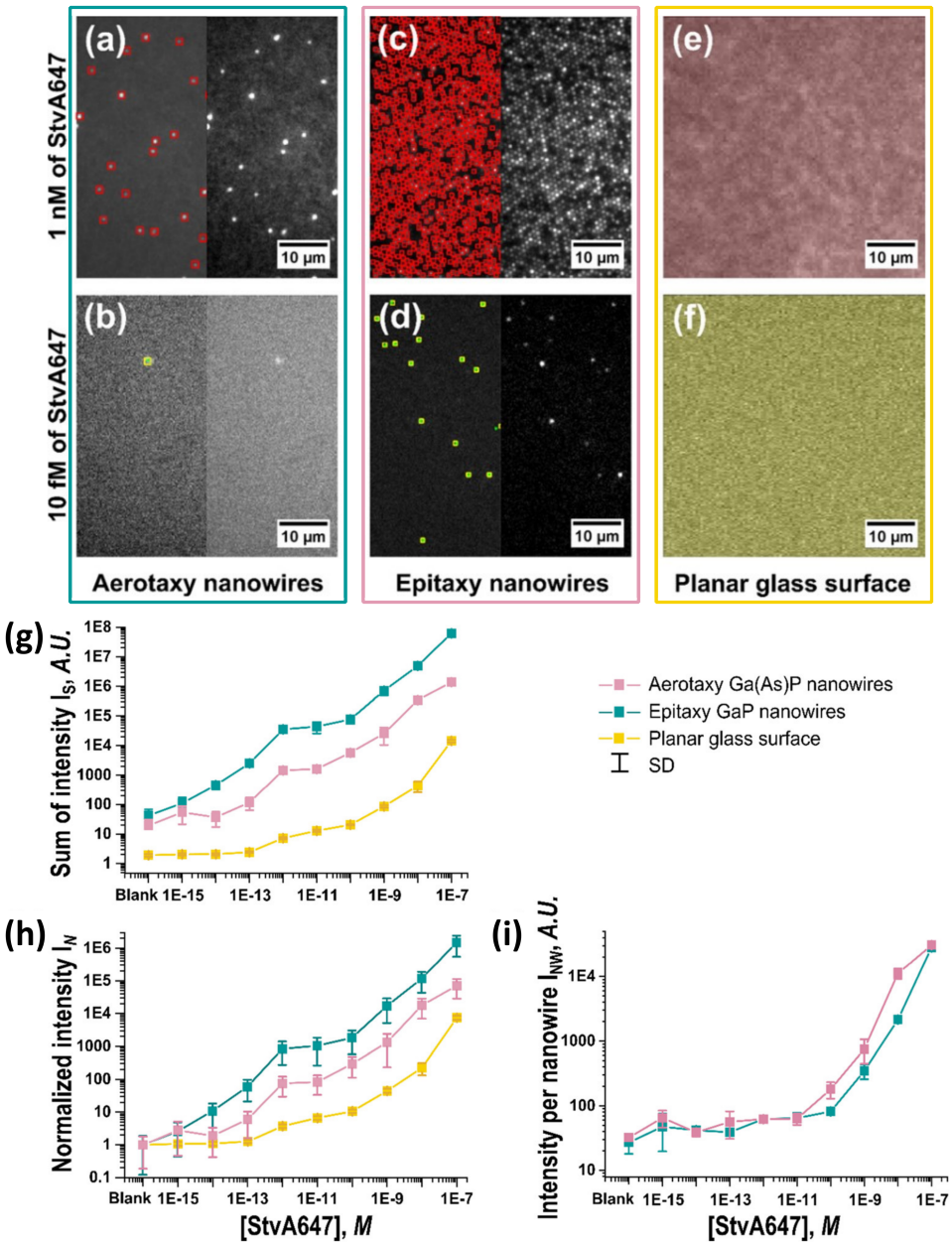

Figure 6.6: Examples of image analysis for the calculations of fluorescence intensity on ROIs of the three evaluated surfaces, for high (top row) and low (bottom row) concentrations of StvA647, respectively. (a,b) For aerotaxy Ga(As)P nanowire platforms, the intensity is calculated as the sum of intensity on the localized nanowires. Left and right are the same image with and without the detections highlighted. (c,d) Epitaxy GaP nanowire platforms. (e,f) On planar glass slides, the intensity is extracted as the sum of intensity per pixel for all the ROIs.(g) Sum of signal intensity as a function of concentration of StvA647 for aerotaxy nanowires, epitaxy nanowires, and planar controls, as indicated in the legend. (h) IN, the signal intensity of the samples normalized to the blank. (i) Average intensity per nanowire, for all detected bright nanowires.

6.2.2 Biosensing in blood (Paper VI)

Paper VI explores lightguiding nanowires for fluorescence-based biosensing in optically non-transparent media, including whole blood, milk, and lipid emulsions. Given typical microfluidic channel dimensions (50–200 µm) and high scattering coefficients ($\mu_s \approx 10$–100 mm^{-1}), light propagation through these media is in the multiple scattering regime. For blood in a conventional IBIDI channel with a height of 0.4 mm at 640 nm excitation, yields $\mu_s l_p \approx 40 \gg 1$. The scattering coefficients of lipid emulsions are higher around 10 times compared to blood [183], making them even more challenging for optical detection. Milk, on the other hand, has a dilution of fats, thus being less scattering but more complex biologically.

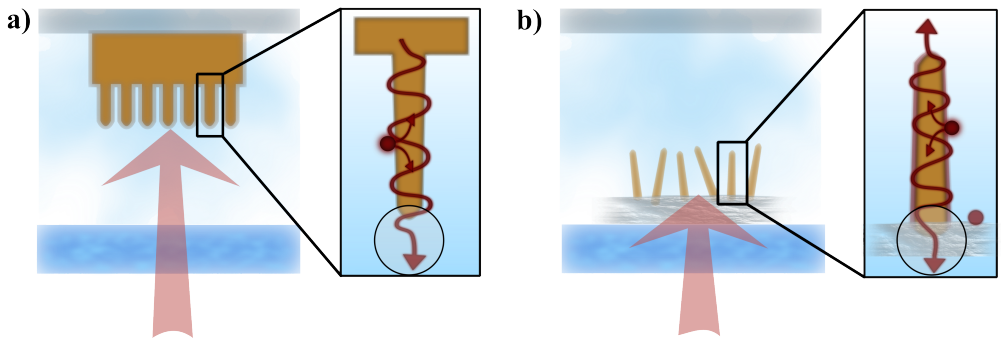

Figure 6.7: Schematic of polymer-embedded nanowire for biosensing in optically non-transparent media. (a) The nanowire configuration used in Papers I-V: the nanowires are attached to the upper surface of the microfluidic channel, with excitation and emission collection occurring through the turbid medium. (b) The reverse geometry employed in Paper VI: nanowires are attached to the bottom surface, with excitation and emission collection occurring through the transparent polymer substrate, bypassing the turbid medium.

Polymer-embedded nanowires address this challenge through two key steps: (i) elimination of thick semiconductor substrate, allowing direct attachment to coverglass, and (ii) emission collection from the polymer side ($n \approx 1.45$, optically transparent like glass) bypasses scattering in the turbid medium above (see Figure 6.7). While the nanowire is immersed in the non-transparent biofluid, light is guided and collected from the transparent polymer substrate, enabling efficient signal detection.

Brightfield imaging was discussed intensively in this thesis, however, in presence of highly scattering media, this type of imaging becomes less informative. In transparent buffer, the nanowires appear as dark spots on a bright background, while in blood, the scattering from blood cells creates a noisy background, making it difficult to visually identify the nanowires (Figure 6.8 b,e). Fluence simulations further confirm that while light propagation is seriously hindered in blood and significantly scattered within the medium (Figure 6.8 a,d). However, fluorescence imaging reveals that the fluorescence signal from nanowires is com-

parable in both transparent buffer and blood (Figure 6.8 c,f).

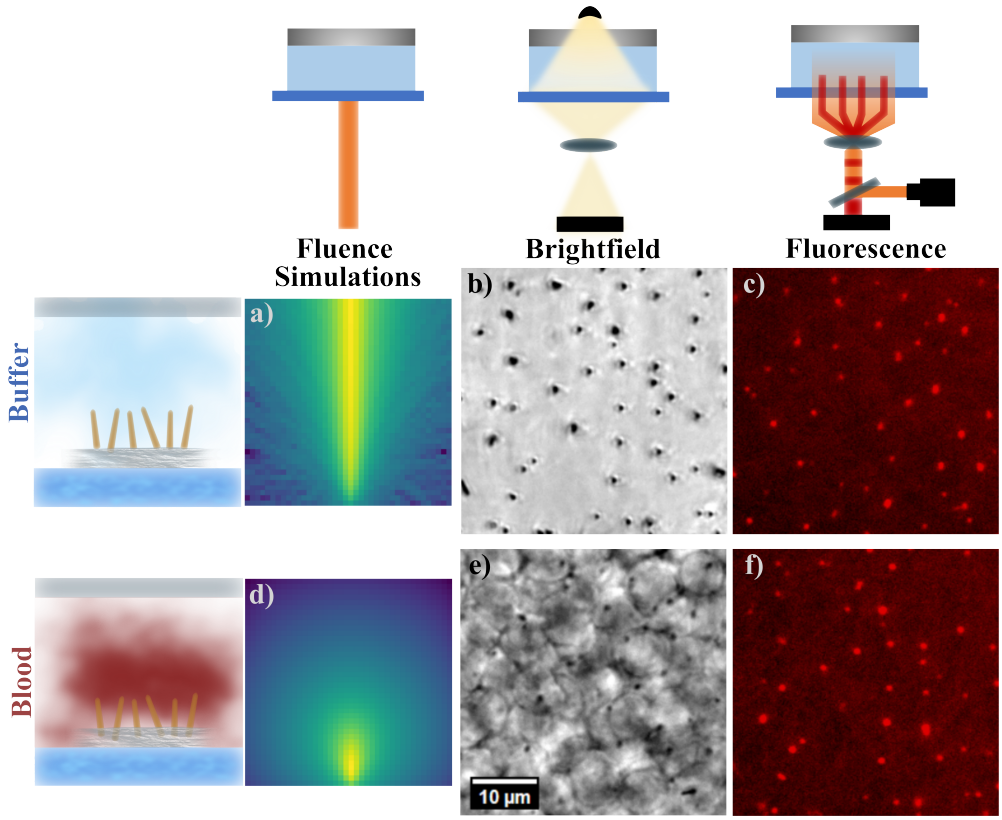

Figure 6.8: Detection in transparent buffer and blood. Columns (left to right): channel visualization, fluence simulations based on channel geometry, brightfield and fluorescence images. Rows (top to bottom): Sketches of simulation illumination and experimental imaging techniques. (a, d) Simulated fluence shows that in case of buffer, the light can travel through sample matrix with much less scattering, as compared to blood. (b,e) Brightfield image, using illumination from top, shows a clear pattern of nanowires as dark spots on bright background, while in presence of blood, it is more difficult to see the nanowires. (c,f) Fluorescence signal detected from buffer and blood is comparable, and seemingly, unmodified, despite the large difference in brightfield images.

The lowest concentration detected in blood and transparent buffer are 0.1 nM for both cases as can be observed in Figure 6.9. The fluorescence intensities detected from nanowires in blood are comparable to those in transparent buffer, indicating that the nanowire-based biosensing platform maintains its sensitivity even in the presence of complex biological media. This demonstrates the robustness and versatility of the polymer-embedded nanowire platform for biosensing applications in challenging environments.

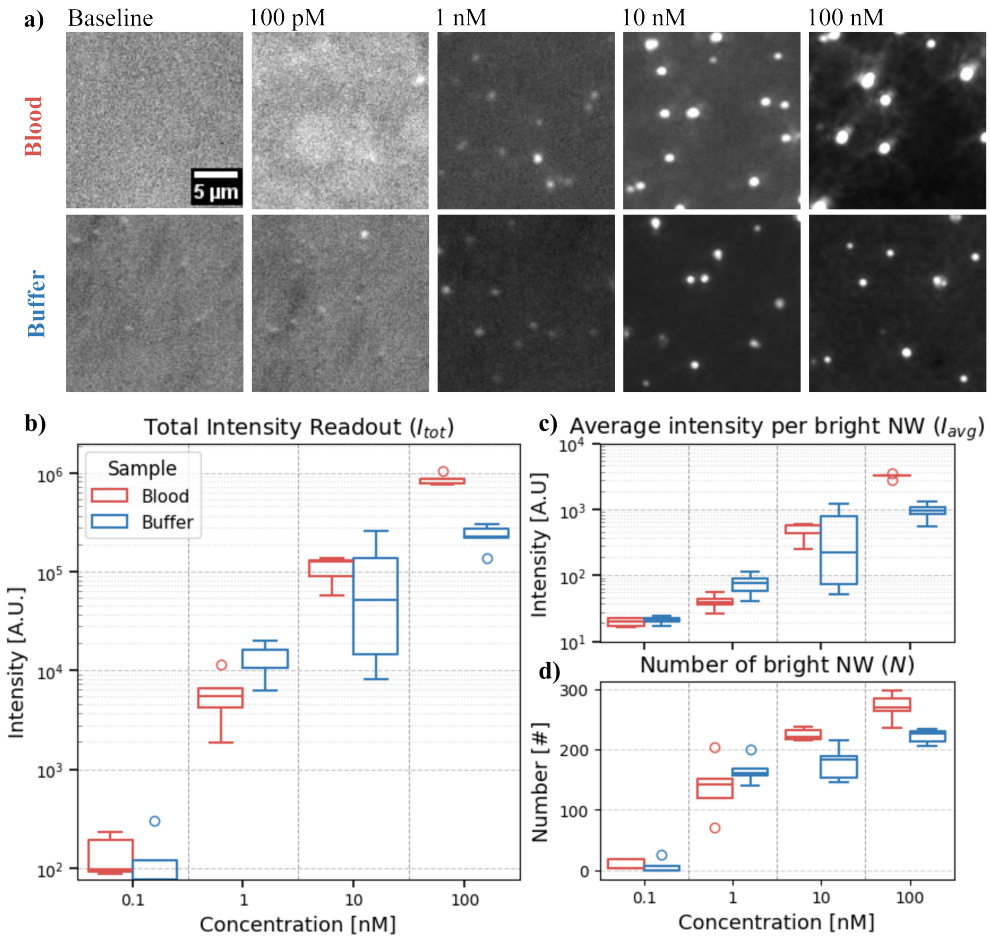

Figure 6.9: Comparison between buffer and blood. a) Representative fluorescence images for buffer and blood. b) Total intensity readout for measured concentrations, normalized by subtracting the total intensity of the baseline. c) Average intensity values per detected bright nanowire indicate the amount of binding on individual nanowires. d) The number of bright nanowires, which eventually saturates when all nanowires in the field of view are bright.

In addition to whole blood, we also demonstrate detection in two other optically non-transparent media: milk and lipid emulsions. For lipid emulsions, we achieve a detection limit of 0.1 nM, the same as in blood and transparent buffer. For milk, the detection limit is slightly higher at 1 nM, likely due to its more complex biological composition affecting binding efficiency. Overall, these results highlight the potential of polymer-embedded nanowire platforms for sensitive biosensing in a variety of challenging biological fluids.

Compared to Paper II, where similar polymer-embedded nanowires were used, the achieved detection limit is higher here. However, this is independent of media type. One reason for this is the change in illumination geometry: while light collection through the polymer

is the key factor to bypass scattering, light collection plane within the polymer might perform worse than when the light is collected from exposed nanowires. Paper II uses water immersion objective to collect light through aqueous media, while here the same objective is focused on a polymer with higher refractive index. This mismatch may lead to aberrations and reduced collection efficiency, thus affecting sensitivity. Further optimization of the optical setup and nanowire functionalization could help improve detection limits in future studies.

6.3 Observing biological processes

The previous two papers are mainly focused on the development of nanowire-based biosensing platforms and computational tools to enhance detection capabilities. Different in their focus, they all share the same biological assay, namely streptavidin-biotin binding. In all these papers, we develop different methods and look from different perspectives, the biological tool is the same.

This section summarizes two papers (Paper II and IV) that focus on using nanowire-based platforms to observe biological processes. In paper II, we utilize nanowire-based biosensing to detect molecular beacons. While still a proof-of-concept, it is more representative to real biological assay, as the molecular beacons are immobilized on the nanowires and open once they hybridize to the target oligonucleotide. Paper IV takes the more complex biological system described here - supported lipid bilayers formed on nanowires - and compares the formation kinetics on nanowires to planar surfaces.

Both studies are dynamic in nature, thus requiring real-time monitoring of biological interactions. Therefore, in this case, custom-made microfluidic chambers are used both to (i) minimize the effect of the bulky substrate and (ii) ensure the appropriate sample delivery to the nanowire sensors.

6.3.1 Oligonucleotide detection with molecular beacons (Paper II)

In this paper, we demonstrate the application of nanowire-based optical biosensing for the detection of specific oligonucleotide sequences using molecular beacons.

The nanowires employed in this study are epitaxially grown GaP nanowires coated with a thin silica layer. As illustrated in Figure 6.10 a, the functionalization process involves immobilizing molecular beacons on the nanowire surface via biotin–streptavidin interactions. These molecular beacons are designed to emit fluorescence upon hybridization with their complementary target oligonucleotides.

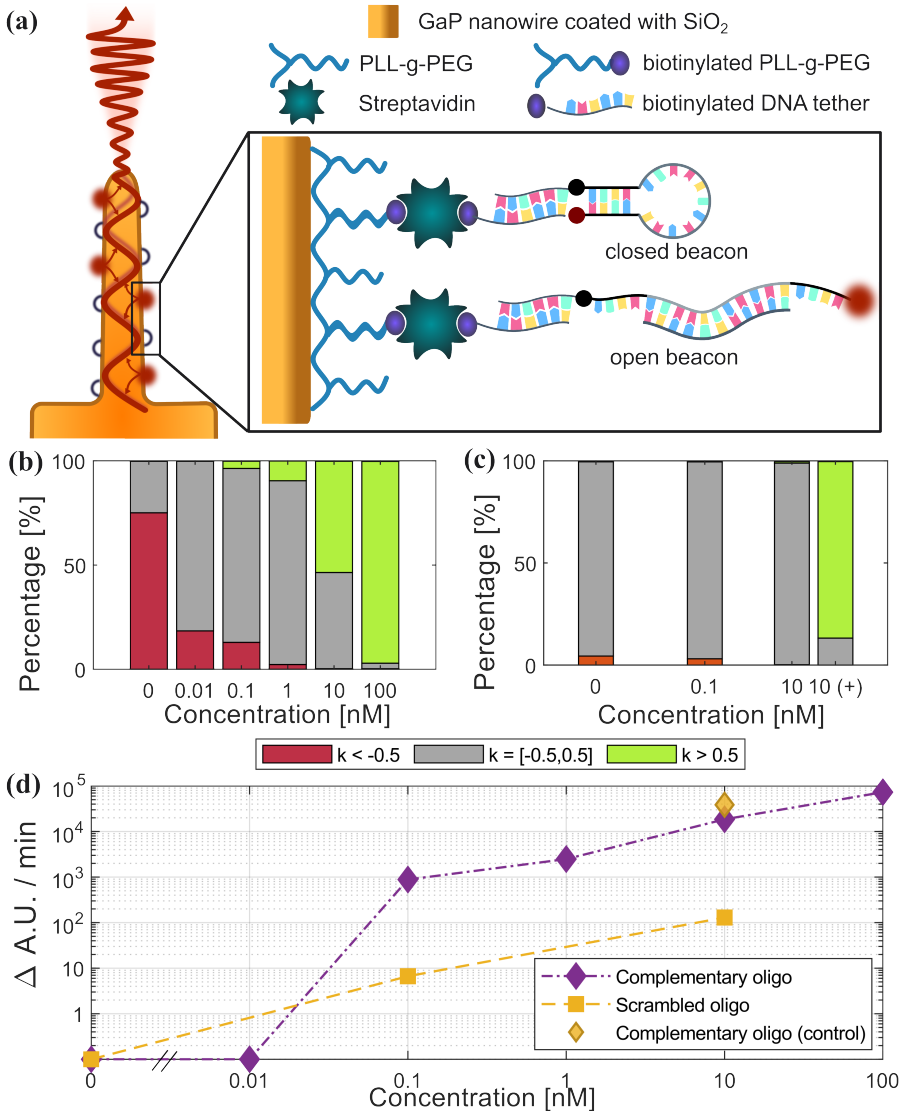

Figure 6.10: Oligonucleotide detection using molecular beacons immobilized on nanowires. a) Schematic of light-guiding nanowire, with immobilized MBs and functionalization layers. When target oligonucleotides bind to MBs, fluorescence is emitted and guided through the nanowire. b) The percentage of the nanowires with increasing, constant and decreasing intensities for target oligonucleotides c) Same for scrambled oligonucleotides. d) Sum of the line coefficients k for the NWs with an increasing fluorescence signal only respectively for target and scrambled oligonucleotides.

The experimental design enables real-time monitoring of the molecular beacons' conformational changes. Initially, a baseline fluorescence signal is established from nanowires with immobilized molecular beacons in the absence of target oligonucleotides. Ideally, little fluorescence is expected since the beacons remain in a closed conformation. However,

thermal fluctuations may occasionally induce spontaneous opening, producing a low-level fluorescence background. We found that while absolute fluorescence intensity provides some information, the dynamic change in signal over time is a more reliable indicator. Consequently, the fluorescence intensity of each nanowire is monitored individually, as each acts as an independent sensor.

To quantify this change, a linear model is fitted to the fluorescence intensity trace of each nanowire over time. Based on the linear coefficient k, the nanowires are categorized into three groups: (i) increasing intensity ($k > 0.5$, indicating beacon opening), (ii) decreasing intensity ($k < 0$, indicating closing or photobleaching), and (iii) constant intensity ($k \in [0, 0.5]$, indicating no significant change).

Subsequently, varying concentrations of target oligonucleotides (ranging from 0.1 nM to 100 nM) are introduced into the microfluidic chamber containing the nanowire sensors. The fluorescence intensity from the nanowires is monitored over time using time-lapse fluorescence microscopy.

The results, summarized in Figure 6.10, show a clear concentration-dependent increase in the percentage of nanowires exhibiting rising fluorescence intensity upon exposure to target oligonucleotides (Figure 6.10b). In contrast, control experiments with scrambled oligonucleotides show minimal changes in fluorescence intensity (Figure 6.10 c), confirming the specificity of the molecular beacons. The sum of linear coefficients for nanowires with increasing intensity also displays a clear dependence on target concentration (Figure 6.10 d).

The minimum detectable concentration achieved in this setup is 0.1 nM, demonstrating the potential of nanowire-based biosensing combined with molecular beacons for sensitive and specific oligonucleotide detection. This approach holds strong promise for applications in genetic diagnostics and molecular biology research. While lower detection limits have been attained using other methods, the present work serves as a proof of concept, showcasing the potential of nanowire-based biosensing for dynamic molecular detection assays.

6.3.2 SLB formation on nanowires (Paper IV)

The lightguiding properties of semiconductor nanowires not only enhance the limits of optical biosensing, but also provide a platform to study biological processes at nanoscale. Nanowires provide a high surface-to-volume ratio and unique topographical features that can influence the behavior of biological membranes.

This study compares supported lipid bilayer (SLB) formation kinetics from POPC lipid vesicles on silica-coated vertically oriented silicon nanowires (NWs, radius of curvature $\sim$60 nm) versus planar silica surfaces, using time-resolved fluorescence microscopy with single-molecule sensitivity enabled by NW lightguiding. By observing the propagation of

the SLB front over time, we quantify the formation kinetics on both nanowire and planar surfaces. The results show that SLB formation on nanowires is significantly, around 3 times, faster than on planar substrates (4.6 ± 0.8 μm/s vs. 1.4 ± 0.3 μm/s). This is attributed to lower energy penalty for vesicle deformation and rupture on the curved nanowire surfaces, facilitating quicker bilayer spreading.

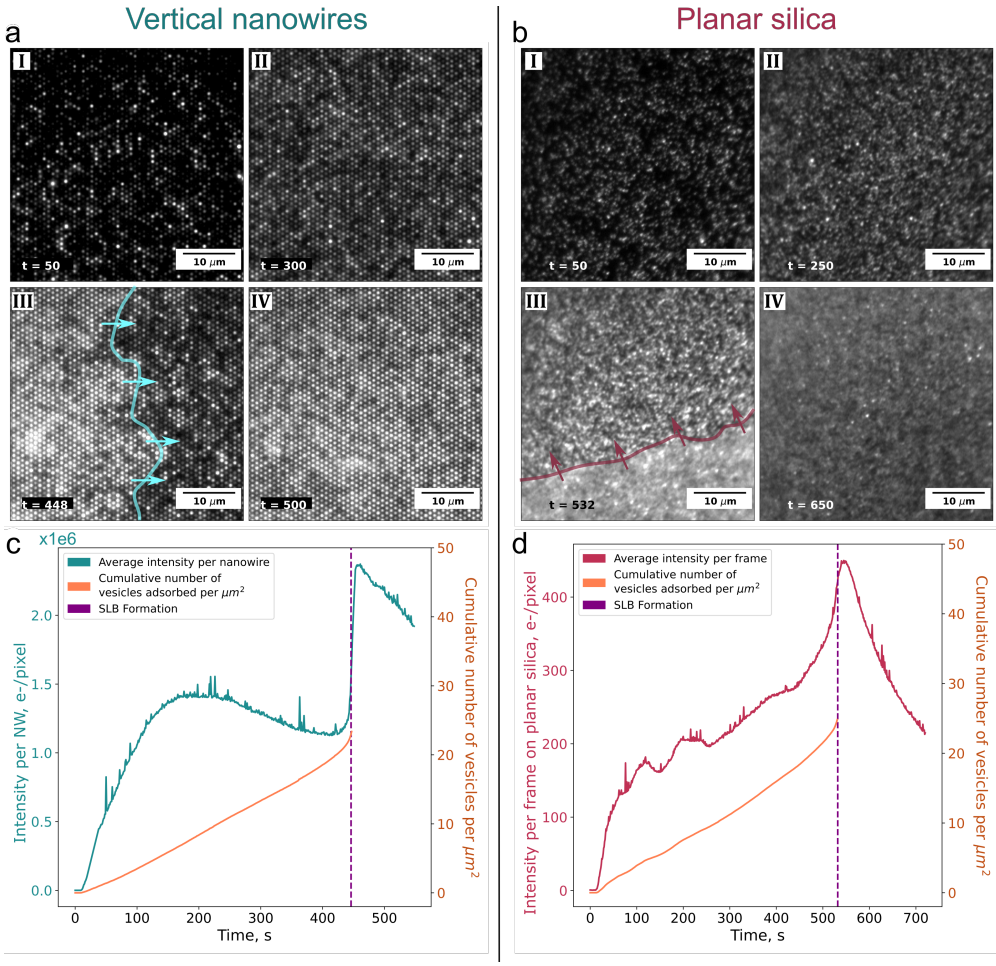

Figure 6.11: Supported lipid bilayer formation on nanowires and planar surfaces. (a) Sequential epifluorescence images (I–IV) show key stages of SLB formation on nanowire tips, and (b) corresponding TIRF micrographs from planar silica, recorded during continuous addition of vesicles containing 1% fluorescent lipid. Micrograph III in both sets mark the onset of SLB formation, and is at different time points. (c, d) The cumulative number of adsorbed vesicles per µm² (orange) is plotted over time up to SLB initiation, based on counts of newly appearing vesicles between frames. The plots also show background-corrected mean intensity per bright nanowire (turquoise) in (c) and per frame on planar silica (red) in (d).

We suggest that early local SLB patch formation precedes global SLB onset on NWs, unlike planar surfaces where patches emerge stochastically near critical coverage (∼20–30

vesicles/μm^2) (Figure 6.11 c-d). NW geometry promotes vesicle deformation and rupture at concave bases (increased contact area), forming mobile patches with fluctuating fluorescence from diffusing dye-labeled lipids, as evidenced by stepwise intensity changes and reduced photobleaching rates pre-SLB. Another significant difference is the intensities observed during SLB formation, with NWs showing higher fluorescence intensities for the same imaging conditions. Fluorescence recovery after photobleaching (FRAP), confirms fluidity of SLBs on both NWs and planar glass, proving that NW curvature does not hinder lipid mobility post-formation.

In this study, we used fluorescently labeled lipids to visualize SLB formation dynamics and extract quantitative kinetic parameters. The successful formation of functional SLBs on nanowires opens avenues for investigating membrane-associated processes, such as protein-lipid interactions and membrane mechanics, in a controlled nanoscale environment. Combined with the enhanced fluorescence from NWs and the possibility for off-plane localization (Paper V), this platform holds a promise for studying single-molecule dynamics in biomembranes with high spatial and possible axial resolution.

Chapter 7

Outlook and future perspectives

So comes snow after fire,
and even dragons have their endings

J.R.R. Tolkien, The Hobbit

This thesis work started amidst the COVID-19 pandemic, a time which highlighted again the critical importance of rapid, reliable biosensing technologies. While the thesis work ends here, the journey of developing new biosensing platforms continue. I end in hope that the work presented here contributes a small step towards that goal. This chapter provides an outlook on some direct extensions of the work presented in this thesis, as well as some broader perspectives on the field of nanowire-based biosensing.

This thesis presented advancements in nanowire-based optical biosensing through three interconnected contributions: the development of computational tools that push the limits of detection, the exploration of polymer-embedded nanowires as a scalable and cost-effective sensing platform, and the demonstration of their suitability for real-time biosensing and direct observation of dynamic biological processes.

While the computational tools developed here improve detection sensitivity and accuracy, they also highlight limitations from surface chemistry and non-specific binding. This thesis demonstrated that computational methods can effectively separate nanowire signals from substrate background, but with substrate-grown or etched nanowires, identical surface chemistry on both leads to uniform non-specific binding that complicates signal isolation. Distinct surface treatments on nanowires versus substrates could enhance assay performance. Polymer-embedded nanowires make this particularly feasible since the polymer matrix inherently contrasts the semiconductor nanowires. [184, 185] Recent protein design advances [186] enable proteins or peptides that target nanowires via semiconductor properties [187] or geometry (e.g., curvature-dependent affinity) [188], offer an exciting direction to achieve selective functionalization. Selective surface chemistry combined with computational tools could overcome the specificity limitations, enabling detection of lower analyte concentrations.

The successful formation of supported lipid bilayers (SLBs) on nanowires not only provides a platform to study curvature-dependent membrane formation and related biological processes but may also mitigate non-specific binding. A complete SLB can passivate the surface, reducing background noise and establishing a stable, low-signal baseline. Specific binding events, such as diffusion of labeled DNA or proteins within the bilayer, can then be tracked with clear spatial and temporal contrast. This time-resolved capability enables precise characterization of binding kinetics, molecular diffusion, and reaction-diffusion processes occurring at the nanowire surface.

Scalable and cost-effective fabrication of nanowire platforms is an essential step towards real-world applications. The polymer-embedded nanowires holds a promise in this regard, but further optimization is required. These optimizations include improving diameter and length uniformity, refining oxide and polymer encapsulation to balance mechanical stability with optimal optical outcoupling, and integrating microfluidic structures for controlled sample handling over large areas. The ability to invert the sensing geometry and image through an optically transparent, thin polymer layer rather than through the absorbing and scattering sample matrix is particularly promising for applications in whole blood and other turbid fluids, and could be further refined by co-designing nanowire orientation, polymer refractive index, and illumination scheme to minimize scattering and aberrations.

For proteins, sandwich assays analogous to enzyme-linked immunosorbent assay (ELISA) could be implemented to perform nanowire-based detection in complex biological fluids.

Such assays, capturing unlabeled target protein with immobilized antibodies, rely on fluorescent secondary probes to generate a signal. Therefore, proteins present in low concentrations in human biofluids, such as cytokines (e.g., IL-6, TNF-alpha), sepsis marker procalcitonin, growth factor IGF-1, or hormones like cholesterol, testosterone, and estrogen, could be targeted. This would support continuous profiling in undiluted biofluids for early diagnosis, therapeutic monitoring, and personalized health tracking.

Computational advancements could further this vision, transforming laboratory demonstrations into applied systems. The step-wise single emitter detection and off-plane localization methods developed here could easily be extended to fully automated pipelines. Neural networks could be trained to directly perform localization and tracking of fluoroscently labeled molecules, including models informed by physics-based simulations and molecular dynamics. Bayesian or evidential deep learning architectures would deliver per-event uncertainty and confidence scores, providing robust error quantification essential for clinical diagnostics where false results have serious consequences. However, conventional image filtering and localization algorithms still remain valuable due to their lower computational requirements and greater interpretability. Therefore, hybrid approaches combining informed classical models with machine learning, semi-supervised learning, or physics informed neural networks could balance accuracy and efficiency.

For a complete biosensing system, integrating nanowire platforms with compact, low cost optical hardware is essential. Combined with microfluidics systems, the simplest advance would be a compact tabletop microscope, exploiting the inherent simplicity of lightguiding nanowires: without the need of elaborate TIRF or high numerical aperture objectives and sophisticated microscopes. Pushing toward true portability, on-chip detection would be the ultimate final step. Placing nanowires directly atop CMOS pixel arrays, could enable near-field capture of signal and sub-micron resolution without external optical systems. Excitation-free bioluminescent or chemiluminescent reporters would further simplify design, harnessing prolonged emission for single-molecule sensitivity without light sources.

While during my short PhD lifetime I could only explore a fraction of these exciting directions, I hope that the work presented here provides a stepping stone. Through improved surface chemistry, optimized fabrication, and the fusion of computational insight with hardware miniaturization, nanowire biosensing may ultimately progress from laboratory demonstrations to practical tools in the hands of clinicians and users who are in need of rapid, sensitive detection.

References

[1] A. P. Turner, "Biosensors: sense and sensibility," *Chemical Society Reviews*, vol. 42, pp. 3184–3196, 3 2013.

[2] N. Bhalla, P. Jolly, N. Formisano, and P. Estrela, "Introduction to biosensors," *Essays in Biochemistry*, vol. 60, p. 1, 6 2016.

[3] T. N. L. Pham, S. H. Nguyen, and M. T. Tran, "A comprehensive review of transduction methods of lectin-based biosensors in biomedical applications," *Heliyon*, vol. 10, p. e38371, 10 2024.

[4] J. Qin, W. Wang, L. Gao, and S. Q. Yao, "Emerging biosensing and transducing techniques for potential applications in point-of-care diagnostics," *Chemical Science*, vol. 13, pp. 2857–2876, 3 2022.

[5] P. Damborský, J. Švitel, and J. Katrlík, "Optical biosensors," *Essays in Biochemistry*, vol. 60, p. 91, 6 2016.

[6] S. Mostufa, B. Rezaei, S. Ciannella, P. Yari, J. Gómez-Pastora, R. He, and K. Wu, "Advancements and perspectives in optical biosensors," *ACS Omega*, vol. 9, pp. 24181–24202, 6 2024.

[7] B. Kaur, S. Kumar, J. Nedoma, R. Martinek, and C. Marques, "Advancements in optical biosensing techniques: From fundamentals to future prospects," *APL Photonics*, vol. 9, 9 2024.

[8] Z. Geng, X. Zhang, Z. Fan, X. Lv, Y. Su, and H. Chen, "Recent progress in optical biosensors based on smartphone platforms," *Sensors (Basel, Switzerland)*, vol. 17, p. 2449, 11 2017.

[9] S. Akgönüllü and A. Denizli, "Recent advances in optical biosensing approaches for biomarkers detection," *Biosensors and Bioelectronics: X*, vol. 12, p. 100269, 12 2022.

[10] M. Strianese, M. Staiano, G. Ruggiero, T. Labella, C. Pellecchia, and S. D'Auria, "Fluorescence-based biosensors," *Methods in Molecular Biology*, vol. 875, pp. 193–216, 2012.

[11] P. Nath, K. R. Mahtaba, and A. Ray, "Fluorescence-based portable assays for detection of biological and chemical analytes," *Sensors 2023, Vol. 23, Page 5053*, vol. 23, p. 5053, 5 2023.

[12] C. I. Justino, A. C. Duarte, and T. A. Rocha-Santos, "Critical overview on the application of sensors and biosensors for clinical analysis," *Trends in Analytical Chemistry*, vol. 85, p. 36, 12 2016.

[13] S. Dey, M. Dolci, and P. Zijlstra, "Single-molecule optical biosensing: Recent advances and future challenges," *ACS Physical Chemistry Au*, vol. 3, pp. 143–156, 3 2023.

[14] N. Akkilic, S. Geschwindner, and F. Höök, "Single-molecule biosensors: Recent advances and applications," *Biosensors and Bioelectronics*, vol. 151, p. 111944, 3 2020.

[15] M. Lelek, M. T. Gyparaki, G. Beliu, F. Schueder, J. Griffié, S. Manley, R. Jungmann, M. Sauer, M. Lakadamyali, and C. Zimmer, "Single-molecule localization microscopy," *Nature Reviews Methods Primers*, vol. 1, p. 39, June 3 2021.

[16] G. H. Patterson, "Fluorescence microscopy below the diffraction limit," *Seminars in Cell & Developmental Biology*, vol. 20, pp. 886–893, 10 2009.

[17] L. Mezache and C. Leterrier, "Advancing super-resolution microscopy: Recent innovations in commercial instruments," *Microscopy and Microanalysis*, vol. 31, 3 2025.

[18] H. Maib, P. Adarska, R. Hunton, J. H. Vines, D. Strutt, F. Bottanelli, and D. H. Murray, "Recombinant biosensors for multiplex and super-resolution imaging of phosphoinositides," *Journal of Cell Biology*, vol. 223, 6 2024.

[19] F. Edorna, F. D. Choque, G. Ferrari, L. A. Masullo, P. Zdańkowski, G. P. Acuna, P. Tinnefeld, A. M. Szalai, L. F. Lopez, A. Zelcer, and F. D. Stefani, "Open-source sub-nanometer stabilization system for super-resolution fluorescence microscopy," *Light: Science & Applications 2025 14:1*, vol. 14, pp. 385–, 11 2025.

[20] D. Verardo, F. W. Lindberg, N. Anttu, C. S. Niman, M. Lard, A. P. Dabkowska, T. Nylander, A. Månsson, C. N. Prinz, and H. Linke, "Nanowires for biosensing: Lightguiding of fluorescence as a function of diameter and wavelength," *Nano Letters*, vol. 18, pp. 4796–4802, 8 2018.

[21] R. Frederiksen, G. Tutuncuoglu, F. Matteini, K. L. Martinez, A. Fontcuberta, and E. Alarcon-Llado, "Visual understanding of light absorption and waveguiding in standing nanowires with 3d fluorescence confocal microscopy," *ACS Photonics*, vol. 4, pp. 2235–2241, 9 2017.

[22] J. Valderas-Gutiérrez, R. Davtyan, S. Sivakumar, N. Anttu, Y. Li, P. Flatt, J. Y. Shin, C. N. Prinz, F. Höök, T. Fioretos, M. H. Magnusson, and H. Linke, "Enhanced optical biosensing by aerotaxy ga(as)p nanowire platforms suitable for scalable production," *ACS Applied Nano Materials*, vol. 5, pp. 9063–9071, 7 2022.

[23] N. Anttu, H. Mäntynen, T. Sadi, A. Matikainen, J. Turunen, and H. Lipsanen, "Comparison of absorption simulation in semiconductor nanowire and nanocone arrays with the fourier modal method, the finite element method, and the finite-difference time-domain method," *Nano Express*, vol. 1, 12 2020.

[24] D. Verardo, L. Liljedahl, C. Richter, B. Agnarsson, U. Axelsson, C. N. Prinz, F. Höök, C. A. Borrebaeck, and H. Linke, "Fluorescence signal enhancement in antibody microarrays using lightguiding nanowires," *Nanomaterials*, vol. 11, pp. 1–11, 2021.

[25] B. Du, C. Tang, D. Zhao, H. Zhang, D. Yu, M. Yu, K. C. Balram, H. Gersen, B. Yang, W. Cao, C. Gu, F. Besenbacher, J. Li, and Y. Sun, "Diameter-optimized high-order waveguide nanorods for fluorescence enhancement applied in ultrasensitive bioassays," *Nanoscale*, vol. 11, pp. 14322–14329, 8 2019.

[26] R. S. Frederiksen, E. Alarcon-Llado, P. Krogstrup, L. Bojarskaite, N. Buch-Månson, J. Bolinsson, J. Nygård, A. FontcubertaMorral, and K. L. Martinez, "Nanowire-aperture probe: Local enhanced fluorescence detection for the investigation of live cells at the nanoscale," *ACS Photonics*, vol. 3, pp. 1208–1216, 7 2016.

[27] I. N. Unksov, N. Anttu, D. Verardo, F. Höök, C. N. Prinz, and H. Linke, "Fluorescence excitation enhancement by waveguiding nanowires," *Nanoscale Adv.*, vol. 5, pp. 1760–1766, 2023.

[28] N. Anttu, H. Mäntynen, A. Sorokina, J. Turunen, T. Sadi, and H. Lipsanen, "Applied electromagnetic optics simulations for nanophotonics," *Journal of Applied Physics*, vol. 129, p. 131102, April 2021.

[29] A. Sorokina, H. Lipsanen, and N. Anttu, "Designing outcoupling of light from nanostructured emitter in stratified medium with parasitic absorption," *Journal of Applied Physics*, vol. 131, 6 2022.

[30] N. Chenouard, I. Smal, F. D. Chaumont, M. Maška, I. F. Sbalzarini, Y. Gong, J. Cardinale, C. Carthel, S. Coraluppi, M. Winter, A. R. Cohen, W. J. Godinez, K. Rohr, Y. Kalaidzidis, L. Liang, J. Duncan, H. Shen, Y. Xu, K. E. Magnusson, J. Jaldén, H. M. Blau, P. Paul-Gilloteaux, P. Roudot, C. Kervrann, F. Waharte, J. Y. Tinevez, S. L. Shorte, J. Willemse, K. Celler, G. P. V. Wezel, H. W. Dan, Y. S. Tsai, C. O. D. Solórzano, J. C. Olivo-Marin, and E. Meijering, "Objective comparison of particle tracking methods," *Nature Methods*, vol. 11, pp. 281–289, 3 2014.

[31] M. Lindén, V. Ćurić, A. Boucharin, D. Fange, and J. Elf, "Simulated single molecule microscopy with smeagol," *Bioinformatics*, vol. 32, pp. 2394–2395, 8 2016.

[32] S. C. Stein and J. Thiart, "Trackntrace: A simple and extendable open-source framework for developing single-molecule localization and tracking algorithms," *Scientific Reports 2016 6:1*, vol. 6, pp. 1–7, 11 2016.

[33] D. Sage, H. Kirshner, T. Pengo, N. Stuurman, J. Min, S. Manley, and M. Unser, "Quantitative evaluation of software packages for single-molecule localization microscopy," *Nature Methods*, vol. 12, pp. 717–724, 2015.

[34] D. Sage, T. A. Pham, H. Babcock, T. Lukes, T. Pengo, J. Chao, R. Velmurugan, A. Herbert, A. Agrawal, S. Colabrese, A. Wheeler, A. Archetti, B. Rieger, R. Ober, G. M. Hagen, J. B. Sibarita, J. Ries, R. Henriques, M. Unser, and S. Holden, "Super-resolution fight club: assessment of 2D and 3D single-molecule localization microscopy software," *Nature Methods*, vol. 16, no. 5, pp. 387–395, 2019.

[35] A. J. Wollman, R. Nudd, E. G. Hedlund, and M. C. Leake, "From animaculum to single molecules: 300 years of the light microscope," *Open Biology*, vol. 5, 4 2015.

[36] E. Abbe, "Beiträge zur theorie des mikroskops und der mikroskopischen wahrnehmung: I. die construction von mikroskopen auf grund der theorie," *Archiv für mikroskopische Anatomie*, vol. 9, pp. 413–418, 12 1873.

[37] S. W. Hell, "Far-field optical nanoscopy," *Science*, vol. 316, pp. 1153–1158, 5 2007.

[38] J. W. Lichtman and J. A. Conchello, "Fluorescence microscopy," *Nature Methods 2005 2:12*, vol. 2, pp. 910–919, 11 2005.

[39] J. R. Lakowicz, *Principles of fluorescence spectroscopy*. Springer, 3rd ed., 2010.

[40] M. Zimmer, "Green fluorescent protein (gfp): Applications, structure, and related photophysical behavior," *Chemical Reviews*, vol. 102, pp. 759–781, 3 2002.

[41] M. Zhang, M. Li, W. Zhang, Y. Han, and Y. H. Zhang, "Simple and efficient delivery of cell-impermeable organic fluorescent probes into live cells for live-cell superresolution imaging," *Light: Science and Applications*, vol. 8, pp. 1–11, 12 2019.

[42] Y. Khan, S. Hwang, R. Braveenth, Y. H. Jung, B. Walker, and J. H. Kwon, "Synthesis of fluorescent organic nano-dots and their application as efficient color conversion layers," *Nature Communications*, vol. 13, pp. 1–9, 12 2022.

[43] S. Pandey and D. Bodas, "High-quality quantum dots for multiplexed bioimaging: A critical review," *Advances in Colloid and Interface Science*, vol. 278, p. 102137, 4 2020.

[44] A. Jabłoństski, "Efficiency of anti-stokes fluorescence in dyes," *Nature 1933 131:3319*, vol. 131, pp. 839–840, 1933.

[45] T. Scientific, "Fluorescence spectraviewer."

[46] D. J. Webb and C. M. Brown, "Epi-fluorescence microscopy," *Methods in molecular biology (Clifton, N.J.)*, vol. 931, p. 29, 2013.

[47] C. A. Combs, "Fluorescence microscopy: A concise guide to current imaging methods," *Current protocols in neuroscience / editorial board, Jacqueline N. Crawley ... [et al.]*, vol. 0 2, p. Unit2.1, 2010.

[48] M. J. Sanderson, I. Smith, I. Parker, and M. D. Bootman, "Fluorescence microscopy," *Cold Spring Harbor protocols*, vol. 2014, p. pdb.top071795, 10 2014.

[49] M. L. Martin-Fernandez, C. J. Tynan, and S. E. Webb, "A 'pocket guide' to total internal reflection fluorescence," *Journal of Microscopy*, vol. 252, pp. 16–22, 2013.

[50] D. Toomre and D. J. Manstein, "Lighting up the cell surface with evanescent wave microscopy," *Trends in Cell Biology*, vol. 11, p. 298, July 2001.

[51] K. N. Fish, "Total internal reflection fluorescence (tirf) microscopy," *Curr Protoc Cytom*, vol. Chapter 12, p. Unit12.18, Oct 2009.

[52] C. Y. Hsu, A. M. Rheima, Z. sabri Abbas, M. U. Faryad, M. M. Kadhim, U. S. Altimari, A. H. Dawood, A. dhari jawad al bayati, Z. T. Abed, R. S. Radhi, A. S. Jaber, S. K. Hachim, F. K. Ali, Z. H. Mahmoud, G. B. pour, and E. Kianfar, "Nanowires properties and applications: A review study," *South African Journal of Chemical Engineering*, vol. 46, pp. 286–311, 10 2023.

[53] L. N. Quan, J. Kang, C. Z. Ning, P. D. Yang, J. Deng, Y. Su, D. Liu, B. Liu, and C. Liu, "Introduction: 1d nanomaterials/nanowires," *Chemical Reviews*, vol. 119, pp. 8955–8957, 8 2019.

[54] P. Krogstrup, H. I. Jorgensen, M. Heiss, O. Demichel, J. V. Holm, M. Aagesen, J. Nygard, I. A. Fontcuberta, . S. Sandhu, Z. Yu, S. Fan, . G. Grzela, R. Paniagua-Domínguez, T. Barten, D. V. Dam, J. A. Sánchez-Gil, and J. G. Rivas, "Review on photonic properties of nanowires for photovoltaics," *Optics Express, Vol. 24, Issue 15, pp. 17345-17358*, vol. 24, pp. 17345–17358, 7 2016.

[55] N. S. Ramgir, Y. Yang, and M. Zacharias, "Nanowire-based sensors," *Small*, vol. 6, pp. 1705–1722, 8 2010.

[56] T. A. Crowley, K. J. Ziegler, D. M. Lyons, D. Erts, H. Olin, M. A. Morris, and J. D. Holmes, "Synthesis of metal and metal oxide nanowire and nanotube arrays within a mesoporous silica template," *Chemistry of Materials*, vol. 15, pp. 3518–3522, 9 2003.

[57] X. Duan, C. M. Lieber, C. M. Lieber, X. Duan, J. Hu, J.-L. Huang, L. Venkataraman, J. Wang, Q. Wei, M. Frongillo, and Y. Lu, "General synthesis of compound semiconductor nanowires," *Adv. Mater*, vol. 12, 2000.

[58] D. Kong, J. C. Randel, H. Peng, J. J. Cha, S. Meister, K. Lai, Y. Chen, Z. X. Shen, H. C. Manoharan, and Y. Cui, "Topological insulator nanowires and nanoribbons," *Nano Letters*, vol. 10, pp. 329–333, 1 2009.

[59] A. I. Hochbaum and P. Yang, "Semiconductor nanowires for energy conversion," *Chemical Reviews*, vol. 110, pp. 527–546, 1 2009.

[60] X. Duan, J. Wang, and C. M. Lieber, "Synthesis and optical properties of gallium arsenide nanowires," *Applied Physics Letters*, vol. 76, pp. 1116–1118, 2 2000.

[61] S. Assali, I. Zardo, S. Plissard, D. Kriegner, M. A. Verheijen, G. Bauer, A. Meijerink, A. Belabbes, F. Bechstedt, J. E. Haverkort, and E. P. Bakkers, "Direct band gap wurtzite gallium phosphide nanowires," *Nano Letters*, vol. 13, pp. 1559–1563, 4 2013.

[62] V. V. Fedorov, A. Bolshakov, O. Sergaeva, V. Neplokh, D. Markina, S. Bruyere, G. Saerens, M. I. Petrov, R. Grange, M. Timofeeva, S. V. Makarov, and I. S. Mukhin, "Gallium phosphide nanowires in a free-standing, flexible, and semitransparent membrane for large-scale infrared-to-visible light conversion," *ACS Nano*, vol. 14, pp. 10624–10632, 8 2020.

[63] J.-N. Chazalviel, P. Allongue, A. C. Gouget-Laemmel, C. H. de Villeneuve, A. Moraillon, and F. Ozanam, "Covalent functionalizations of silicon surfaces and their application to biosensors," *Science of Advanced Materials*, vol. 3, pp. 332–353, June 2011.

[64] R. Voicu, R. Boukherroub, V. Bartzoka, T. Ward, J. T. C. Wojtyk, and D. D. M. Wayner, "Formation, characterization, and chemistry of undecanoic acid-terminated silicon surfaces: Patterning and immobilization of dna," *Langmuir*, vol. 20, no. 26, pp. 11713–11720, 2004. PMID: 15595802.

[65] A. W. Snyder and D. J. Mitchell, "Leaky mode analysis of circular optical waveguides," *Opto-electronics*, vol. 6, pp. 287–296, 7 1974.

[66] H. Kogelnik, "Theory of optical waveguides," pp. 7–88, 1988.

[67] N. Anttu, "Fluorophore signal detection and imaging enhancement in high refractive index nanowire biosensors," *Nano Express*, vol. 6, no. 1, p. 015005, 2025.

[68] N. Anttu, "Modifying the emission of light from a semiconductor nanowire array," *Journal of Applied Physics*, vol. 120, p. 043108, July 29 2016.

[69] A. E. Krasnok, A. P. Slobozhanyuk, C. R. Simovski, S. A. Tretyakov, A. N. Poddubny, A. E. Miroshnichenko, Y. S. Kivshar, and P. A. Belov, "An antenna model for the purcell effect," *Scientific Reports 2015 5:1*, vol. 5, pp. 12956–, 8 2015.

[70] K. Shoorideh and C. O. Chui, "On the origin of enhanced sensitivity in nanoscale fet-based biosensors," *Proceedings of the National Academy of Sciences of the United States of America*, vol. 111, pp. 5111–5116, 2014.

[71] A. K. Y. Dafhalla, T. S. Dhahi, A. W. Al-Mufti, S. A. Saad, A. S. Alqahtani, M. A. H. Al-nuaimi, M. E. Elobaid, T. Adam, and S. C. Gopinath, "Nanogap nanowires and its applications in biosensing," *Sensing and Bio-Sensing Research*, vol. 44, p. 100638, 6 2024.

[72] S. K. Bhardwaj, N. Bhardwaj, V. Kumar, D. Bhatt, A. Azzouz, J. Bhaumik, K. H. Kim, and A. Deep, "Recent progress in nanomaterial-based sensing of airborne viral and bacterial pathogens," *Environment International*, vol. 146, p. 106183, 1 2021.

[73] P. Ambhorkar, Z. Wang, H. Ko, S. Lee, K. I. Koo, K. Kim, and D. I. D. Cho, "Nanowire-based biosensors: From growth to applications," *Micromachines*, vol. 9, p. 679, 12 2018.

[74] R. Yan, D. Gargas, and P. Yang, "Nanowire photonics," *Nature Photonics*, vol. 3, pp. 569–576, 2009.

[75] P. C. McIntyre and A. F. i Morral, "Semiconductor nanowires: to grow or not to grow?," *Materials Today Nano*, vol. 9, p. 100058, 3 2020.

[76] E. D. Leshchenko and N. V. Sibirev, "Recent advances in the growth and compositional modelling of iii–v nanowire heterostructures," *Nanomaterials 2024, Vol. 14, Page 1816*, vol. 14, p. 1816, 11 2024.

[77] P. M. Coulon, B. Damilano, B. Alloing, P. Chausse, S. Walde, J. Enslin, R. Armstrong, S. Vézian, S. Hagedorn, T. Wernicke, J. Massies, J. Zúñiga□Pérez, M. Weyers, M. Kneissl, and P. A. Shields, "Displacement talbot lithography for nanoengineering of iii-nitride materials," *Microsystems and Nanoengineering*, vol. 5, pp. 1–12, 12 2019.

[78] F. Clube, C. Dais, and H. H. Solak, "Displacement talbot lithography: a new method for high-resolution patterning of large areas," *Optics Express, Vol. 19, Issue 11, pp. 10686-10691*, vol. 19, pp. 10686–10691, 5 2011.

[79] K. Patorski, "The self-imaging phenomenon and its applications," *Progress in Optics*, vol. 27, pp. 1–108, 1 1989.

[80] A. Berg, S. Lehmann, N. Vainorius, A. Gustafsson, M. E. Pistol, L. R. Wallenberg, L. Samuelson, and M. T. Borgström, "Growth and characterization of wurtzite gap nanowires with control over axial and radial growth by use of hcl in-situ etching," *Journal of Crystal Growth*, vol. 386, pp. 47–51, 1 2014.

[81] R. S. Wagner and W. C. Ellis, "Vapor-liquid-solid mechanism of single crystal growth," *Applied Physics Letters*, vol. 4, pp. 89–90, 3 1964.

[82] K. Hiruma, H. Murakoshi, M. Yazawa, and T. Katsuyama, "Self-organized growth of gaasinas heterostructure nanocylinders by organometallic vapor phase epitaxy," *Journal of Crystal Growth*, vol. 163, pp. 226–231, 6 1996.

[83] D. Alcer, *Single Junction and Tandem Junction Nanowire Solar Cells*. Doctoral thesis (compilation), Lund University, Faculty of Engineering, LTH, Department of Physics, 2024.

[84] K. Adham, *Charge Carrier Diffusion Induced Light Emitting Diodes*. Doctoral thesis (compilation), Lund University, Faculty of Engineering, LTH, Department of Physics, 2024.

[85] R. W. Johnson, A. Hultqvist, and S. F. Bent, "A brief review of atomic layer deposition: from fundamentals to applications," *Materials Today*, vol. 17, pp. 236–246, 6 2014.

[86] M. Heurlin, D. Lindgren, K. Deppert, L. Samuelson, M. H. Magnusson, M. L. Ek, and R. Wallenberg, "Continuous gas-phase synthesis of nanowires with tunable properties," *Nature*, vol. 492, pp. 90–94, 12 2012.

[87] W. Metaferia, A. R. Persson, K. Mergenthaler, F. Yang, W. Zhang, A. Yartsev, R. Wallenberg, M. E. Pistol, K. Deppert, L. Samuelson, and M. H. Magnusson, "Gaasp nanowires grown by aerotaxy," *Nano letters*, vol. 16, pp. 5701–5707, 9 2016.

[88] S. Sivakumar, *Understanding and Optimization of III-V Nanowire Growth in Aerotaxy*. Doctoral thesis (compilation), Lund University, Faculty of Engineering, LTH, Department of Physics, 2021.

[89] E. Welser, W. Guter, A. Wekkeli, and F. Dimroth, "Memory effect of ge in iii–v semiconductors," *Journal of Crystal Growth*, vol. 310, pp. 4799–4802, 11 2008.

[90] U. Naseem, J. Borgström, J. Castillo-León, and P. Viklund, "Methods of capturing and aligning an assembly of nanowires," 2017. European Patent Application, filed 2015-04-28, priority 2014-04-29.

[91] V. T. H. Nguyen, C. Silvestre, P. Shi, R. Cork, F. Jensen, J. Hubner, K. Ma, P. Leussink, M. de Boer, and H. Jansen, "The core sequence: A nanoscale

fluorocarbon-free silicon plasma etch process based on sf6/o2 cycles with excellent 3d profile control at room temperature," *ECS Journal of Solid State Science and Technology*, vol. 9, p. 024002, 1 2020.

[92] M. Ramesh, R. Janani, C. Deepa, and L. Rajeshkumar, "Nanotechnology-enabled biosensors: A review of fundamentals, design principles, materials, and applications," *Biosensors*, vol. 13, p. 40, 1 2022.

[93] N. M. Green, "Avidin," *Advances in Protein Chemistry*, vol. 29, pp. 85–133, 1 1975.

[94] A. Jain and K. Cheng, "The principles and applications of avidin-based nanoparticles in drug delivery and diagnosis," *Journal of controlled release : official journal of the Controlled Release Society*, vol. 245, p. 27, 1 2016.

[95] F. Tausig and F. J. Wolf, "Streptavidin—a substance with avidin-like properties produced by microorganisms," *Biochemical and Biophysical Research Communications*, vol. 14, pp. 205–209, 1 1964.

[96] A. Jain, A. Barve, Z. Zhao, W. Jin, and K. Cheng, "Comparison of avidin, neutravidin, and streptavidin as nanocarriers for efficient sirna delivery," *Molecular pharmaceutics*, vol. 14, p. 1517, 5 2017.

[97] T. T. Nguyen, K. L. Sly, and J. C. Conboy, "Comparison of the energetics of avidin, streptavidin, neutravidin, and anti-biotin antibody binding to biotinylated lipid bilayer examined by second-harmonic generation," *Analytical Chemistry*, vol. 84, pp. 201–208, 1 2011.

[98] C. M. Dundas, D. Demonte, and S. Park, "Streptavidin-biotin technology: Improvements and innovations in chemical and biological applications," *Applied Microbiology and Biotechnology*, vol. 97, pp. 9343–9353, 11 2013.

[99] M. Wilchek, "My life with affinity," *Protein Science : A Publication of the Protein Society*, vol. 13, p. 3066, 11 2004.

[100] Y. L. Jeyachandran, J. A. Mielczarski, E. Mielczarski, and B. Rai, "Efficiency of blocking of non-specific interaction of different proteins by bsa adsorbed on hydrophobic and hydrophilic surfaces," *Journal of Colloid and Interface Science*, vol. 341, pp. 136–142, 1 2010.

[101] K. Kubiak-Ossowska, B. Jachimska, and P. A. Mulheran, "How negatively charged proteins adsorb to negatively charged surfaces: A molecular dynamics study of bsa adsorption on silica," *Journal of Physical Chemistry B*, vol. 120, pp. 10463–10468, 10 2016.

[102] J. E. Medina, N. C. Dracopoli, P. B. Bach, A. Lau, R. B. Scharpf, G. A. Meijer, C. L. Andersen, and V. E. Velculescu, "Cell-free dna approaches for cancer early detection and interception," *Journal for Immunotherapy of Cancer*, vol. 11, p. e006013, 9 2023.

[103] C. Rolfo and A. Russo, "Brave new world of cfdna-omics for early cancer detection," *Journal for ImmunoTherapy of Cancer*, vol. 11, p. 6309, 9 2023.

[104] D. C. Ferrier, M. P. Shaver, and P. J. Hands, "Micro- and nano-structure based oligonucleotide sensors," *Biosensors and Bioelectronics*, vol. 68, pp. 798–810, 6 2015.

[105] T. Gilboa, P. M. Garden, and L. Cohen, "Single-molecule analysis of nucleic acid biomarkers – a review," *Analytica Chimica Acta*, vol. 1115, pp. 61–85, 6 2020.

[106] Y. Tang, G. Qiao, E. Xu, Y. Xuan, M. Liao, and G. Yin, "Biomarkers for early diagnosis, prognosis, prediction, and recurrence monitoring of non-small cell lung cancer," *OncoTargets and therapy*, vol. 10, p. 4527, 9 2017.

[107] A. R. Shakoori, "Fluorescence in situ hybridization (fish) and its applications," *Chromosome Structure and Aberrations*, p. 343, 1 2017.

[108] S. Tyagi and F. R. Kramer, "Molecular beacons: Probes that fluoresce upon hybridization," *Nature Biotechnology 1996 14:3*, vol. 14, pp. 303–308, 1996.

[109] R. Monroy-Contreras and L. Vaca, "Molecular beacons: Powerful tools for imaging rna in living cells," *Journal of Nucleic Acids*, vol. 2011, p. 741723, 1 2011.

[110] C. J. Yang and W. Tan, *Molecular beacons*. Springer-Verlag Berlin Heidelberg, 1 2013.

[111] A. Tsourkas, M. A. Behlke, S. D. Rose, and G. Bao, "Hybridization kinetics and thermodynamics of molecular beacons," *Nucleic Acids Research*, vol. 31, p. 1319, 2 2003.

[112] G. Bonnet, S. Tyagi, A. Libchaber, and F. R. Kramer, "Thermodynamic basis of the enhanced specificity of structured dna probes," *Proceedings of the National Academy of Sciences of the United States of America*, vol. 96, p. 6171, 5 1999.

[113] Y. Gao, L. K. Wolf, and R. M. Georgiadis, "Secondary structure effects on dna hybridization kinetics: a solution versus surface comparison," *Nucleic Acids Research*, vol. 34, p. 3370, 2006.

[114] M. M. Sekar, W. Bloch, and P. M. S. John, "Comparative study of sequence-dependent hybridization kinetics in solution and on microspheres," *Nucleic Acids Research*, vol. 33, p. 366, 2005.

[115] A. Vainrub and B. M. Pettitt, "Surface electrostatic effects in oligonucleotide microarrays: Control and optimization of binding thermodynamics," *Biopolymers*, vol. 68, pp. 265–270, 2 2003.

[116] A. Halperin, A. Buhot, and E. B. Zhulina, "Brush effects on dna chips: Thermodynamics, kinetics, and design guidelines," *Biophysical Journal*, vol. 89, pp. 796–811, 8 2005.

[117] M. I. Glazer, J. A. Fidanza, G. H. McGall, M. O. Trulson, J. E. Forman, and C. W. Frank, "Kinetics of oligonucleotide hybridization to dna probe arrays on high-capacity porous silica substrates," *Biophysical Journal*, vol. 93, p. 1661, 2007.

[118] R. L. Stoermer, K. B. Cederquist, S. K. McFarland, M. Y. Sha, S. G. Penn, and C. D. Keating, "Coupling molecular beacons to barcoded metal nanowires for multiplexed, sealed chamber dna bioassays," *Journal of the American Chemical Society*, vol. 128, p. 16892, 12 2006.

[119] M. Z. Markarian and J. B. Schlenoff, "Effect of molecular crowding and ionic strength on the isothermal hybridization of oligonucleotides," *The journal of physical chemistry. B*, vol. 114, p. 10620, 8 2010.

[120] H. Kuhn, V. V. Demidov, J. M. Coull, M. J. Fiandaca, B. D. Gildea, and M. D. Frank-Kamenetskii, "Hybridization of dna and pna molecular beacons to single-stranded and double-stranded dna targets," *Journal of the American Chemical Society*, vol. 124, pp. 1097–1103, 2 2002.

[121] G. M. Cooper, *Cell Membranes*. Sunderland, MA: Sinauer Associates, 2 ed., 2000.

[122] B. Alberts, A. Johnson, J. Lewis, M. Raff, K. Roberts, and P. Walter, *The Lipid Bilayer*. New York: Garland Science, 4 ed., 2002.

[123] C. Paba, V. Dorigo, B. Senigagliesi, N. Tormena, P. Parisse, K. Voitchovsky, and L. Casalis, "Lipid bilayer fluidity and degree of order regulates small evs adsorption on model cell membrane," *Journal of Colloid and Interface Science*, vol. 652, pp. 1937–1943, 12 2023.

[124] C. Tribet and F. Vial, "Flexible macromolecules attached to lipid bilayers: impact on fluidity, curvature, permeability and stability of the membranes," *Soft Matter*, vol. 4, pp. 68–81, 12 2007.

[125] S. J. Singer and G. L. Nicolson, "The fluid mosaic model of the structure of cell membranes," *Science*, vol. 175, pp. 720–731, 2 1972.

[126] K. Simons and E. Ikonen, "Functional rafts in cell membranes," *Nature 1997 387:6633*, vol. 387, pp. 569–572, 6 1997.

[127] L. K. Tamm and H. M. McConnell, "Supported phospholipid bilayers," *Biophysical Journal*, vol. 47, p. 105, 1985.

[128] L. K. Tamm, J. Crane, and V. Kiessling, "Membrane fusion: a structural perspective on the interplay of lipids and proteins," *Current Opinion in Structural Biology*, vol. 13, pp. 453–466, 8 2003.

[129] R. P. Richter, R. Bérat, and A. R. Brisson, "Formation of solid-supported lipid bilayers: An integrated view," *Langmuir*, vol. 22, pp. 3497–3505, 4 2006.

[130] I. Langmuir, "The constitution and fundamental properties of solids and liquids. ii. liquids.1," *Journal of the American Chemical Society*, vol. 39, pp. 1848–1906, 9 2002.

[131] K. B. B. Vol, E. K. Rideal, and P. R. Soc, "Films built by depositing successive monomolecular layers on a solid surface," *Journal of the American Chemical Society*, vol. 57, pp. 1007–1022, 6 2002.

[132] J. Kurniawan, J. F. V. D. Souza, A. T. Dang, G. Y. Liu, and T. L. Kuhl, "Preparation and characterization of solid-supported lipid bilayers formed by langmuir–blodgett deposition: A tutorial," *Langmuir*, vol. 34, pp. 15622–15639, 12 2018.

[133] I. Reviakine and A. Brisson, "Formation of supported phospholipid bilayers from unilamellar vesicles investigated by atomic force microscopy," *Langmuir*, vol. 16, pp. 1806–1815, 2 2000.

[134] H. T. McMahon and J. L. Gallop, "Membrane curvature and mechanisms of dynamic cell membrane remodelling," *Nature*, vol. 438, pp. 590–596, 12 2005.

[135] M. Simunovic, G. A. Voth, A. Callan-Jones, and P. Bassereau, "When physics takes over: Bar proteins and membrane curvature," *Trends in cell biology*, vol. 25, p. 780, 12 2015.

[136] J. Zimmerberg and M. M. Kozlov, "How proteins produce cellular membrane curvature," *Nature Reviews Molecular Cell Biology 2005 7:1*, vol. 7, pp. 9–19, 11 2005.

[137] J. L. Gallop, "Filopodia and their links with membrane traffic and cell adhesion," *Seminars in Cell & Developmental Biology*, vol. 102, pp. 81–89, 6 2020.

[138] G. Garcia, D. R. Raleigh, and J. F. Reiter, "How the ciliary membrane is organized inside-out to communicate outside-in," *Current biology : CB*, vol. 28, p. R421, 4 2018.

[139] A. T. T. Pham, A. Wallace, X. Zhang, D. Tohl, H. Fu, C. Chuah, K. J. Reynolds, C. Ramsey, and Y. Tang, "Optical-based biosensors and their portable healthcare devices for detecting and monitoring biomarkers in body fluids," *Diagnostics*, vol. 11, p. 1285, 7 2021.

[140] S. L. Jacques, "Optical properties of biological tissues: a review," *Physics in Medicine & Biology*, vol. 58, p. R37, 5 2013.

[141] L. V. Wang and H. i.. Wu, *Biomedical optics : principles and imaging*. Wiley-Interscience, 2007.

[142] V. Tuchin, "Optical properties of tissues with strong (multiple) scattering," *https://doi.org/10.1117/3.684093.ch1*, vol. PM166, pp. 3–142, 9 2007.

[143] A. Sassaroli and S. Fantini, "Comment on the modified beer–lambert law for scattering media," *Physics in Medicine & Biology*, vol. 49, p. N255, 7 2004.

[144] A. Zardecki and W. G. Tam, "Multiple scattering corrections to the beer-lambert law. 1: Open detector," *Applied Optics, Vol. 21, Issue 13, pp. 2405-2412*, vol. 21, pp. 2405–2412, 7 1982.

[145] E. S. Fry and R. M. Pope, "Absorption spectrum (380–700 nm) of pure water. ii. integrating cavity measurements," *Applied Optics, Vol. 36, Issue 33, pp. 8710-8723*, vol. 36, pp. 8710–8723, 11 1997.

[146] S. L. Jacques and S. A. Prahl, "Omlc — oregon medical laser center: Optical properties database." `https://omlc.org/`, 2018. Accessed: 2025-11-28.

[147] N. Bosschaart, G. J. Edelman, M. C. Aalders, T. G. V. Leeuwen, and D. J. Faber, "A literature review and novel theoretical approach on the optical properties of whole blood," *Lasers in Medical Science*, vol. 29, p. 453, 2013.

[148] G. Saiko, F. Sadrzadeh-Afsharazar, T. Burton, S. Prahl, and A. Douplik, "Absorption, scattering, and refractive index of blood and its components: a review," *Frontiers in Photonics*, vol. 6, p. 1636398, 8 2025.

[149] S. Stocker, F. Foschum, P. Krauter, F. Bergmann, A. Hohmann, C. S. Happ, and A. Kienle, "Broadband optical properties of milk," *Applied Spectroscopy*, vol. 71, pp. 951–962, 5 2017.

[150] A. Gastélum-Barrios, G. M. Soto-Zarazúa, A. Escamilla-García, M. Toledano-Ayala, G. Macías-Bobadilla, and D. Jauregui-Vazquez, "Optical methods based on ultraviolet, visible, and near-infrared spectra to estimate fat and protein in raw milk: A review," *Sensors (Basel, Switzerland)*, vol. 20, p. 3356, 6 2020.

[151] N. Anttu, H. Mäntynen, A. Sorokina, P. Kivisaari, T. Sadi, and H. Lipsanen, "Geometry tailoring of emission from semiconductor nanowires and nanocones," *Photonics 2020, Vol. 7, Page 23*, vol. 7, p. 23, 3 2020.

[152] J. D. Jackson, *Classical Electrodynamics*. John Wiley & Sons, 3rd ed., 1999.

[153] J. Y. J.-P. H. P. Lalanne, "Light-in-complex-nanostructures/retop: Version 8.1," Apr. 2020.

[154] L. Novotny and B. Hecht, *Principles of Nano-Optics*. Cambridge University Press, 2nd ed., 2012.

[155] T. Ursell, "Generate random numbers from a 2d discrete distribution." `https://www.mathworks.com/matlabcentral/fileexchange/35797-generate-random-numbers-from-a-2d-discrete-distribution`, Dec. 2023. MATLAB Central File Exchange.

[156] H. Deschout, K. Neyts, and K. Braeckmans, "The influence of movement on the localization precision of sub-resolution particles in fluorescence microscopy," *Journal of Biophotonics*, vol. 5, pp. 97–109, 1 2012.

[157] C. Solomon and T. Breckon, *Fundamentals of Digital Image Processing: A Practical Approach with Examples in Matlab*. Chichester, UK: John Wiley & Sons, Ltd, first ed., 2010.

[158] W. Burger and M. J. Burge, *Principles of Digital Image Processing: Fundamental Techniques*. Springer Publishing Company, Incorporated, 1 ed., 2009.

[159] MathWorks, "What is image filtering in the spatial domain?."

[160] A. de Juan, A. Gowen, L. Duponchel, and C. Ruckebusch, *Image Fusion*, vol. 31. 2019.

[161] R. C. Gonzalez and R. E. R. E. Woods, *Digital image processing*. 4th ed.

[162] I. Izeddin, J. Boulanger, V. Racine, C. Specht, A. Kechkar, D. Nair, A. Triller, D. Choquet, M. Dahan, and J. Sibarita, "Wavelet analysis for single molecule localization microscopy," *Opt. Express*, vol. 20, pp. 2081–2095, Jan 2012.

[163] J. Schnitzbauer, M. T. Strauss, T. Schlichthaerle, F. Schueder, and R. Jungmann, "Super-resolution microscopy with dna-paint," *Nature Protocols*, vol. 12, pp. 1198–1228, 6 2017.

[164] J. Serra, *Image Analysis and Mathematical Morphology*, vol. 1. Academic Press, 1982.

[165] C. S. Smith, N. Joseph, B. Rieger, and K. A. Lidke, "Fast, single-molecule localization that achieves theoretically minimum uncertainty," *Nature Methods*, vol. 7, no. 5, pp. 373–375, 2010. Epub 2010 Apr 4.

[166] D. Deng, "Dbscan clustering algorithm based on density," *Proceedings - 2020 7th International Forum on Electrical Engineering and Automation, IFEEA 2020*, pp. 949–953, 9 2020.

[167] A. M. Ikotun, A. E. Ezugwu, L. Abualigah, B. Abuhaija, and J. Heming, "K-means clustering algorithms: A comprehensive review, variants analysis, and advances in the era of big data," *Information Sciences*, vol. 622, pp. 178–210, 4 2023.

[168] N. Alibabaie and A. M. Latif, "Fuzzy notch filter for periodic and quasi-periodic noise reduction in digital images," 10 2019.

[169] D. Chakraborty, M. K. Tarafder, A. Banerjee, and S. R. B. Chaudhuri, "Gabor-based spectral domain automated notch-reject filter for quasi-periodic noise reduction from digital images," *Multimedia Tools and Applications*, vol. 78, pp. 1757–1783, 1 2019.

[170] I. Aizenberg and C. Butakoff, "A windowed gaussian notch filter for quasi-periodic noise removal," *Image Vis Comput*, vol. 26, pp. 1347–1353, 10 2008.

[171] Q. Du, M. Gunzburger, and L. Ju, "Advances in studies and applications of centroidal voronoi tessellations," *Numerical Mathematics*, vol. 3, pp. 119–142, 2010.

[172] J. Bernauer, R. P. Bahadur, F. Rodier, J. Janin, and A. Poupon, "Dimovo: a voronoi tessellation-based method for discriminating crystallographic and biological protein–protein interactions," *Bioinformatics*, vol. 24, pp. 652–658, 3 2008.

[173] F. Aurenhammer, "Voronoi diagrams: a survey of a fundamental geometric data structure," *ACM Computing Surveys (CSUR)*, vol. 23, pp. 345–405, 9 1991.

[174] Z. Liu, L. Jin, J. Chen, Q. Fang, S. Ablameyko, Z. Yin, and Y. Xu, "A survey on applications of deep learning in microscopy image analysis," *Computers in Biology and Medicine*, vol. 134, p. 104523, July 2021.

[175] E. Moen, D. Bannon, T. Kudo, and et al., "Deep learning for cellular image analysis," *Nat Methods*, vol. 16, pp. 1233–1246, December 2019.

[176] O. Ronneberger, P.Fischer, and T. Brox, "U-net: Convolutional networks for biomedical image segmentation," in *Medical Image Computing and Computer-Assisted Intervention (MICCAI)*, vol. 9351 of *LNCS*, pp. 234–241, Springer, 2015. (available on arXiv:1505.04597 [cs.CV]).

[177] A. E. Ilesanmi and T. O. Ilesanmi, "Methods for image denoising using convolutional neural network: a review," *Complex Intell. Syst.*, vol. 7, pp. 2179–2198, 2021.

[178] N. R. Huber, A. Ferrero, K. Rajendran, F. Baffour, K. N. Glazebrook, F. E. Diehn, A. Inoue, J. G. Fletcher, L. Yu, S. Leng, and C. H. McCollough, "Dedicated convolutional neural network for noise reduction in ultra-high-resolution photon-counting detector computed tomography," *Phys Med Biol*, vol. 67, no. 17, pp. 10.1088/1361–6560/ac8866, 2022.

[179] S. Xie, J. Song, Y. Hu, C. Zhang, and S. Zhang, "Using cnn with multi-level information fusion for image denoising," *Electronics*, vol. 12, p. 2146, 2023. Submission received: 21 March 2023 / Revised: 4 May 2023 / Accepted: 5 May 2023 / Published: 8 May 2023.

[180] A. Krizhevsky, I. Sutskever, and G. E. Hinton, "Imagenet classification with deep convolutional neural networks," 2012.

[181] S. Albawi, T. A. Mohammed, and S. Al-Zawi, "Understanding of a convolutional neural network," *Proceedings of 2017 International Conference on Engineering and Technology, ICET 2017*, vol. 2018-January, pp. 1–6, 7 2017.

[182] W. P. McCormick, N. I. Lyons, and K. Hutcheson, "Distributional properties of jaccard's index of similarity," *Communications in Statistics - Theory and Methods*, vol. 21, pp. 51–68, 1 1992.

[183] S. T. Flock, S. L. Jacques, B. C. Wilson, W. M. Star, and M. J. van Gemert, "Optical properties of intralipid: A phantom medium for light propagation studies," *Lasers in Surgery and Medicine*, vol. 12, pp. 510–519, 1 1992.

[184] J. Veerbeek, R. Steen, W. Vijselaar, W. F. Rurup, S. Korom, A. Rozzi, R. Corradini, L. Segerink, and J. Huskens, "Selective functionalization with pna of silicon nanowires on silicon oxide substrates," *Langmuir*, vol. 34, p. 11395, 9 2018.

[185] E. Joseph, S. S. Rajput, S. Patil, and A. Nisal, "Mechanism of adhesion of natural polymer coatings to chemically modified siloxane polymer," *Langmuir*, vol. 37, pp. 2974–2984, 3 2021.

[186] J. L. Watson, D. Juergens, N. R. Bennett, B. L. Trippe, J. Yim, H. E. Eisenach, W. Ahern, A. J. Borst, R. J. Ragotte, L. F. Milles, B. I. Wicky, N. Hanikel, S. J. Pellock, A. Courbet, W. Sheffler, J. Wang, P. Venkatesh, I. Sappington, S. V. Torres, A. Lauko, V. D. Bortoli, E. Mathieu, S. Ovchinnikov, R. Barzilay, T. S. Jaakkola, F. DiMaio, M. Baek, and D. Baker, "De novo design of protein structure and function with rfdiffusion," *Nature 2023 620:7976*, vol. 620, pp. 1089–1100, 7 2023.

[187] S. R. Whaley, D. S. English, E. L. Hu, P. F. Barbara, and A. M. Belcher, "Selection of peptides with semiconductor binding specificity for directed nanocrystal assembly," *Nature 2000 405:6787*, vol. 405, pp. 665–668, 6 2000.

[188] Z. Gu, Z. Yang, Y. Chong, C. Ge, J. K. Weber, D. R. Bell, and R. Zhou, "Surface curvature relation to protein adsorption for carbon-based nanomaterials," *Scientific Reports 2015 5:1*, vol. 5, pp. 10886–, 6 2015.

Scientific publications

Printed by Media-Tryck, Lund 2026 NORDIC SWAN ECOLABEL 3041 0903

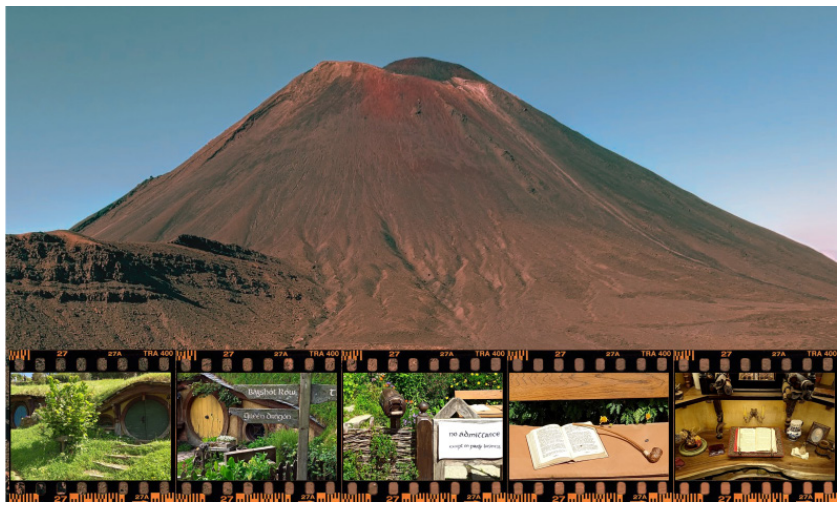

LUND UNIVERSITY

Department of Physics
Faculty of Engineering

ISBN 978-91-8104-794-3